16th Brazilian Congress of Mechanical Engineering

Engineering for the New Millennium

MICROSYSTEMS DESIGN

ISBN 85-85769-06-6

Microsystems Design

XVI CONGRESSO BRASILEIRO DE ENGENHARIA MECÂNICA
16th BRAZILIAN CONGRESS OF MECHANICAL ENGINEERING

EFEITO DO ESTADO METALÚRGICO DE UMA LIGA DE ALUMÍNIO SOBRE O ACABAMENTO E A INTEGRIDADE SUPERFICIAL NA USINAGEM DE ULTRAPRECISÃO

Rogério Madureira de Almeida
Arthur José Vieira Porto
Jaime Gilberto Duduch
Helder Augustus Treviso da Silva
Escola de Engenharia de São Carlos/USP. Av. Trabalhador São-carlense – 400, Centro. CEP: 13566-590 São Carlos/SP
e-mail: rogerioalmeida@yahoo.com.br, ajvp@sc.usp.br, jgduduch@sc.usp.br, helderts@sc.usp.br

Renato Goulart Jasinevicius
SOCIESC-IST/Centro de Mecânica de Precisão de Joinville. R. Albano Schmidt – 3333, Boa Vista. CEP:89227-700 Joinville/SC
e-mail: rgvicius@sociesc.com.br

Resumo. *Este trabalho apresenta um estudo experimental sobre a influência das condições de usinagem sobre o acabamento superficial e a integridade superficial de uma liga de alumínio metalurgicamente transformada, faceada com uma ferramenta de diamante. Para isso avaliou-se a influência das condições de usinagem sobre o acabamento superficial e a integridade superficial através da micro dureza desta liga. Os parâmetros de corte variados foram o avanço (f) e profundidade de corte (ap). Os resultados mostram que a rugosidade superficial aumentou com a diminuição da dureza superficial. A profundidade de corte parece ter pouca influência sobre o acabamento superficial. A amostra laminada apresentou as menores rugosidades de pico-a-vale, o qual foram atribuídas à geometria da ferramenta.*

Palavras chave:. ferramenta de diamante, acabamento superficial e integridade superficial

1. Introdução

O torneamento com ferramenta de diamante ou usinagem de ultraprecisão é utilizado principalmente para fabricação de substratos utilizados em discos magnéticos, espelhos poligonais para impressoras laser entre outras aplicações (Schroeter, 1999). O acabamento superficial dos espelhos usinados a partir de metais não ferrosos utilizando ferramentas de diamante são inferiores a 10 nm Ra (Hashimoto, 1984). No entanto sabe-se que a rugosidade superficial é normalmente maior do que a rugosidade superficial geométrica determinada através dos parâmetros de avanço e geometria da ferramenta. Sabe-se que ferramentas com raio de ponta grande sofrem menos influência do material do que ferramentas com raio de ponta pequeno. Os fatores que influenciam este fenômeno estão relacionados a aspectos do material da ferramenta e da máquina traduzido através de vibrações de baixa amplitude e/ou trepidações (Sata, 1985). Dentre os aspectos relacionados a materiais não ferrosos encontra-se: tamanho de grão, propriedades físicas (dureza, resistência a tração) e orientação cristalográfica. Segundo König (1991) e Ohmori (1982), sabe-se que durante a usinagem de ultraprecisão as condições de corte são geralmente inferiores ao tamanho médio dos grãos do agregado policristalino. Em função disso, pode-se afirmar que a ferramenta deve passar várias vezes dentro de um único grão. Isso pode gerar pequenas imperfeições causadas pela diferença de propriedades observada de um grão para outro. Dentre as possíveis soluções propostas encontra-se as seguintes: redução do tamanho de grão, utilização de um monocristal ou a laminação do substrato visando obter uma orientação preferencial para os grãos.

Durante a usinagem, a interação ferramenta-material gera uma deformação superficial no material diferente daquela observada no substrato. A camada deformada plasticamente em uma superfície usinada deve apresentar propriedades mecânicas diferentes das iniciais. O estudo dessas propriedades devem ser avaliadas com o objetivo de caracterizar a integridade superficial (Evans, 1987 e Lucca, 1998). As análises das superfícies usinadas podem incluir a quantificação da deformação plástica e a distribuição de tensões. Existem diversas técnicas experimentais para se avaliar a integridade superficial, entre elas a metalografia (ataque químico, medição da micro dureza e técnicas de recristalização).

Devido às dimensões de corte utilizado e baseado em dados obtido na literatura, acredita-se que a medida de micro dureza pode ser utilizada como meio de avaliação da integridade superficial. A espessura da camada deformada após a usinagem de ultraprecisão é da ordem de 3 μm (Diniz, 1998).

O objetivo desse trabalho é testar condições de usinagem em uma liga de alumínio metalurgicamente transformada. Para isso será avaliada a influência das condições de usinagem sobre o acabamento superficial e a integridade superficial através de micro dureza.

2. Procedimento Experimental

A máquina ferramenta utilizada nos ensaios foi um torno "Aspheric Surface Generator" ASG 2500 Rank Pneumo. Esta máquina possui uma base de ferro fundido, termicamente livre de tensões, sendo isolada de vibrações externas através de isoladores passivos a ar montados cinematicamente numa estrutura de aço. O eixo árvore é sustentado por mancais aerostáticos de escora que conferem alta rigidez axial. Um CNC Allen-Bradley 8200 é utilizado

para controlar o deslocamento e a posição dos eixos simultaneamente. A posição dos eixos é monitorada por transdutores interferométricos a laser. A resolução da máquina é de 10 nm.

O material utilizado para produzir superfícies espelhadas é uma liga de Alumínio – KOBE-M2B. As propriedades mecânicas e a composição química dessa liga estão resumidas nas Tab.1 e Tab.2.

Tabela 1. Propriedades mecânicas da liga Al KOBE-M2B

Limite de escoamento (MPa)	Limite de ruptura (Mpa)	Alongamento (%)
141	259,5	43

Tabela 2. Composição química da liga Al KOBE-M2B

Elementos	Si	Fe	Cu	Mn	Mg	Cr	Zn	Ti	Al
Composição (%)	0,004	0,022	0,001	0,003	4,03	0	0,002	0,003	Resto

O material precisa ter um alívio de tensão por um dos dois seguintes métodos:

a) 1-Temp: 380°C por 3 horas
2-Resfriamento natural para se alcançar a temperatura do ambiente.

b) 1-Temp: 250-280°C por 8 horas
2-Resfriamento natural para se alcançar a temperatura do ambiente.

Os diferentes tamanhos de grão das amostras utilizadas podem ser observadas através das micrografias das superfícies mostradas nas Figs. 1,2 e 3.

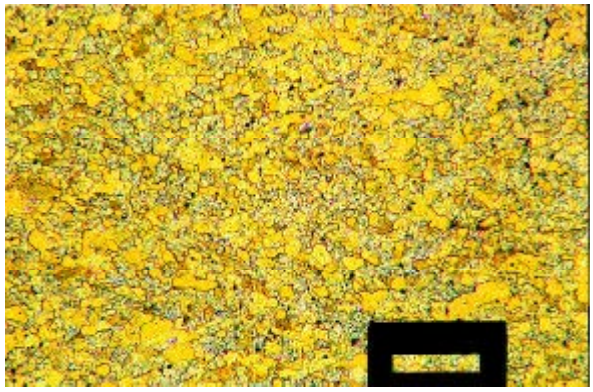

Figura 1: Micrografia de uma amostra com TGp (tamanho de grão pequeno), ampliada 100x

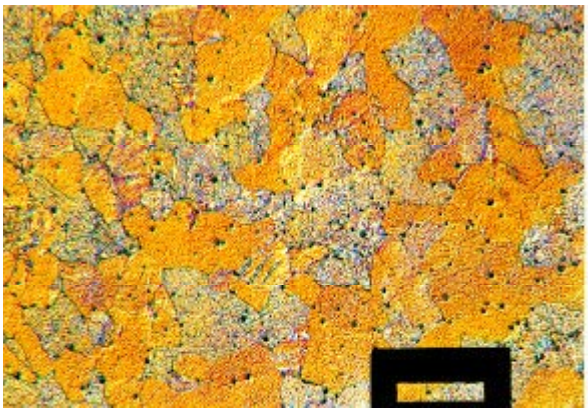

Figura 2: Micrografia de uma amostra com TGn (tamanho de grão normal), ampliada 100x

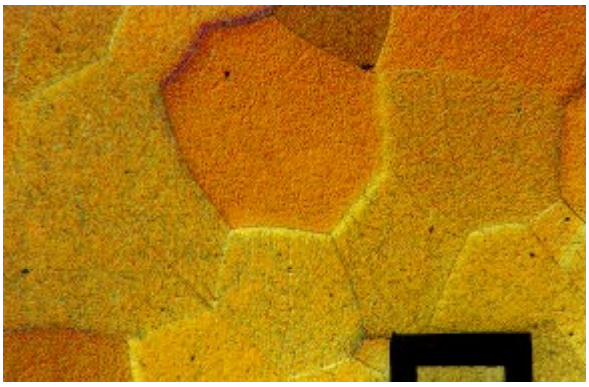

Figura 3: Micrografia de amostra laminada (80%), ampliada 50x

As peças de alumínio são preparadas em um torno convencional. A Fig. 4, é uma micrografia mostrando o acabamento da superfície da peça usinada com ferramenta de aço rápido. A rugosidade média (Ra) desta superfície era de 0,35 μm e a rugosidade de pico a vale (Rt) era de 2,1μm.

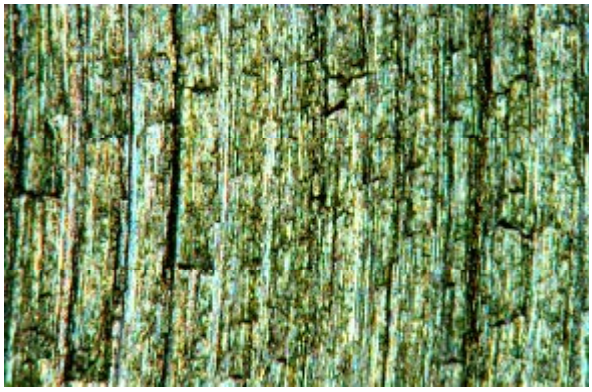

Figura 4: Estado da superfície previamente usinada com ferramenta de aço rápido, ampliada 100x

Estas peças são então montadas num dispositivo de fixação também de alumínio, especialmente fabricado para a fixação dos corpos de prova na placa de vácuo do torno de ultraprecisão.

Após a fixação à placa de vácuo da máquina os corpos de prova são faceados e recebem passos de desbaste (ap=20 μm e f=20 μm/rev) para acertar a planicidade e para remoção da camada superficial provavelmente oxidada.

Os parâmetros de corte que foram variados neste trabalho foram a profundidade de corte (ap) e o avanço (f) a fim de se observar a rugosidade superficial da peça. Foi realizado também um ensaio de micro indentação para se medir a micro dureza do material da peça. O micro durômetro utilizado foi um BUEHLER (modelo n 1600-6300).

Cada peça recebeu 8 passos variando-se a profundidade de corte e o avanço da seguinte maneira: fixando-se a profundidade de corte (10 μm) e variando-se o avanço (30; 15; 10 e 5 μm/rev) e em seguida fixando-se o avanço (15 μm/rev) e variando-se a profundidade de corte (30; 20; 10 e 5 μm), todas com a mesma rotação de 1000 rpm. A Fig. 5, mostra o diagrama esquemático de uma peça usinada com esse procedimento.

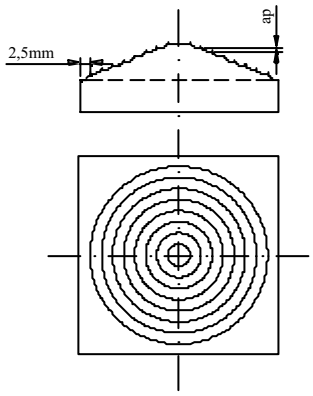

Figura 5: Diagrama esquemático dos passos de usinagem em uma peça de Al – KOBE-M2B.

Para o ensaio de dureza uma outra amostra foi desbastada com as seguintes condições de corte: fixou-se o avanço (5 μm/rev) variando-se a profundidade de corte 5 vezes (5,0; 2,5; 1,5; 1,0 e 0,5 μm), pois a espessura da camada encruada pode variar em função das condições de corte, geometria (γ, α) e afiação da ferramenta.

A avaliação do acabamento superficial foi realizado com um FORM TALYSURF modelo 120L. Os parâmetros analisados foram:

-Rugosidade (P-V)Rt e

-Rugosidade média aritmética Ra

Todos os ensaios de corte foram realizados com uma ferramenta Difer nacional com as seguintes características:

-ângulo de folga (α): <5°

-ângulo de saída (γ): 0°

-raio de ponta (r_p): 4mm

3. Resultados e Discussões

Os desvios padrão dos resultados obtidos nesses ensaios são os seguintes: para Rt estão variando na faixa de 0,002 a 0,01μm e para Ra estão na faixa de 0,001 a 0,002μm.

Influência do Avanço (f): através deste experimento foi observado que os resultados de rugosidade superficial obtidos não se aproximam dos resultados teoricamente representados por Jasinevicius (1995), pela Eq. (1).

$$R_t = \frac{f^2}{8r_p} \qquad (1)$$

Tomando-se o avanço como o parâmetro de avaliação e fixando-se a profundidade de corte (10μm) e a rotação (1000rpm), os seguintes resultados são apresentados pela Tab.3.

Tabela 3: Valores de Ra e Rt medidos em todas as amostras (ap=10μm).

Condições de Corte	Acabamento Superficial (nm)							
Avanço	TGp		TGg		TGn		L (80%)	
f (μm/rev)	Ra	Rt	Ra	Rt	Ra	Rt	Ra	Rt
5	7,2	64,3	6,8	60,4	7,4	68,6	6,4	52,4
10	7,2	63,9	7,1	58,8	8,5	73,4	7,9	68,5
15	7,7	66,4	7,6	81,3	7,7	67,2	7,1	59,5
30	10,5	81,3	9,8	73,5	10,8	81,1	8,4	70,6

Como mostra a Tab.3, os valores de Rt (rugosidade superficial pico a vale) são muito maiores do que os valores teoricamente calculados, mas notou-se também que houve um aumento da rugosidade com o aumento do avanço o que é uma tendência teoricamente esperada.

Os valores de Ra medidos sobre as mesmas condições de corte estão apresentados na mesma Tab.3. Os resultados apresentam a mesma tendência de aumento da rugosidade com o aumento do avanço. Para as peças com tamanho de grão pequeno (TGp) e tamanho de grão grande (TGg) os valores de Ra se mantiveram praticamente constantes para valores de avanço entre 5 e 10 μm/rev. Para valores de avanço acima de 15 μm/rev os valores de Ra aumentaram significativamente. Para a peça laminada (80%) Ra manteve-se praticamente a mesma com pequenas variações.

Influência da Profundidade de Corte (ap): tomando-se a profundidade de corte como parâmetro de avaliação e fixando-se o avanço (15 μm/rev) e a rotação (1000rpm) os resultados obtidos são apresentados na Tab.4.

Tabela 4: Valores de Rt medidos em todas amostras (f=15 μm/rev).

Condições de Corte	Rugosidade Pico a Vale (Rt ~ nm)			
Profundidade (ap ~ μm)	TGp	TGg	TGn	L(80%)
5	62,6	59,6	67,4	64,4
10	66,4	81,3	67,2	59,5
20	58,9	59,9	66,3	61,0
30	58,7	-	80,4	63,4

De acordo com os resultados da Tab.4, pode-se inferir que a profundidade de corte tem pouca influência sobre o acabamento superficial, porém, para profundidades de corte maiores houve uma pequena redução nos valores de rugosidade superficial tendendo a serem mais estáveis. Isto deve ocorrer devido a um recuo elástico do material durante a usinagem, o que faz com que o contato entre o material da peça e a face de folga da ferramenta aumente, provocando assim um aumento do efeito "burnishing" ("amassamento") no material. Este fenômeno pode induzir um aumento da espessura da camada deformada tanto superficial como subsuperficiais e aumento de tensões residuais na superfície.

Através do teste de micro dureza realizado nas peças foi possível obter os resultados apresentados na Tab.5.

Tabela 5: Valores de micro dureza medidos em todas peças (f=5µm/rev e ap=10µm).

	TGp		TGg		TGn		L (80%)	
	$Hv_{méd}$	Pp	$Hv_{méd}$	Pp	$Hv_{méd}$	Pp	$Hv_{méd}$	Pp
Carga (g)								
10	68,3	3,34	69,5	3,29	69,7	3,29	109,9	2,6
25	68,0	5,25	69,5	5,1	68,9	5,23	109,2	4,2
50	66,4	7,6	62,9	7,4	69,4	7,43	114,5	5,7
100	63,0	10,9	62,6	10,7	69,1	10,42	111,2	8,2
200	61,1	15,7	62	15,3	66,3	15	108,3	11,8
300	61,4	19,3	60,5	18,5	66	18,4	108,2	14,5

O perfil da superfície usinada é basicamente composto de uma repetição do perfil da aresta de corte da ferramenta transferido em planos normais a direção de corte, ou seja, a rugosidade do perfil da aresta de corte é transferido à superfície usinada (Purquerio, 1994).

De acordo com os resultados da Tab.5, pode-se notar que as amostras que não sofreram um processo de conformação metálico antes da usinagem, apresentaram um valor de dureza baixo, próximo ao valor de dureza do Al puro, que está ao redor de 65Hv. Pelo fato do alumínio ser um material de baixa dureza houve uma deformação elastoplástica do material durante o processo de usinagem, provocando assim o efeito "burnishing" já citado anteriormente.

Já o material da amostra que passou por um processo de laminação antes da usinagem apresentou uma dureza bem superior e praticamente constante na faixa de 110Hv. O fato da amostra laminada apresentar maior dureza e melhor orientação cristalográfica dos grãos, faz com que o material se deforme mais fácil e plasticamente e assim permite que o perfil da aresta de corte da ferramenta seja melhor impresso na superfície da peça usinada, obtendo-se um melhor acabamento superficial.

A superfície das amostras com tamanho de grão pequeno e tamanho de grão grande, usinadas com ferramenta de diamante, são mostradas nas Figs. 6 e 7.

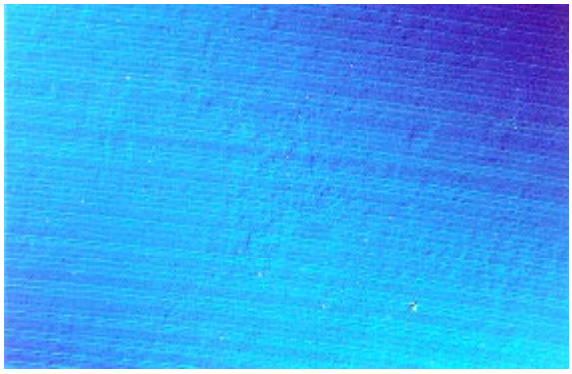

Figura 6: Superfície usinada de uma amostra com TGp, ampliada 200x

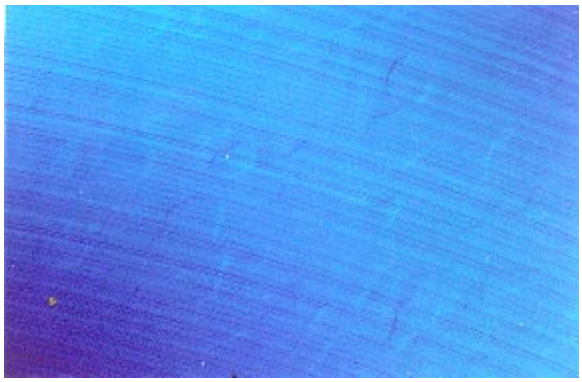

Figura 7: Superfície usinada de uma amostra com TGn, ampliada 200x

As condições de corte (f, ap) utilizadas neste experimento foram muito inferiores ao tamanho médio dos grãos do agregado cristalino. Com isso, pela Fig. 7, podemos observar que a ferramenta passou várias vezes dentro de um único grão, o que não se observa na Fig. 6, resultando assim uma superfície melhor acabada.

O fato de ter-se escolhido uma ferramenta com raio de ponta grande (4mm) é que esta sofre menos influência do material do que ferramentas com raio de ponta pequeno. Sabe-se que um material policristalino apresenta propriedades físicas, tamanho e orientação dos grãos diferentes no cristal. Deste modo, ao se utilizar uma ferramenta com raio de ponta pequeno esta sofrerá maior influência dessas propriedades, como por exemplo, diferença de elasticidade de um grão para outro, "steps" ("degraus") entre um grão e outro devido a terem tamanhos diferentes e a mudança dos planos de deslizamento preferenciais que cada grão possui ao se passar de um grão para outro. Com isso, utilizando-se uma ferramenta com raio de ponta grande essas influências são minimizadas.

4. Considerações Finais

Este trabalho apresentou um estudo experimental sobre a influência das condições de usinagem sobre o acabamento superficial e a integridade superficial de uma liga de alumínio metalurgicamente transformada, faceada com uma ferramenta de diamante.

O avanço mostrou-se o parâmetro de maior influência, com menores valores de rugosidade superficial obtidos para valores de avanço entre 5 e 10μm/rev. A profundidade de corte apresentou pouca influência nos resultados de acabamento superficial, porém, para profundidades de corte maiores, de 20 a 30μm, observou-se uma pequena redução nos valores de rugosidade superficial.

A possível solução utilizada neste experimento para eliminação dos problemas causados pela diferença de propriedades observada de um grão para outro foi a laminação do substrato de uma das amostras, conseguindo-se assim, superfícies com melhor acabamento superficial.

5. Agradecimentos

Ao CNPq e a FAPESP pelo apoio financeiro à pesquisa.

6. Referências Bibliográficas

Diniz, A. E., Noritomi, P.Y., 1998, "Influência dos Parâmetros de Corte na Rugosidade". Máquinas e Metais, Vol. 391, pp. 92– 101.

Evans, C.,et al, 1987, "Some Observations on Tool Sharpness and Sub-Surface Damage in Single Point Diamond Turning". Spie, Vol. 802, In-Process Optical Metrology for Precision Machining.

Hashimoto, H., et al, 1984, "Formation Mechanisms Of Ultraprecision Machined Surfaces With A Single Point Diamond Tool". Procedings of the 5th International Conference on Production Engineering, Tokio, .

Jasinevicius, R. G., Porto, A. J. V., Duduch, J. G., 1995, "Influência da condições de usinagem no torneamento de ultraprecisão de uma liga de alumínio com ferramenta de diamante", COBEM-CIDIM, XIII, .

König, W., et al, 1991, "Diamond Machining Technology". (tutorial), 6th IPES. Sem, Braunscheweig, 96p.

Lucca, D. A., et al, 1998, "Progress In Assessing Surface and Subsurface Integrity". Annals of the CIRP, Vol. 47/2, pp. 669 – 693.

Ohmori, G., Takada, S., 1982, "Primary Factor Affecting Accuracy In Ultra Precision Machining by Diamond Tool". Bull. Japan Soc of Pre. Engg., Vol. 16(1), pp. 3-7.

Purquerio, B. M., et al, 1994, "O Torneamento de Ultraprecisão Já é Possível no Brasil". Máquinas e Metais, pp. 106-116.

Sata, T., et al, 1985, "Analysis of Surface Roughness Generation In Turning Operation and its Aplications". Annals of the CIRP, Vol. 34/1.

Schroeter, R. B., Weingaertner, W. L., A USINAGEM DE ULTRAPRECISÃO. Máquinas e Metais, v. 396, p. 20-35, Janeiro 1999.

EFFECT OF THE METALURGICAL STATE OF AN ALUMINUM ALLOY ON SURFACE INTEGRITY IN ULTRAPRECISION MACHINING

Rogério Madureira de Almeida
Arthur José Vieira Porto
Jaime Gilberto Duduch
Helder Augustus Treviso da Silva
Escola de Engenharia de São Carlos/USP. Av. Trabalhador São-carlense – 400, Centro. CEP: 13566-590 São Carlos/SP
e-mail: rogerioalmeida@yahoo.com.br, ajvp@sc.usp.br, jgduduch@sc.usp.br, helderts@sc.usp.br

Renato Goulart Jasinevícius
SOCIESC-IST/Centro de Mecânica de Precisão de Joinville. Rua Albano Schmidt - 3333 Boa Vista. CEP: 89227-700 Joinville/SC
e-mail: rgvicius@sociesc.com.br

Abstract. *The influence of cutting conditions on surface integrity during machining of metalurgically modified aluminum alloy was investigated. Facing cuts were performed in order to test the machining conditions on the aluminum alloy samples. The cutting parameters assessed were feed rate and depth of cut. Surface finish and surface microhardness of the machined samples were evaluated. The results show that surface roughness increased with the decrease in surface hardness. The cutting depth seems to have very slight influence on surface finish. The cold rolled sample (80% reduction) presented lower peak-to-valley roughness which were attributed to the diamond tool geometry. It is shown that the diagonal size of the indentation mark increases with the reduction in microhardness. The cold rolled sample presented the smallest diagonal size while the sample with large grain size showed the largest.*

Keywords: *diamond tool, ultraprecision machining, surface finishing, surface integrity.*

XVI CONGRESSO BRASILEIRO DE ENGENHARIA MECÂNICA
16th BRAZILIAN CONGRESS OF MECHANICAL ENGINEERING

MEDIÇÃO DE DESLOCAMENTOS NO PLANO E FORA DO PLANO UTILIZANDO HOLOGRAFIA DIGITAL

Analucia Vieira Fantin
Universidade Federal de Santa Catarina, SC,
Laboratório de Metrologia e Automatização
Campus Universitário – Trindade – 88040-970, Florianópolis, SC, Brasil
avf@labmetro.ufsc.br

Armando Albertazzi Gonçalves Jr.
Universidade Federal de Santa Catarina, SC,
Laboratório de Metrologia e Automatização
Campus Universitário – Trindade – 88040-970, Florianópolis, SC, Brasil
albertazzi@labmetro.ufsc.br

***Resumo**: A evolução das câmeras CCD e dos sistemas de processamento de imagens viabilizou o desenvolvimento da Holografia Digital. O filme fotográfico pôde ser substituído por sensores CCD de elevada resolução capazes de registrar os complexos padrões de interferência. A Holografia Digital envolve o registro do padrão de interferência das ondas de referência e do objeto no próprio CCD da câmera de TV. A partir de dois hologramas digitais, gravados para dois diferentes estados do objeto (não deformado e deformado), os valores de intensidade e a diferença de fase entre estes dois estados, são reconstruídos numericamente. O trabalho aborda o desenvolvimento de uma formulação que aplica a Holografia Digital para medir deslocamentos no plano. Esta concepção transfere para o software a responsabilidade de algumas etapas de medição como, por exemplo, o deslocamento de fase. O trabalho ainda apresenta uma aplicação prática do método.*

***Palavras-chave**: Holografia Digital, Interferometria, Metrologia Óptica, Medição não destrutiva.*

1. Princípio da Holografia Digital

O avanço tecnológico e o surgimento de câmeras CCD de alta resolução, contribuíram para o desenvolvimento de uma nova técnica de medição de deslocamentos, a Holografia Digital. Na Holografia Digital, hologramas de Fresnel são gerados diretamente no CCD de uma câmera de alta resolução (Carcolé et al, 1994).

Estes hologramas representam o objeto no seu estado deformado e não deformado. As imagens produzidas por estes dois estados são armazenadas na memória do microcomputador e a reconstrução das ondas luminosas é feita numericamente. O cálculo para reconstrução das imagens baseia-se em uma aproximação da integral de difração.

Ao contrário da Eletronic Speckle Pattern Interferometry (ESPI) (Boettger, 1998), na Holografia Digital não são utilizadas lentes ou qualquer outro instrumento óptico para reconstrução da frente de onda. O processo é totalmente digital.

A principal vantagem da técnica de Holografia Digital é que, além da intensidade da frente de onda, os valores de fase são calculados diretamente no processo de reconstrução numérica. Isto significa que a interferência de fase que representa o campo de deformação, pode ser calculada através da subtração das distribuições de fase das ondas reconstruídas.

1.1. Teorema da Amostragem

A utilização do CCD na holografia digital só se tornou viável com o surgimento do CCD de alta resolução. O Teorema da Amostragem exige que cada período da variação espacial na distribuição de intensidade do holograma seja amostrado por pelo menos dois pixels do CCD.

A interferência em cada ponto do holograma é determinada pelo ângulo entre a onda de referência e a onda do objeto (Kreis et al, 1998; Kobayashi, 1989):

$$\delta = \frac{\lambda}{2\,\mathrm{sen}(\theta/2)} \tag{1}$$

Onde δ é espaçamento entre duas franjas, θ o ângulo entre a onda do objeto e a onda de referência e, λ o comprimento de onda.

Para um CCD com dimensão do pixel igual a $\Delta\xi$, de acordo com o Teorema da Amostragem devemos ter $2\Delta\xi < \delta$. Esta desigualdade implica que um pequeno ângulo entre a onda do objeto e a onda de referência deve ser mantido. No caso de pequenos ângulos pode-se admitir que $\text{sen}(\theta) \approx \theta$.

Sendo assim, substituindo $\text{sen}(\theta/2)$ por $\theta/2$ e δ por $2\Delta\xi$ na Eq.(1), o ângulo máximo admitido para geração de um padrão de interferência fica definido como:

$$\theta < \frac{\lambda}{2\Delta\xi} \tag{2}$$

Ou seja, o ângulo é delimitado pelo tamanho do pixel do CCD (Kreis and Jüptner, 1997).

Desde que o teorema da amostragem não seja violado qualquer onda de referência pode ser utilizada: colimada ou divergente, com incidência normal ou oblíqua ao CCD. A onda plana é preferivelmente utilizada em experimentos, pois é facilmente modelada para o cálculo de reconstrução numérica.

2. Reconstrução Numérica

Fisicamente, a reconstrução da imagem a partir de hologramas gravados em placas de material sensível a luz é feita através da iluminação do holograma com a onda de referência. Na Holografia Digital este passo foi substituído por operações matemáticas envolvendo o conceito e os princípios da teoria de difração (Hacht, 1974).

A partir da teoria de difração o campo difratado por um holograma pode ser calculado por (Goodman, 1996):

$$b(x, y) = \frac{1}{i\lambda}\int\int h(\xi,\eta) r(\xi,\eta) \frac{\exp(ik\rho)}{\rho} \cos\theta \, d\xi \, d\eta \tag{3}$$

Onde,

$h(\xi,\eta)$: intensidade do holograma

$r(\xi,\eta)$: função da onda de referência

λ: comprimento de onda

$k = \frac{2\pi}{\lambda}$: número de onda

ρ: distância entre pontos do holograma e da imagem

z: distância entre holograma e plano da imagem

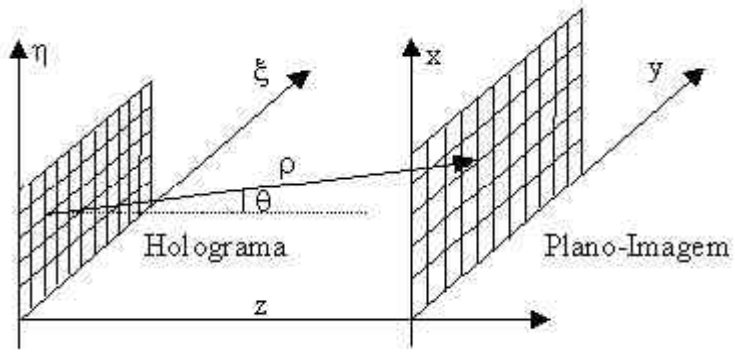

Figura 1– Geometria da Holografia Digital de Fresnel

Onde o termo ρ e cosseno são definidos matematicamente por:

$$\cos\theta = \frac{z}{\rho} \tag{4}$$

$$\rho = \sqrt{z^2 + (x-\xi)^2 + (y-\eta)^2} \tag{5}$$

A integral pode ser re-escrita como:

$$b(x,y) = \frac{z}{i\lambda}\int\int h(\xi,\eta) r(\xi,\eta) \frac{\exp(ik\rho)}{\rho^2} d\xi d\eta \tag{6}$$

2.1. Aproximação de Fresnel

Para reduzir a integral da difração a uma expressão mais simples e útil, algumas aproximações devem ser introduzidas para a distância ρ. As aproximações são baseadas na expansão binomial da Eq.(5) (Goodman, 1996).

Seja b um número menor que uma unidade, então considere a expressão $\sqrt{1+b}$. A expansão binomial desta raiz quadrada é dada por:

$$\sqrt{1+b} = 1 + \frac{1}{2}b - \frac{1}{8}b^2 + ... \tag{7}$$

Onde o número de termos necessários para uma dada precisão depende da magnitude de b. Para aplicar a expansão binomial à Eq.(5) fatora-se o primeiro termo do radical para fora da raiz quadrada.

$$\rho = z\sqrt{1 + (\frac{x-\xi}{z})^2 + (\frac{y-\eta}{z})^2} \tag{8}$$

Onde, neste caso, a quantidade b representa o segundo e terceiro termo do radical. Substituindo estes termos na Eq.(8):

$$\rho = z\left[1 + \frac{1}{2}\left((\frac{x-\xi}{z})^2 + (\frac{y-\eta}{z})^2\right) - \frac{1}{8}\left((\frac{x-\xi}{z})^2 + (\frac{y-\eta}{z})^2\right)^2 + ...\right] \tag{9}$$

Considerando apenas os dois primeiros termos da expansão binomial chega-se ao resultado:

$$\rho = z\left[1 + \frac{1}{2}\left((\frac{x-\xi}{z})^2 + (\frac{y-\eta}{z})^2\right)\right] \tag{10}$$

O problema agora consiste em quando devem ser considerados todos os termos desta aproximação ou quando apenas o primeiro termo é suficiente. Note que a quantidade ρ aparece duas vezes na integral, uma delas no termo exponencial, e outra no denominador do integrando. Quando ρ aparece no denominador do integrando é suficiente aproximá-lo por z, porém quando aparece no termo exponencial deve-se considerar os três termos da aproximação, pois ρ aparece na exponencial multiplicado pelo valor k, no qual um valor típico seria 10^7 na região visível do espectro, ou seja, qualquer pequena variação no termo ρ causaria erros críticos no valor da exponencial, além disso a fase é sensível a pequenas variações destes valores.

A expressão resultante para o campo da imagem (x,y) fica:

$$b(x,y) = \frac{z}{i\lambda}\int\int h(\xi,\eta) r(\xi,\eta) \frac{\exp(ikz\left[1 + \frac{1}{2}\left((\frac{x-\xi}{z})^2 + (\frac{y-\eta}{z})^2\right)\right])}{z^2} d\xi d\eta \tag{11}$$

Colocando o termo constante para a fora da integral e, simplificando o termo z:

$$b(x,y) = \frac{\exp(ikz)}{i\lambda z}\int\int h(\xi,\eta) r(\xi,\eta) \exp\left(ikz\left[\frac{1}{2}\left((\frac{x-\xi}{z})^2 + (\frac{y-\eta}{z})^2\right)\right]\right) d\xi d\eta \tag{12}$$

Definindo a função:

$$G(x-\xi, y-\eta) = \exp\left(ikz\left[\frac{1}{2}\left((\frac{x-\xi}{z})^2 + (\frac{y-\eta}{z})^2\right)\right]\right) \tag{13}$$

Expandindo os termos quadrados da função G:

$$G(x-\xi, y-\eta) = \exp\left(\frac{ik}{2z}\left(x^2+y^2-2x\xi-2y\eta+\xi^2+\eta^2\right)\right) \tag{14}$$

$$G(x-\xi, y-\eta) = \exp\left(\frac{ik}{2z}\left(x^2+y^2\right)\right)\exp\left(\frac{ik}{2z}\left(\xi^2+\eta^2\right)\right)\exp\left(\frac{-ki}{z}\left(x\xi+y\eta\right)\right) \tag{15}$$

Substituindo G na Eq.(12), e sabendo que $k = \frac{2\pi}{\lambda}$,

$$b(x,y) = \frac{\exp(ikz)\exp\left(\frac{i\pi}{z\lambda}\left(x^2+y^2\right)\right)}{i\lambda z}\int\int h(\xi,\eta)r(\xi,\eta)\exp\left(\frac{i\pi}{z\lambda}\left(\xi^2+\eta^2\right)\right)\exp\left(\frac{-2\pi i}{z\lambda}\left(x\xi+y\eta\right)\right)d\xi d\eta \tag{16}$$

Fazendo uma troca de variáveis, $\nu = x/z\lambda$ e, $\mu = y/z\lambda$, o resultado anterior torna-se:

$$b(\nu,\mu) = \frac{\exp(ikz)\exp\left(i\pi z\lambda\left(\nu^2+\mu^2\right)\right)}{i\lambda z}\int\int h(\xi,\eta)r(\xi,\eta)\exp\left(\frac{i\pi}{z\lambda}\left(\xi^2+\eta^2\right)\right)\exp\left(-2\pi i\left(\nu\xi+\mu\eta\right)\right)d\xi d\eta \tag{17}$$

Deste resultado conclui-se que o campo difratado $b(\nu,\mu)$ é a transformada de Fourier do holograma $h(\xi,\eta)$ multiplicada pela função da onda de referência $r(\xi,\eta)$ e a "chirp function" $\exp\left(\frac{i\pi}{z\lambda}\left(\xi^2+\eta^2\right)\right)$, onde esta última função é uma aproximação quadrática da função de onda esférica.

O holograma digital consiste de N x M valores discretos, cada um referente a um pixel do CCD de tamanho $\Delta\xi \times \Delta\eta$. Desta maneira, pode-se dizer que o número e o tamanho dos pixels do CCD definem a discretização:

$$b(n,m) = \frac{e^{ikz}e^{\left(i\pi z\lambda\left(\frac{n^2}{N^2\Delta\xi^2}+\frac{m^2}{M^2\Delta\eta^2}\right)\right)}}{i\lambda z}\sum_{dx=0}^{N-1}\sum_{dy=0}^{M-1}h(\Delta\xi,\Delta\eta)r(\Delta\xi,\Delta\eta)e^{\left(\frac{i\pi}{z\lambda}\left(dx^2\Delta\xi^2+dy^2\Delta\eta^2\right)\right)}e^{\left(-2\pi i\left(\frac{dx.n}{N}+\frac{dy.m}{M}\right)\right)} \tag{18}$$

Onde as dimensões do pixel no campo reconstruído são:

$$\Delta x = \frac{z\lambda}{N\Delta\xi} \quad e \quad \Delta y = \frac{z\lambda}{M\Delta\eta}$$

Na holografia interferométrica o termo em frente a Eq.(18) pode ser omitido. Este termo não depende do holograma $h(\xi,\eta)$ e, sua contribuição ao valor de fase é a mesma para os dois estados do objeto (deformado e não deformado). Conseqüentemente a omissão deste termo não modifica o cálculo da diferença de fase.

3. Termo dc

A interferência das ondas de referência e do objeto no CCD da câmera gera um efeito na reconstrução digital da imagem caracterizado por um quadrado brilhante no centro da imagem. O significado físico deste quadrado, conhecido como termo dc, é a difração de ordem zero da onda de referência.

O termo dc pode ser eliminado através da subtração dos termos referentes aos campos de onda de referência e do objeto adquiridos separadamente em duas tomadas (Kreis e Jüptner, 1997).

$$h' = h - |O| - |R| \tag{19}$$

Onde $|O|$ é a intensidade de luz da onda do objeto e $|R|$ a intensidade da onda de referência.

A desvantagem deste método de eliminar o termo dc é que o objeto não pode sofrer nenhum movimento enquanto o holograma original h e a onda do objeto $|O|$ são gravados. Kreis e Jüptner (1997) propõem outras maneiras de eliminar este termo dc. A primeira delas sugere que o holograma modificado h' seja calculado a partir da subtração da média global de intensidades dos pixels do holograma original h, ou seja,

$$h' = h - \frac{1}{NM}\sum_{i=0}^{N-1}\sum_{j=0}^{M-1} h(i,j) \tag{20}$$

Onde, N e M são o número de pixels na direção x e y da imagem. Este método de eliminar o termo dc pode ser interpretado como um filtro do tipo passa alta. Seguindo esta mesma interpretação outros tipos de filtros podem ser aplicados para se alcançar semelhante resultado.

Bons resultados foram alcançados com um filtro que remove a média local em regiões de tamanho 3x3:

$$\begin{aligned} h'(k,l) = h(k,l) - \frac{1}{9}[&h(k-1,l-1) + h(k-1,l) + h(k-1,l+1) + h(k,l-1) + h(k,l) + \\ &h(k,l+1) + h(k+1,l-1) + h(k+1,l) + h(k+1,l+1)] \end{aligned} \tag{21}$$

O holograma h', que agora será utilizado na reconstrução digital da onda do objeto, possui intensidades positivas e negativas. Embora opticamente isto não faça sentido, matematicamente é coerente, pois as intensidades relativas dos pixels da imagem não se alteram após a eliminação do termo dc.

4. Cálculo de Intensidade e Fase

O campo de onda reconstruído numericamente é complexo. A intensidade e a distribuição de fase são calculadas por (Hacht, 1974):

$$I(n,m) = b(n,m).b^*(n,m) \tag{22}$$

e

$$\phi(n,m) = \arctan\frac{Im(b(n,m))}{Re(b(n,m))} \tag{23}$$

5. Holografia Digital Interferométrica

Na holografia interferométrica clássica os campos de onda de dois estados de um objeto são reconstruídos simultaneamente, resultando em um interferograma (Vest, 1979). Na Holografia Digital este processo consiste na adição de dois hologramas digitais. A reconstrução numérica gera um campo cujas intensidades são o interferograma.

Se os dois hologramas são individualmente reconstruídos e, suas distribuições de fase ϕ_1 e ϕ_2 são calculadas a partir da Eq.(23), então a diferença de fase modulada em 2π pode ser determinada por :

$$\Delta\phi(n,m) = \begin{cases} \phi_2(n,m) - \phi_1(n,m) & \text{se } \phi_2(n,m) \geq \phi_1(n,m) \\ \phi_2(n,m) - \phi_1(n,m) + 2\pi & \text{se } \phi_2(n,m) < \phi_1(n,m) \end{cases} \tag{24}$$

ou equivalentemente (Kreis *et al.*, 1991),

$$\Delta\phi(m,n) = \arctan 2\frac{Im(b_2(n,m).b_1^*(n,m))}{Re(b_2(n,m).b_1^*(n,m))} \tag{25}$$

5.1. Cálculo de Deslocamento

A alteração de fase $\Delta\phi$ introduzida por um deslocamento $\vec{d}$ do objeto pode ser expressa por (Pedrini et al, 1998):

$$\frac{\lambda * \{\Delta\phi\}}{2\pi} = |\vec{p}| * \{\vec{d}\} \tag{26}$$

Onde, λ é o comprimento de onda do feixe luminoso, $\Delta\phi$ é a diferença de fase no ponto, antes e depois do deslocamento, $\vec{p}$ é o vetor sensibilidade que depende da geometria do arranjo holográfico e, $\vec{d}$ é o vetor deslocamento.

5.2. Sensibilidade no Plano e Fora do Plano da Superfície

Uma configuração sensível a deslocamentos do objeto que ocorrem na direção normal a superfície do objeto é mostrada na Fig.(1), situação referenciada também como sensibilidade "fora do plano" do objeto (Goodman, 1996). Esta configuração é sensível (vetor sensibilidade $\vec{p}$) a deslocamentos do objeto que ocorrem na direção da soma dos vetores de iluminação e de observação $\vec{n}_1$ e $\vec{n}_2$.

$$\vec{p} = \vec{n}_1 + \vec{n}_2 \tag{27}$$

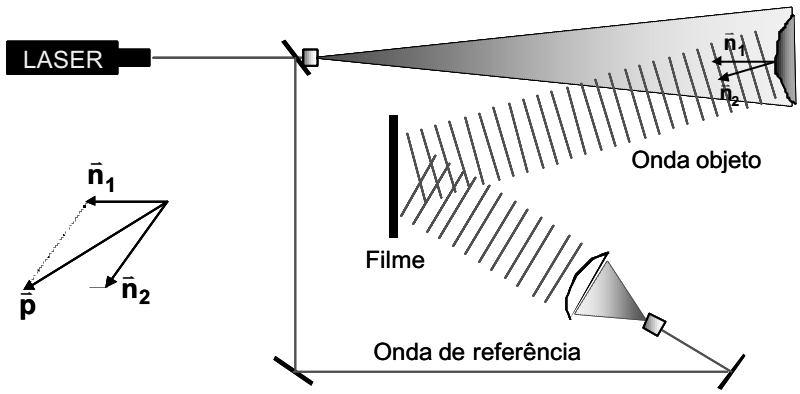

Figura 2- Configuração para medição de deslocamentos no plano

A configuração sensível a deslocamentos do objeto que ocorrem na direção tangente a superfície do objeto é representada na Fig.(5), situação referenciada também como sensibilidade "no plano" do objeto (Sciamarella, 1976). Seja $\vec{n}_1$ o vetor unitário apontando na direção da iluminação 1 (I_1) e $\vec{n}_2$ o vetor unitário apontando na direção de iluminação 2 (I_2), no caso particular em que $\vec{n}_1$ e $\vec{n}_2$ são orientados simetricamente em relação a normal à superfície do objeto, o vetor sensibilidade aponta numa direção paralela à superfície do objeto, ou seja, a configuração é sensível a deslocamentos da superfície que ocorrem na direção da diferença dos vetores $\vec{n}_1$ e $\vec{n}_2$ (Fig.(3)).

$$\vec{p} = \vec{n}_1 - \vec{n}_2 \tag{28}$$

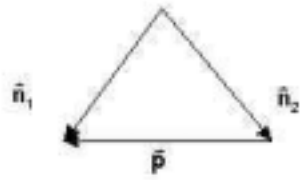

Figura 3 – Representação vetorial de uma configuração para medição de deslocamentos fora do plano

6. Medição de Deslocamentos no Plano

A técnica de medição de deslocamentos no plano consiste da aquisição de quatro imagens, cada uma referente a um estado do objeto e, uma fonte de iluminação I_1 ou I_2, como mostra a Fig.(5). A tabela a seguir mostra como estas imagens são geradas:

Tabela 1 - Aquisição de imagens para medição de deslocamentos no plano e fora do plano

IMAGENS	Interferência	Estado do Objeto	Holograma
1	I_1 + Onda Referência	Não deformado	H_1
2	I_2 + Onda Referência	Não deformado	H_2
3	I_1 + Onda Referência	Deformado	H_3
4	I_2 + Onda Referência	Deformado	H_4

Os quatro hologramas são gravados digitalmente e combinados dois a dois de acordo com o tipo de fonte utilizada, ou seja, H_1 é somado a H_3 e, H_2 é somado à H_4. A soma dos hologramas fisicamente equivale à sua superposição. Como resultado deste processo são obtidos dois hologramas gerados com iluminação simples. A reconstrução da imagem e o cálculo de fase são feitos numericamente através da formulação discutida no item 2. O fluxograma a seguir mostra o cálculo da diferença de fase para cada um dos hologramas separadamente.

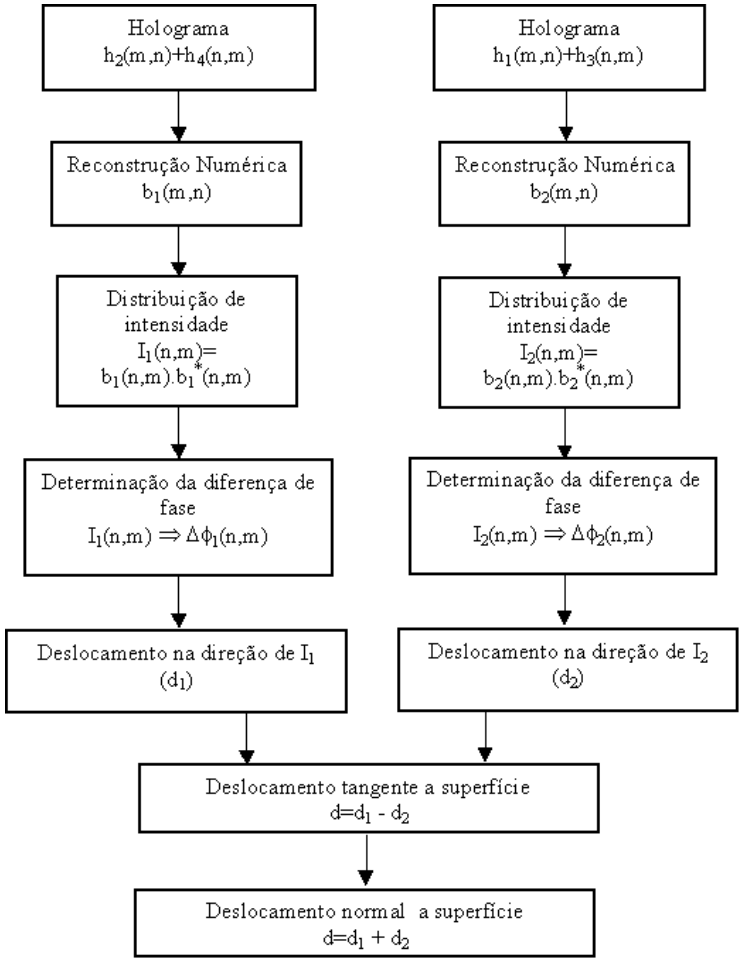

Figura 4 - Fluxograma para o cálculo do deslocamento no plano e fora do plano

Tendo calculado os deslocamentos fora do plano a partir da Eq.(26) , os valores de deslocamentos tangentes e normais à superfície são calculados através de subtração e soma vetorial respectivamente.

7. Medição de uma Viga Engastada

O objeto em medição é uma viga engastada de aproximadamente 101 mm de comprimento. Um deslocamento de 0,05 mm foi aplicado na viga através de um parafuso micrométrico localizado a 5,8 mm da extremidade livre. Com o propósito de limitar o ângulo entre a onda de referência e a onda do objeto, somente uma pequena parte da viga próxima ao engaste, cerca de 18 mm, foi iluminada. A distância utilizada entre a viga e o CCD foi de 1,03 m.

Para a iluminação foi utilizado um laser He-Ne de 30 mW de potência e comprimento de onda de 633 nm. Um holograma para cada um dos estados da viga (carregada e não carregada) foi gravado e tiveram o termo dc eliminado numericamente.

A configuração básica utilizada no experimento é apresentada na Fig.(5). Nesta configuração dois feixes de laser iluminam o objeto em duas direções simétricas.

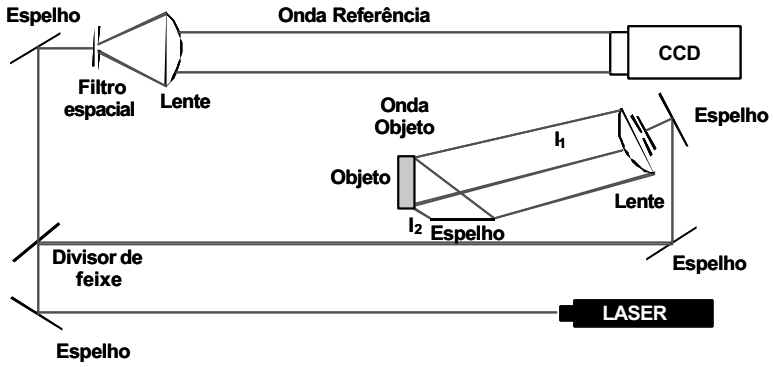

Figura 5 – Configuração para medição de deslocamentos no plano e for a do plano

O feixe de laser foi dividido em uma onda de referência e duas ondas que iluminam o objeto. A onda de referência foi expandida por um conjunto de lentes e ilumina diretamente o CCD. A imagem da câmera produz um sinal de saída contendo 1024 x 1024 pixels e 256 níveis de cinza por pixel.

Utilizando a formulação para a reconstrução numérica, foi implementado um algoritmo para o cálculo de intensidade e fase da onda reconstruída.

Para determinação da interferência de fase, a fase dos hologramas para cada um dos estados da viga considerando cada uma das iluminações (Tab.(1)) foram determinadas individualmente a partir da Eq.(23).

(a) Fase de H_1 (b) Fase de H_2 (c) Fase de H_3 (d) Fase de H_4

Figura 6 – Fase dos Hologramas descritos na Tab.(1).

A subtração destes mapas de fase com a Eq.(24) resulta na interferência mostrada na Fig.(7).

(a) Interferência de fase dos hologramas gerados com iluminação 1 (Interferência$_1$=H1-H_3)

(b) Interferência de fase dos hologramas gerados com iluminação 2 (Interferência$_2$=H_2-H_4)

Figura 7 - Interferências de fase moduladas em 2π calculadas diretamente dos hologramas digitais

Os deslocamentos normal e tangente à superfície da viga foram determinados a partir da soma e subtração das interferências (a) e (b) da Fig.(7).

(a) (b)

Figura 8 – Mapas de fase correspondentes aos deslocamentos (a) normal e (b) tangente à superfície da viga

O mapa de fase correspondente ao deslocamento tangente à superfície da viga mostra que um deslocamento de 0,05 mm na extremidade livre da viga gera um deslocamento na região próxima ao engaste significativamente maior na direção normal do que na direção tangente à superfície. A Fig.(9) mostra a mesma viga porém com um deslocamento de 0,15 mm na sua extremidade livre.

(a) (b)

Figura 9 - Mapas de fase correspondentes aos deslocamentos (a) normal e (b) tangente à superfície da viga

7.1. Comparação entre Holografia Digital e Método Analítico

Um algoritmo para remoção do salto de fase (Jones e Wykes, 1989) foi utilizado para transformar a fase, modulada em 2π, em valores contínuos de fase. A Fig.(10) mostra graficamente os campos de deslocamento obtidos com Holografia Digital, referente a um deslocamento de 0,05 mm na extremidade livre da viga, e o calculado analiticamente. O gráfico da Fig.(10.b) foi obtido a partir da equação de uma viga engastada para o caso bidimensional (Roark, 1965), por este motivo não mostra a variação do deslocamento ao longo da largura da viga.

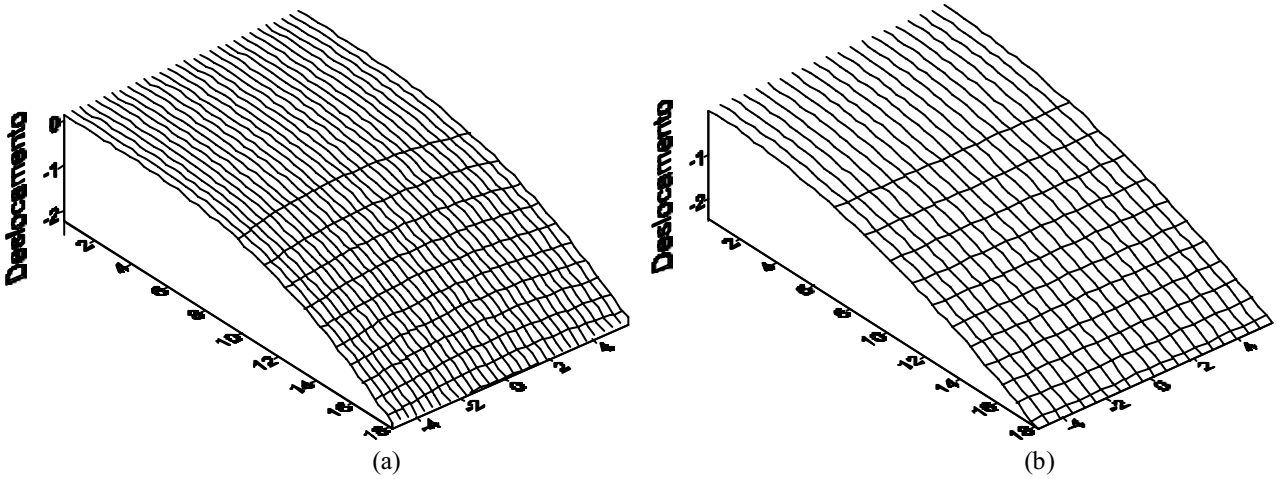

(a) (b)

.

Figura 10 – Campos de deslocamento normal à superfície calculados por (a) Holografia Digital e (b) Método Analítico

O resultado da Fig.(10) pode ser melhor analisado através de curvas de nível, como mostra Fig.(11).

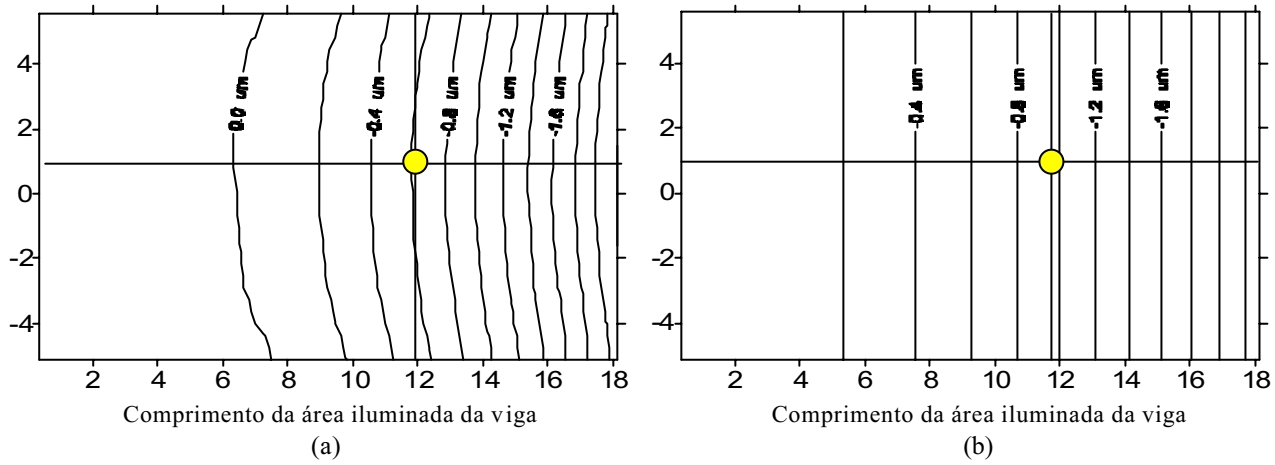

Figura 11 – Curvas de nível dos deslocamentos normal à superfície por (a) Holografia Digital (b) Método Analítico

Tomando como parâmetro de comparação o ponto mostrado na figura (11.a), o deslocamento neste ponto foi de 0.60 micrometros. O valor do deslocamento calculdado neste mesmo ponto pelo método analítico é 0.95 micrometros, ou seja, um erro de aproximadamente 0.35 micrometros. Apesar da região iluminada não ser precisamente a mesma que foi simulada para o caso ideal, este resultado qualitativo mostra a ordem dos erros que se pode esperar com a técnica.

8. Conclusões

A simplicidade e a qualidade dos resultados obtidos com holografia digital são os seus grandes atrativos. Sem lentes ou outros dispositivos para formação da imagem, a responsabilidade pela reconstrução da imagem e dos mapas de fase é totalmente transferida para o computador. Potencialmente esta técnica cria caminhos e oportunidades para que dispositivos compactos e robustos possam ser idealizados em um futuro próximo. Um estudo está sendo desenvolvido para simplificar ainda mais o método através da aquisição de hologramas de iluminação dupla, este tipo de configuração reduziria o número de imagens adquiridas e conseqüentemente o tempo computacional dispendido no momento da reconstrução numérica.

A Holografia Digital não é exatamente uma técnica nova. Os primeiros artigos foram publicados em 1996. Entretanto, há detalhes de implementação que não são abordados nos artigos e na bibliografia especializada e que devem ser "descobertos" por conta própria.

Através dos ensaios apresentados neste trabalho os autores foram bem sucedidos ao implementar a Holografia Digital e aplicá-la em um ensaio simples, onde os resultados foram comparados com resultados obtidos analiticamente.

9. Referências

Boettger, J., 1998. "Desenvolvimento de um Sistema Portátil para Medição de Tensões Residuais em Campo Utilizando a Holografia Eletrônica e o Método do Furo". Dissertação de Mestrado. Departamento de Engenharia Mecânica. UFSC.

Carcolé, E., Campos, J. and Bosch, S., 1994. "Diffraction Theory of Fresnel Lenses Encoded in Low-Resolution Devices". Applied Optics, Vol. 33, No 2, 162-174.

Goodman, J. W., 1996. "Introduction to Fourier Optics". McGraw-Hill Companies, Inc., New York, 2nd Edit.

Hacht, E., Zajac, A., 1974. "OPTICS". Addison-Wesley Publishing Company. EUA.

Jones, R., Wykes, C., 1989, "Holographic and Speckle Interferometry". Cambridge University Press.

Kobayashi, A. S., 1989. "Handbook on Experimental Mechanics". Society for Experimental Mechanics Inc, Prentice-Hall Inc.

Kreis, Th. and Jüptner, W., 1997. "Principles of Digital Holography". Proc of Fringe 97, 3rd Intern. Workshop on Automatic Processing of Fringe Patterns, 353-363.

Kreis, Th., Jüptner, W. and Geldmacher, J., 1998. "Principles of Digital Holographic Interferometry". Laser Interferometry IX: Techniques and Analysis, Proc. SPIE. Vol. 3478, 45-54.

Pedrini, G., et al., 1998. "In-Line Digital Holographic Interferometry". Applied Optics, Vol. 37, No 26, 6262-6269.

Roark, R. J., 1965. "Formulas for Stress and Strain". McGraw-hill.

Vest, C. M., 1979. "Holographic Interferometry". John Wiley & Sons, Inc.

IN PLANE AND OUT OF PLANE DISPLACEMENTS MEASUREMENTS USING DIGITAL HOLOGRAPHY

Analucia Vieira Fantin
Universidade Federal de Santa Catarina, SC,
Laboratório de Metrologia e Automatização
Campus Universitário – Trindade – 88040-970, Florianópolis, SC, Brasil
avf@labmetro.ufsc.br

Armando Albertazzi Gonçalves Jr.
Universidade Federal de Santa Catarina, SC,
Laboratório de Metrologia e Automatização
Campus Universitário – Trindade – 88040-970, Florianópolis, SC, Brasil
albertazzi@labmetro.ufsc.br

Abstract: *After the development of high-resolution CCD cameras, Digital Holography was made possible and has been more and more used in laser metrology. The hologram of an object is formed on the CCD of a high-resolution camera and it is stored electronically. No lens or other imaging device is required. The reconstruction is done numerically from the digitally stored holograms. The intensity and phase can be calculated from the digitally sampled holograms. A comparison of the phases reconstructed from digital holograms of the same object in both undeformed and deformed states allow direct determination of the interference phase. This work presents the mathematical model to numerical reconstruction. The available bibliography is related to Digital Holography using Simple Illumination. This work proposes the development of another configuration using Double Illumination techniques to measure in plane displacements. A practical application of Digital Holography is discussed. This kind of configuration improves the fringe quality compared to other optical measurement techniques.*

Keywords: *Digital Holography; Interferometry, Optical Metrology, Non-Destructive Measurements.*

XVI CONGRESSO BRASILEIRO DE ENGENHARIA MECÂNICA
16th BRAZILIAN CONGRESS OF MECHANICAL ENGINEERING

Anisotropic Etching of Si for Micromachining Applications Using $SF_6/CH_4/O_2/Ar$ Plasma

S. Moshkalyov*, C. Reyes-Betanzo, J. Swart
Centro de Componentes Semicondutores –CCS, UNICAMP, C.P. 6061, CEP. 13083-970, Campinas, SP.
***e-mail:** stanisla@led.unicamp.br

Abstract
Dry anisotropic etching of silicon is an important technology for fabrication of MEMS (micro-electromechanical systems). Dry etching has distinct advantages for anisotropic Si processing as compared with wet etching, as it does not depend on crystallographic effects, and both mono- and polysilicon can be processed in the same way. Reactive ion etching of silicon in RF (13.56 MHz) parallel plate reactor using $SF_6/O_2/Ar$ and $SF_6/CH_4/O_2/Ar$ gas mixtures was studied. Etch rates and anisotropy of etch profiles were examined as functions of gas composition, material of electrode, RF power. As a mask material, thin Al films deposited by evaporation, were used. After experiments, etch depths were measured using Dektak stylus meter, and etch profiles were analyzed by scanning electron microscope. High anisotropy of etching (with the ratio of lateral to vertical etch rates lower than 10) and good surface morphology was realized for $SF_6/CH_4/O_2/Ar$ mixtures with etch depths of 10 micrometers or more and etch rates ~200-400 nm/min. Anisotropic etching mechanism is based on ion-enhanced inhibitor etching, with lateral etching suppressed due to polimer deposition and/or oxidation. Without using CH_4 ($SF_6/O_2/Ar$ case), high anisotropy of etching could not be achieved. The roles of different plasma components in anisotropic silicon etching is discussed.

Keywords: MEMS, silicon, deep etching, plasma, anisotropy.

1. Introduction

Deep anisotropic etching of silicon is an important step in many technologies used for fabrication of micro-devices [1-5]. As etch depths for many devices may exceed dozens of microns, high etch rate is an important requirement. Fluorine-containing gases like SF_6, are known to provide high etch rates of silicon (in the order of 1 micron/min). However, etching by fluorine is mostly chemical/spontaneous, and in the case of etching in SF_6 (with or without addition of inert gases as Ar), the resulting etching profiles are usually isotropic. To improve anisotropy, additions of another gases promoting lateral etching inhibition are necessary.

Addition of oxygen to SF_6 was shown to improve considerably etching anisotropy due to oxidation of silicon surface [6]. The etch inhibiting effect is stronger at walls where there is no ion bombardment. Oxidation affects the vertical etch rate to the less degree, as the oxidized silicon layer is removed by ion bombardment during etching. It should be noted that strong ion bombardment is required to achieve relatively high etch rates. However, due to various mechanisms (like ion-induced instability and micromasking) in many cases very rough silicon surface ("black silicon") is produced by etching in SF_6/O_2 plasmas [1]. Furthermore, our studies have shown that it is difficult to achieve both very high anisotropy and high etch rate in the $SF_6/O_2/Ar$ case. At higher oxygen content, strong reduction of silicon etch rate to levels well below 0.5 micron/min is observed which is unacceptable for deep etching purposes.

As an alternative, addition of polymer-forming gases like CHF_3 to SF_6/O_2 has been proposed and smooth anisotropic silicon etching achieved using gas mixture $SF_6/O_2/CHF_3$ [1]. The role of CHF_3 in the process is not completely clear. Note that two points are important: surface roughness and anisotropy. Regarding the first problem, it has been argued that CHF_3 forms a polymer film at the etch surface which helps to remove the oxidized surface layer, thus preventing strong surface roughening. Concerning the anisotropy, it is not well understood which mechanism is most important in inhibition of lateral etching: polymerization or oxidation. In our experiments, instead of CHF_3 we tried to use CH_4 which is much more common, cheap and easy attainable. In most experiments, argon was also added, in order to stabilize plasma and to provide higher ion bombardment. The results obtained show that quite fast, smooth and anisotropic etching of silicon utilizing $SF_6/CH_4/O_2/Ar$ mixture is possible. The results will be used in a program of MEMS development (sensors, actuators) which is now in progress in the CCS – UNICAMP.

2. Experimental set-up

In the experiment, a capacitively coupled RF-driven (13.56 MHz) asymmetric plasma reactor made of stainless steel was used. RF power was applied to a smaller water cooled Al electrode (12 cm in diameter). The bigger upper electrode is electrically connected to the chamber walls. The lower powered electrode in some experiments was covered by a 100-mm Si wafer. A DC potential between electrodes (which is nearly equal to the self-bias existing between the plasma and the smaller electrode in an asymmetric reactor) was measured.

Experiments were performed with p-type (100) silicon samples patterned by a thick (2-4 micron) Al mask. For primary tests, usually small samples (with areas of ~ 0.2-0.5 cm^2) were placed in the center of the electrode or Si wafer used

as a sample holder. Practically the same results were reproduced with bigger samples with area of up to 5-15 cm^2, suitable for MEMS applications. Etch depths were measured by a stylus profiler DEKTAK. In most experiments the etch time was 10 min. To achieve higher etch depths, the plasma can be run for 1 hour or more. Mixtures of gases containing SF_6, CH_4, O_2 and Ar in different compositions were used for etching. Most of experiments were carried out at a pressure of 60 mTorr, total gas flow of about 50 sccm, with RF power ranging from 100 to 150 W, self-bias voltage between 275 and 590 V.

3. Experimental Results and Discussion

Some experimental results on etch rates achieved with different gas mixtures are shown in Figs. (1), (2) and (3). In Figure (1), the silicon etch rate is shown as a function of CH_4 flow for SF_6/ CH_4 /O_2/Ar mixture with the total flow of 55 sccm, 25 sccm of SF_6 and 15 sccm of O_2, RF power of 100 W (DC bias varied between 280 and 345 V). A local maximum is observed at a intermediate flow rate (10 sccm), followed by a fast drop of the etch rate at a higher CH_4 flow. Reduction of the etch rate in this case is probably due to strong polymerization at the silicon surface. In the experiments presented in Fig. (1), a Si wafer was used as a sample holder. It should be noted that emission spectroscopy (actinometry technique) has shown that the Si wafer consumes considerable amount of atomic fluorine [7]. In the case of SF_6 plasma, this effect usually results in significant losses in the silicon etch rate. However, for more complex gas mixtures containing CH_4, O_2 and Ar, the effect of the wafer is not trivial. In particular, lower etch rates were observed for experiments without the Si wafer, see Fig. (2). This gives the evidence that the etching regime does not depend solely on production of etching species in the plasma, other mechanisms may play important role in the surface kinetics (see below).

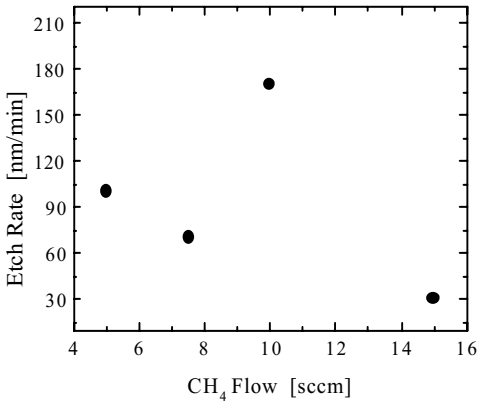

Figure 1. Si etch rate vs. CH_4 flow rate in $SF_6/CH_4/O_2$/Ar plasma.
Process conditions: 100 W, 60 mTorr, DC bias varied (280→345 V).

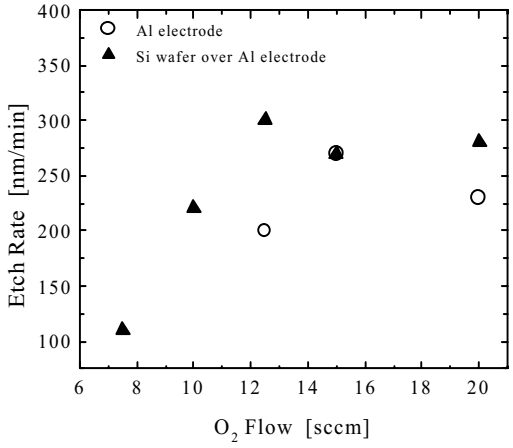

Figure 2. Si etch rate vs. O_2 flow rate in $SF_6/CH_4/O_2$/Ar plasma. Effect of Si wafer used as a sample holder.
Process conditions: 130 W, 60 mTorr, DC bias varied (340→590 V).

In Figure (3), the silicon etch rate is shown as a function of the O_2 flow for a $SF_6/CH_4/O_2/Ar$ mixture with the total gas flow of about 50 sccm, 25 sccm of SF_6 and 10 sccm of CH_4 and three different levels of RF power (100, 130 and 150 W, with DC bias varied between 280 and 590 V). It is interesting to note that the highest etch rate was obtained at intermediate power level (130 W). This indicates that, under the present experimental conditions, production of fluorine radicals (which increases rapidly with power) is not a limiting step for the process. More likely, a competition between two surface processes, polymerization and oxidation, determines the etching regime. Strong polymerization can stop completely the etching process by limiting the access of etchant (fluorine radicals) to the surface and the transport of etch products from the surface. Oxygen is known to etch efficiently polymer films, and one can expect that for oxygen-rich plasmas the surface will be polymer-free. On the other side, excess of oxygen will result in strong oxidation and reduction of the silicon etch rate. Therefore, in terms of the etch rate, the best conditions can be expected in the intermediate region where the two processes (polymerization and oxidation) are balanced. Furthermore, as the polymerization at the walls (no ion bombardment) should be more intense than at the bottom, one can also expect high anisotropy under these conditions.

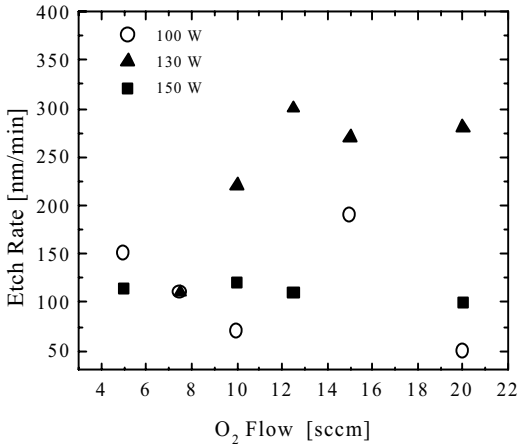

Figure 3. Si etch rate vs. O_2 flow rate as a function of RF power in $SF_6/CH_4/O_2/Ar$ plasma.
Process conditions: 60 mTorr, DC bias varied (275→500 V).

As can be seen from Fig. (3), for oxygen-deficient plasmas the polymerization dominates (the etch rate is low), then the etch rate grows with the oxygen content as polymerization is gradually reduced (see results for 130 W). Further increase of the oxygen content in the plasma leads to saturation and even decrease of the etch rate.

In Figures (4) and (5), etching profiles obtained under different plasma conditions are presented. It is seen that by increasing the oxygen content in the $SF_6/CH_4/O_2/Ar$ gas mixture, considerable improvement of etching anisotropy can be achieved, compare Figs. (4a) and (4b). Note that both experiments were performed without the Si wafer, and the "black silicon" (i.e., rough) surface was obtained. The etch rate was lower for high oxygen content. In Figure (5), it is presented an example of a highly anisotropic etch profile, with the surface roughness being considerably reduced. In this case, the "black silicon" effect disappears, thus indicating that a balance between oxidation and polymerization at the silicon surface has been achieved.

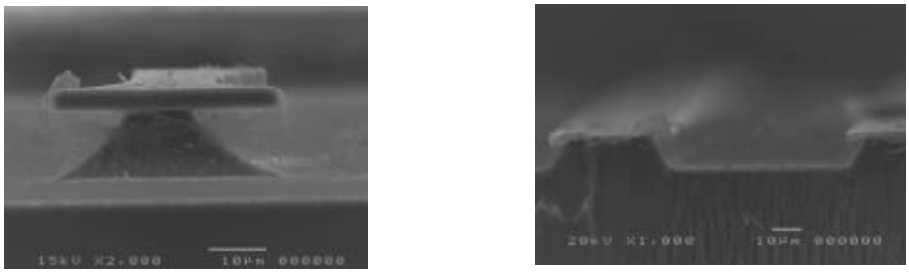

(a) (b)

Figure 4. SEM pictures of sidewall profiles in Si. Process conditions:
(a) $25SF_6/7.5CH_4/5O_2/17.5Ar$, 130 W, 60 mTorr, 435 V, 1220 nm/min.
(b) $25SF_6/7.5CH_4/10O_2/12.5Ar$, 130 W, 60 mTorr, 450 V, 1000 nm/min.

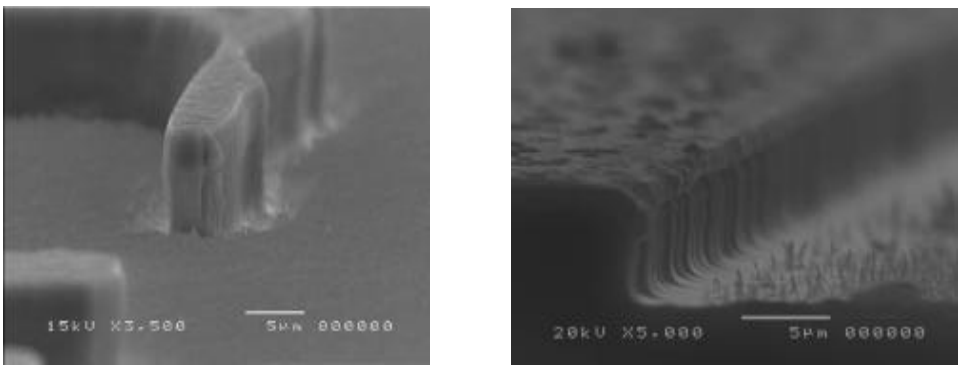

Figure 5. SEM pictures of highly anisotropic etch profiles in Si.
Process conditions: $25SF_6/10CH_4/12.5O_2/5Ar$, 150 W, 60 mTorr, 610 V, 500 nm/min (left);
$25SF_6/7.5CH_4/10O_2/12.5Ar$, 150 W, 60 mTorr, 470 V, 300 nm/min (right).

4. Conclusions

The results of experimental study of deep silicon etching in $SF_6/CH_4/O_2/Ar$ plasmas are presented. To our knowledge, this gas mixture has not been used for deep silicon etching before. It has been shown that by optimization of experimental conditions (the gas mixture, RF power, DC bias, electrode material) it is possible to obtain anisotropic etch profiles with good surface morphology and relatively high etch rates. Etching mechanisms are discussed. Further studies of the deep silicon etching for micromachining applications are on the way.

The work was supported by CNPq and FAPESP.

5. References

1. Legtenberg, R., Hansen, H., De Boer, M., and Elwenspoek, M., 1995, "Anisotropic Reactive Ion Etching of Silicon Using $SF_6/O_2/CHF_3$ Gas Mixtures", J. Electrochem. Society, v. 14 , pp. 2020-2028.
2. Rangelow, I. W., 1997, "Reactive ion etching for high aspect ratio silicon micromachining", Surf. & Coat. Technol., v. 97, pp. 140-150.
3. Lee, S., Park, S., and Cho, D., 1999, "A New Micromachining Technique with (111) Silicon", Jpn. J. Appl. Phys., v. 38, pp. 2699-2703.
4. Kurihara, K., Sekine, M., 2000, "Fabrication of Capillary Plate with Sub-Micron Holes for Investigating High-Aspect Ratio Etching Characteristics", Jpn. J. Appl. Phys., v. 39, pp. 1369-1370.
5. Park, S., Lee, S., Yi, S. and Cho, D., 1999, "Mesa-supported, Single-crystal Microstructures Fabricated by the Surface/Bulk Micromachining Process", Jpn. J. Appl. Phys., v. 39, pp. 4244-4249.
6. D'Emic, C.P., Chan, K., Blum, J., 1992, "Deep trench plasma etching of single crystal silicon using SF_6/O_2 gas mistures", J. Vac. Sci. Technol. B, v. 10 , pp. 1105-1110.
7. Reyes-Betanzo, C., Moshkalyov, S., Swart, J., Ramos, A. C., Diniz, J. A., 2001, "Study of conditions for anisotropic plasma etching of tungsten and tungsten nitride using SF_6 /Ar gas mixtures, J.Electrochem. Society, submitted.

XVI CONGRESSO BRASILEIRO DE ENGENHARIA MECÂNICA
16th BRAZILIAN CONGRESS OF MECHANICAL ENGINEERING

LTCC A KEY TECHNOLOGY FOR MODULAR MESO-SYSTEMS

Mário Ricardo Gongora Rubio
Instituto de Pesquisas Tecnológicas do Estado de São Paulo, Cidade Universitária, CEP 05508-901, São Paulo, Brazil.
e-mail: gongoram@ipt.br

Jorge Juan Santiago Aviles
Pennsylvania University, Philadelphia, USA.
e-mail: santiago@ee.upenn.edu

Edgar Charry Rodriguez
Laboratório de Sistemas Integráveis (LSI) da EPUSP, São Paulo, Brazil
e-mail: charry@lsi.usp.br

Abstract: *For certain applications (LTCC) Low Temperature Co-fired Ceramic tape materials used in multi-layer packages offers the potential of emulating a great deal of silicon sensor/actuator technology at the meso scale level.*
The goal of the present paper is to describe the state of art of modular meso-system technology (MsST) using Thick Film, Silicon and LTCC technologies in a hybrid way. A major MEMS or MST application being addressed today in microfluidics is fluid management for miniaturized chemical analytical systems and other applications.
Applications for MST-3D in the meso-size, from fifty to several hundreds of microns of feature size, requires a material system compatible with hybrid microelectronics, with suitable thermal, mechanical and electrical properties, easy to fabricate and inexpensive to process. Such material is the LTCC tape multi-layer system.
One of the important features of LTCC technology is the possibility of fabricating 3-D structures using multiple layers.
In this work we would like to present several devices and technologies showing the possibilities of the approach.

Keywords: *LTCC, Meso - system Technology, Microfluidics, Sensors & Actuators.*

1. Introduction

The emergence of MEMS/MST techniques provide the means for Micro-system devices fabrication with decreased size and cost as well as increased performance and reliability. Chemical, semiconductor & biotechnology industries have increased needs for microfluidic systems with the following requirements:

- Small sizes;
- Less dead volumes;
- Short response time;
- Minimum wettable surfaces;
- Corrosion resistant materials;
- Low power consumption;
- Non particulate generation;
- Non-moving parts that can block or clog the devices;
- Integration of several fluidic devices;
- High temperature operation
- Low cost.

MEMS/MST development has shown steady growth, pushing the frontiers of new materials and processes for applications like:

- Microsystems for chemical analysis, e.g. μTAS (Micro Total Analytical Systems);
- Microsystems for drug delivery;
- Microsystems for environmental data acquisition;
- Inertial Microsystems for disabled assistance and machine or automata stabilization;
- Hybrid Microsystems for automotive applications.

Due to the economic potential of MEMS/MST technologies, many countries have recognized these techniques as strategic and of high priority. Therefore a great deal of resources have been allocated for R&D in support of the following research areas, see site DARPA, (2000):

- Chemical analyses;
- Inertial Systems;
- Fluid handling and control;
- Distributed sensor & actuator networks.

2. LTCC Technology

Low temperature co-fired ceramic tape technology (LTCC technology) displays excellent properties for doing packaging, interconnection and passive component integration. It has been used in the last twenty years for high reliability applications in military, aviation and automotive areas, as well as in MCM's (Multi Chip Modules) for portable wireless, see Amey et all, (2000) and computer applications. Recently its extent of application has been expanded to the sensor and actuator area, rendering a technology suitable for MST as demonstrated by (Gongora-Rubio, 1999 e Bauer et all, 1999).

Main reasons for using LTCC green ceramic tapes techniques as a MST technology are:

- Simplicity of tape machining with feature size of 50μm to several mm;
- Mass production methods can be immediately applied;
- Thermo-physical properties can be promptly modified, e.g. thermal conductivity;
- Tapes of different compositions can be formulated to obtain desired layer properties,
- Multilayer interconnections (electric or fluidic) can be easily outfitted;
- Embedded passive components is a normal feature;
- Integration of electronic circuits, due to it's hybrid nature, can be readily done;
- Layer count can be high;
- Possibility of auto-packed devices fabrication;
- Fabrication techniques are simple, inexpensive and environmentally benign.

Tapes are easily machined while still in the green (before firing), they are soft, pliable, and easily abraded. It is possible to use mechanical CNC techniques (Numerical controlled milling), punching machines or Laser methods. Once the material is fired and fully sintered, it becomes tough and highly rigid. Green Ceramic Tapes are glass-ceramic composite materials. The composition includes ceramic filler, usually alumina, Al_2O_3, a glass frit binder to lower processing temperature and an organic vehicle for binding and viscosity control. This renders a material compatible with thick film technology. They are commercially produced in flat tapes of various thickness but usually in the range of 100 to 400 μm. called green ceramic tapes because they are manipulated in the green stage, that is before firing and sintering, see Bhedwar, (1990).

The important feature of Green ceramic tape technology is the fabrication three-dimensional structures using multiple layers of ceramic tapes. Each layer is machined in the green with whatever feature in the form of vias, cavities, channels, and internal electrical elements such as capacitors, resistors, and interconnections needed for the overall function of the 3D structure. Individual layers are arranged in the proper order (stacked) as to yield the desired structure, placed in registry and laminated. The location holes for registry and the vias are usually punched, although they can be chemically dissolved, etched, abraded or cutted.

The next step moves this stack to the press where heat and pressure are applied to complete the lamination process. At this point the laminates are ready for sintering in air furnace. A complete green ceramic tape processing sequence for a simple chemical reactor is depicted in Fig. 1.

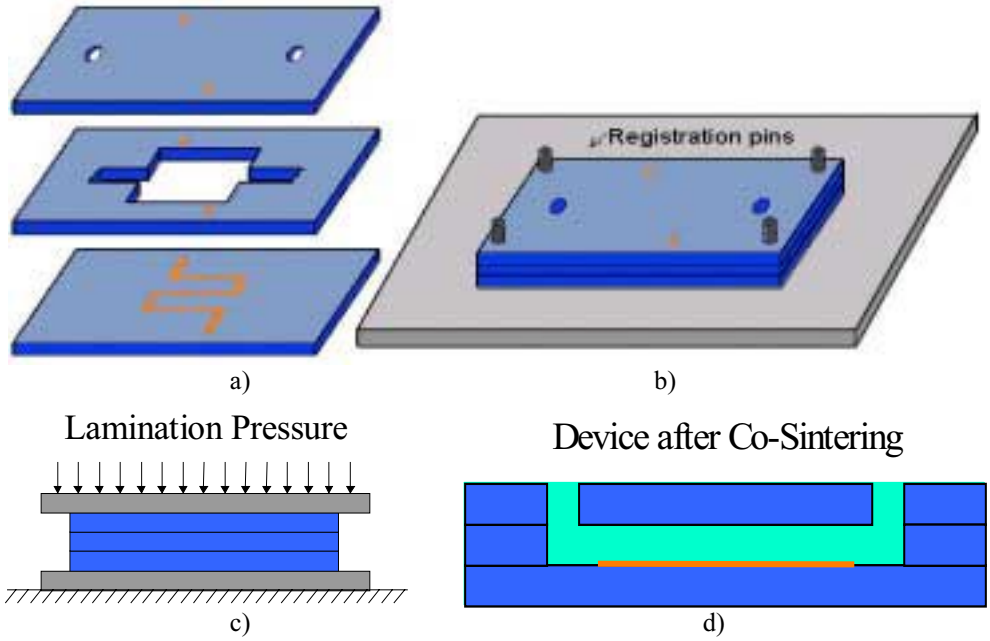

Figure. 1. LTCC for MST process sequence: a) machining each layer to create desired patterns, screen-printing and via filling through a mask, b) alignment and stacking of layers, c) lamination of layers and d) Co-firing.

The LTCC ceramics shrinks upon sintering or heat-treating. A nominal alumina LTCC formulation shrink 12 % in the x, y plane and 15 % in the z-axis, the shrinkage is uniform and predictable and can be incorporated into the design scheme. A typical alumina formulation such as the DuPont's LTCC 951 can be glued after firing to most transparent glasses when viewing ports are desired in a structure. The hermetic binding of other hybrid structures is accomplished with die-bonding glass formulations, epoxies or eutectic bonding.

Due to the high fusion temperature of materials involved in green ceramics fabrication, a sintering process is needed to convert the green ceramic tape into a solid dense material. The sintering temperature profile presents two plateaus. The first one is at 350 ^{o}C; in order to burn all organic components, the second is related to the viscous sintering process at 850 ^{o}C.

3 LTCC for MEMS/MST packaging

MEMS/MST packaging should fulfill the following requirements:

- 3D integration and good silicon efficiency;
- Electrical, mechanical, optical and fluid media interfaces have to link the microstructures to the outside world;
- Module design should provide flexibility with small package size and weight;
- Package technology should be ready for medium volume production
- All typical packaging requirements

In Figure 2 from National Semiconductor, (1999), a BGA package fabricated with LTCC technology and ball cross section is shown, this type of packages opened possibilities for the development of 3-D packaging technologies.

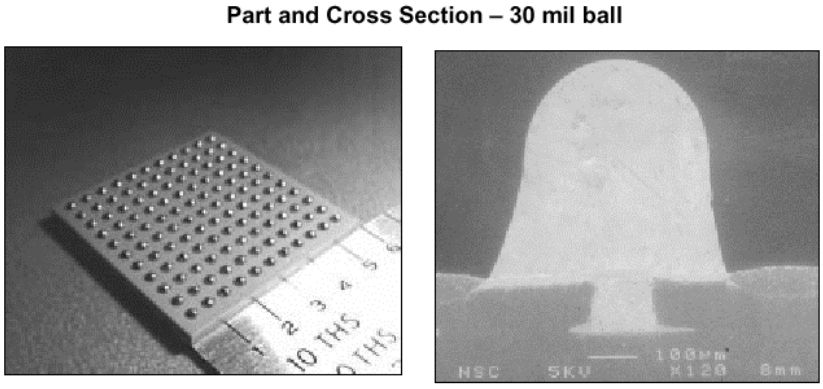

Figure. 2 BGA package fabricated with LTCC technology and ball cross section.

A packaging technology based on a double-sided Ball Grid Array named TB-BGA (Top-Bottom Ball Grid Array) has been recently proposed by Schueneman et all, (1999). This 3-D packaging concept allows several modules to be stacked, implementing a modular vertical integration technique, with electrical, fluidic, optical and communication interfaces for MEMS/MST applications, using LTCC as an enabling technology.

Figure. 3 displays the basic TB-BGA concept and a detail for electrical interfacing, showing the top land grid array, the bottom Ball Grid Array, Via Bus and an internal rewiring layer needed to connect die to the interface.

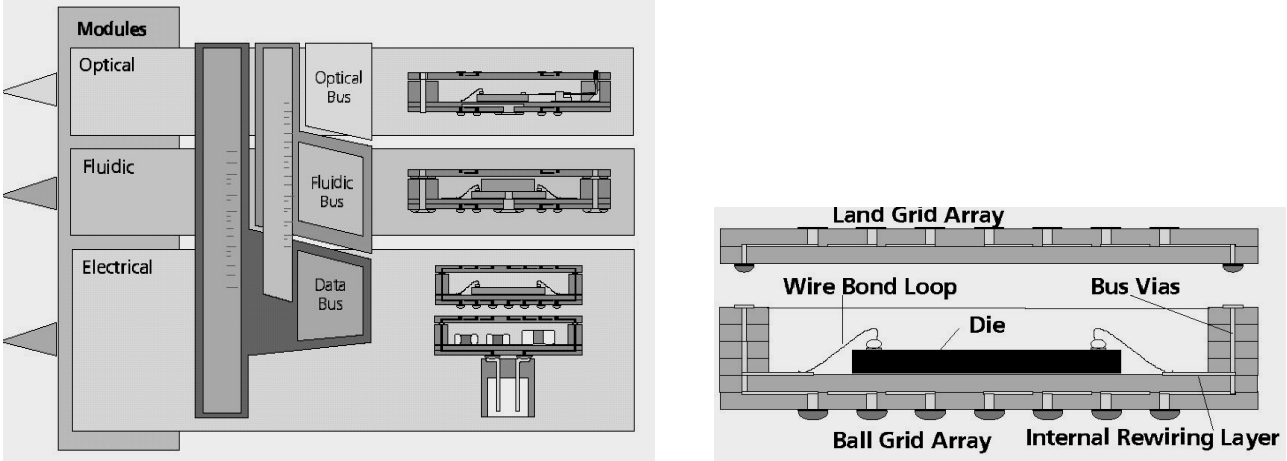

Figure. 3 TB-BGA concept and electrical interfacing, from Schueneman et all, (1999).

3. Some microfluidic devices

The new field of MEMS/MST named Microfluidics is being structured and several works in the area have been reviewed, see Gravesan, (1993). LTCC technology displays simplicity to implement channels with internal reduced dimension as well as cavities without geometrical limitations when compared with other MST technologies. In this section some basic Microfluidics applications using LTCC multi-layer ceramic tapes will be presented, specifically micro-channels, critical orifices, gas flow sensors and hot plates.

3.1. Micro-channels

Poiseuille performed studies on micro-channels in 1846. He managed to do some experiments using glass capillaries of hundreds of microns. From this study the classical expression that relates pressure drop with volumetric flow rate was obtained. Micro-channels were studied by (Pfahler, 1992 and Harley, 1995) for liquid and gas behavior on silicon substrates. Measurements performed by Moon (1998) in straight conduits display linear pressure drop for the low Reynolds number region.

In Figure 4 it is possible to verify a simple way to implement micro-channels using LTCC, in this case three layers are enough to fabricate the channel. Top layer makes media interconnection, middle layer makes the channel itself (that could be straight, in L, Y, U, spiral or any desired complex shape); bottom layer makes the device base.

Figure. 4 Three layer micro-channel implementation.

3.2 Critical Orifices

Critical orifices as nozzles are passive devices for gas flow control, using Choked flow phenomena. Choked flow happens when gas reaches sound velocity in the orifice-passing cavity. At certain critical input pressure this phenomena arises and volumetric flow remains constant despite output pressure variations as studied by (Pereira, 1990 and Kawakita, 1999). Critical orifices do not have moving parts and can control volumetric flow passively. Fig. 5 shows a critical orifice fabricated using LTCC materials and machined using CNC techniques. In addition critical orifice behavior for input pressure vs. volumetric flow and different orifice diameters (90, 180, 210 μm) is displayed.

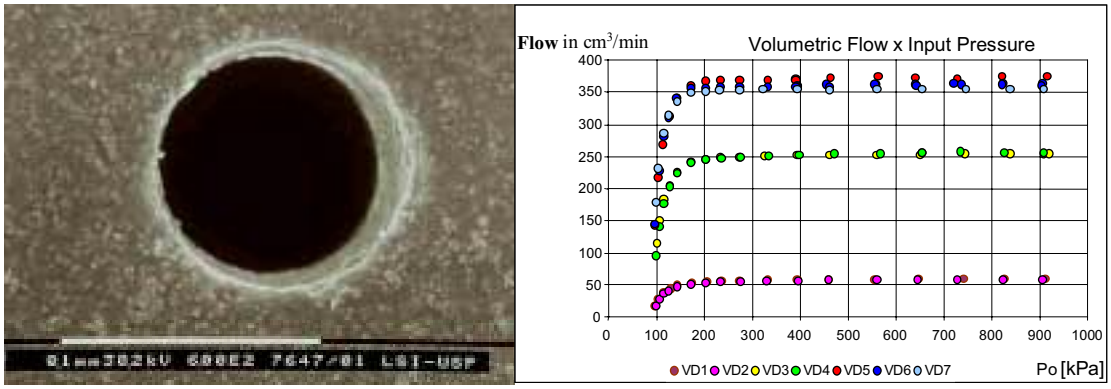

Figure. 5 Ceramic critical orifices and behavior (Flow Vs. Pressure) for several orifice diameters.

3.3 Gas flow sensor

Gongora-Rubio et all (1999) fabricated a meso-scale gas flow sensor using LTCC. The basic sensor structure consists of a thick film resistive heater and two thermistors printed on a thermally isolated bridge in a cavity. The device was fabricated following conventional LTCC technology process and sagging prevention method.

The basic sensor measures the mean temperature in bridge using two thermistors; this temperature is related to flow in the cavity. This configuration utilized five layers of 200 μm thick alumina ceramic DuPont 951. DuPont formulations for the NTC thermistor with high β constant (≈2000), together with a ruthenium-based resistor for the heater were screen-printed on the bridge. Fig. 6 depicts various layers of the basic sensor schematically as well as a SEM microphotograph of the fabricated device cross-section.

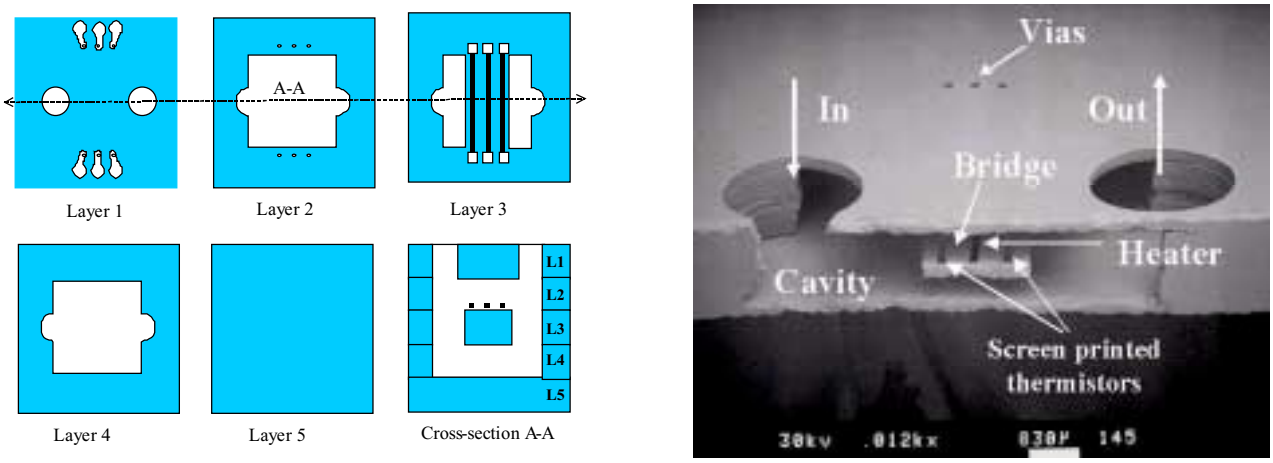

Figure. 6 Flow sensor layer count and SEM view of fabricated device.

It was investigated some sensor characteristics as flow range, sensitivity, temperature excitation, and response time of the device. Fig. 7 indicates dissipation factor of the fabricated device to diverse flow velocities in SLM (Standard Liter per Minute).

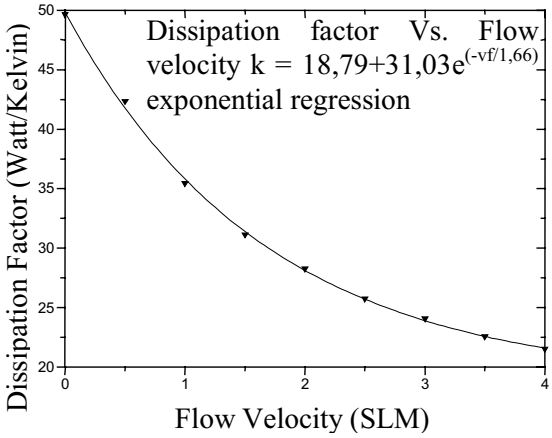

Figure. 7 Dissipation factor of fabricated device Vs. diverse flow velocities.

3.4 Hot plates

Applications for microreactors usually need rapid heating from ambient to high temperature values, and rapid cooling. We use coils to implement a simple internal cavity Joule effect heater, as shown in Fig. 8. Ceramic surface was heated due to Joule effect on coil. Different currents can be applied to obtain desired surface temperatures on cavities fabricated on the ceramic surface, see Gongora-Rubio et all (1999).

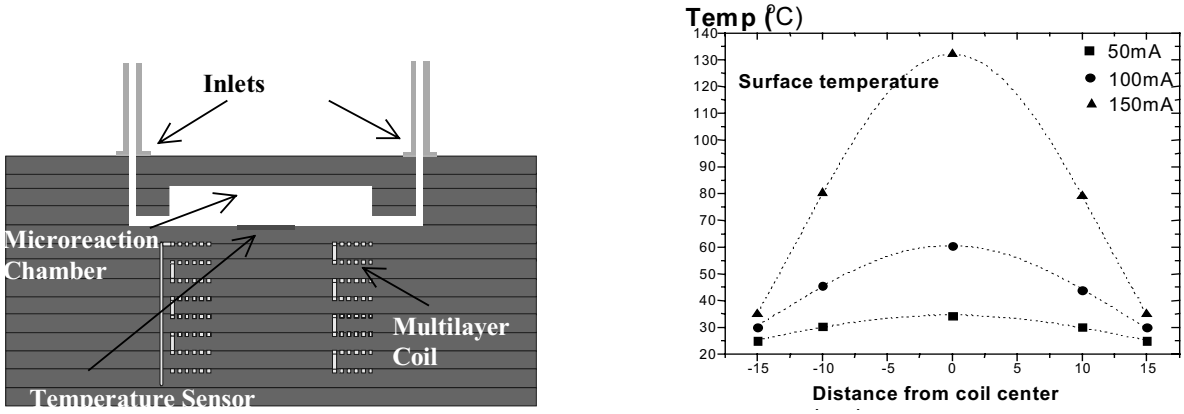

Figure. 8 Conception of cavity heaters and Surface temperature for different coil currents.

4. Actuator applications

Actuators with adequate characteristics for aggressive environments and high temperatures have been developed using low temperature co-fired ceramic tape technology. We would like to report an electro-magnetically actuated normally closed valve demonstrated by Gongora-Rubio et all, (1999).

4.1 Hybrid Micro-valve

Micro-valves are necessary to execute fluid control functions in Micro-fluidic applications, some advantages of miniaturization of this devices are:

- Small sizes;
- Short response time;
- Low power consumption;
- Low inactive volume;
- Good dynamic characteristics.

Main problems with silicon Micro-machined valves are:

- Manipulation of biological fluids having cells or bacteria with hundreds of microns;
- Moving parts used for Micro-valves can block or clog the devices.

In this work a non-moving parts hybrid electromagnetic Micro-valve, fabricated using LTCC, thick film and silicon technologies, is presented. Forces of magnetic origin can be generated by the interaction of a magnetic field intensity H with an electrical current I (Benecke et all, 1990 and Wagner et all, 1991). As a result of this force the spring generate a displacement proportional to the force divided by the equivalent spring constant k.

$$\Delta z = F_z \cdot k^{-1} \tag{1}$$

Electromagnetic techniques are suitable to hybrid meso-systems, as pointed out by Trimmer (1989) because:

- Can generate large forces;
- Can produce large displacements;
- Good performance with temperature
- Adequate velocity response
- Is a robust and non expensive technique

Using some of LTCC possibilities a hybrid micro-valve was implemented. This device has a multi-layer coil, a fluidic system and a flexible diaphragm with a magnet bonded in its topside, associated to a media interface, see cross section shown in Fig. 9.

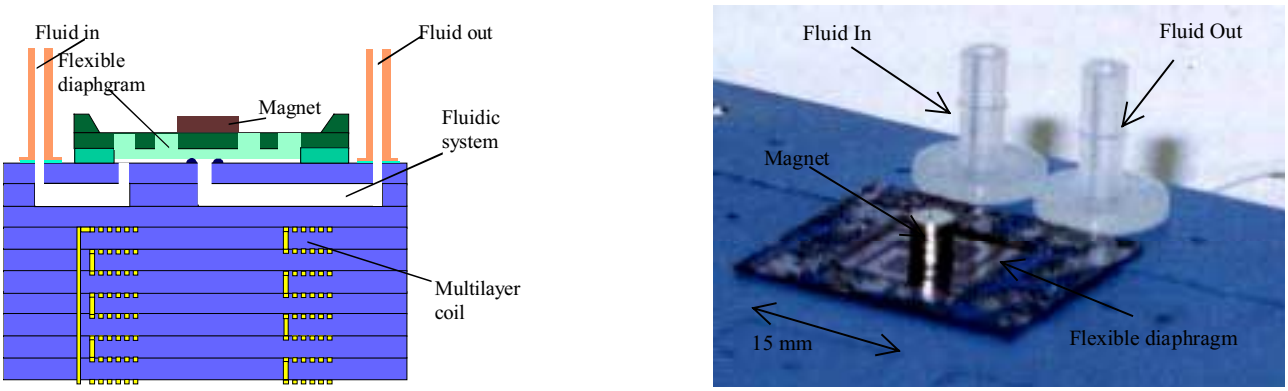

Figure. 9 Cross-section of micro-valve and fabricated device.

Multilayer coil fabrication is described elsewhere (Gongora-Rubio 1999), fluid system can be implemented, as pointed out in section 3.1, with three LTCC tapes, flexible diaphragm with a rare earth magnet attached allows electromagnetic actuation. The diaphragm was implemented using silicon technology for a spiral spring that is covered with an RTV film. Flexible diaphragm fabrication process is described in (Gongora-Rubio 1999).

Complete fabricated Micro-valve is shown in Fig. 9, it is a hybrid device which utilizes a purely LTCC tape electro-magnet and fluid flow manifold, combined with an anisotropically etched silicon rectangular planar spring, and a high-energy product SmCo mini-permanent magnet. Device dimensions are in the meso (intermediate) range with the smallest features (fluid conduit in the manifold) of 400 micrometers and the largest (the electromagnet, coil) of 12 mm.

Displacement response Vs. coil current, for several magnet-coil distances is shown Fig. 10. One can verify that at certain point diaphragm center reaches valve seat.

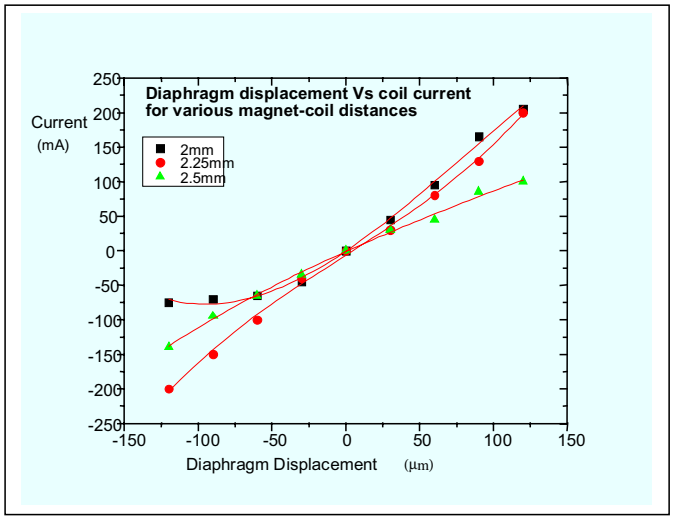

Figure. 10 Diaphragm displacements Vs. Coil current for various magnet-coil distances.

All parts of the electromagnet and the fluid flow channels were machined from DuPont 951 series, alumina based LTCC tapes utilizing either a numerically controlled milling machine, a puncher or an isotropic etching technique involving the glassy binder of a partially sintered LTCC tape. The hybrid device consists of 5 layers of planar spiral coils. This is an inexpensive, easy to fabricate meso-scale valve fabricated in the same material as many IC packaging systems. We are currently developing a meso-scale pump using the same approach reported in this work. This may lead to fluidic systems where the fluidic devices can simultaneously serve as part of the IC package.

5 Possible Meso-System applications

Meso-systems for drug delivery, biological parameter monitoring, gas or liquid chromatographs, cooling and heat exchangers, particle separators, electrophoretic cells, PCR (Polimerase Chain Reactor), micro combustion chambers and chemical microreactors, could be implemented using the techniques presented in this work. Let's take as an example of LTCC hybrid technology application in meso-systems, a well known analytical technique: FIA - Flow injection analysis, Ruzicka et all, (1975). In this technique a sample is injected in a continuous flowing carrier and is transported downstream into a detector. On its way to the detector, the sample fluid is mixed with the carrier and reagent solutions and is dispersed in a reaction coil. A detector measures the result of this reaction by optical or electrochemical sensing in a continuous flow. Block diagram of the FIA system is presented in Fig. 11.

There are several advantages for FIA miniaturization:

- Sensor can have its sensibility and selectivity optimized;
- Time for analysis is 10 to100 s, allowing up to 300 analyses/hour;
- Waste and sample size are minimized;

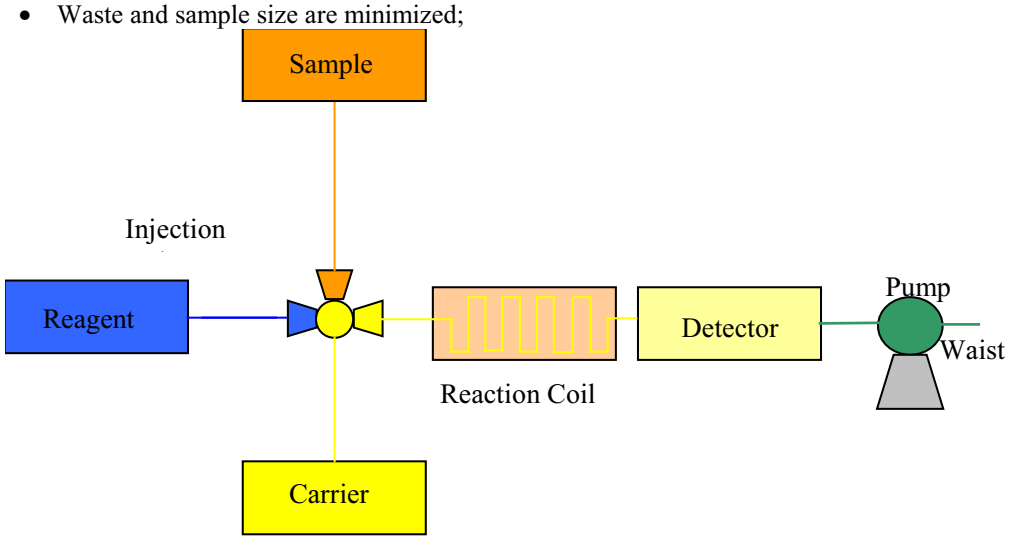

Figure. 11 Block diagram of a FIA system.

A silicon multi-electrode sensor for electro-chemical measurement is available as depicted in Fig. 12. This sort of general-purpose electrochemical sensor fabricated using silicon technology developed by Fontes et all, (1998), displays suitable characteristics for doing static or dynamic analysis, multipoint and multi-species measurements.

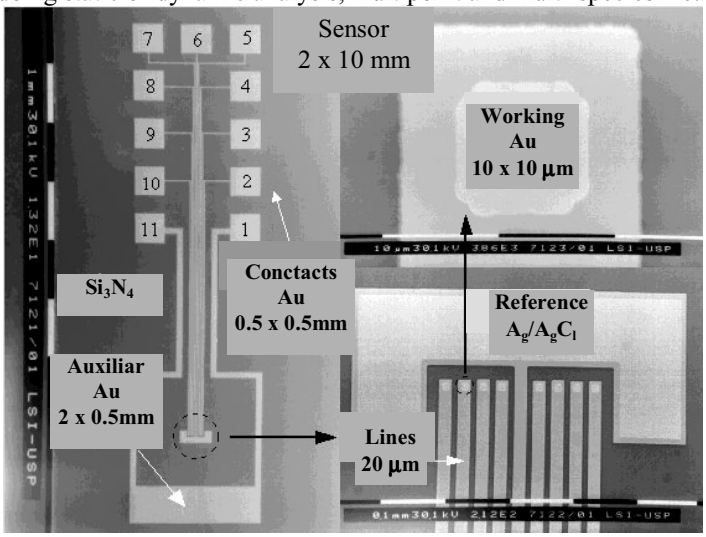

Figure. 12 Silicon multi-electrode sensor for electro-chemical measurement.

Conception of an integrated FIA system using LTCC hybrid technology is shown in Fig. 13.

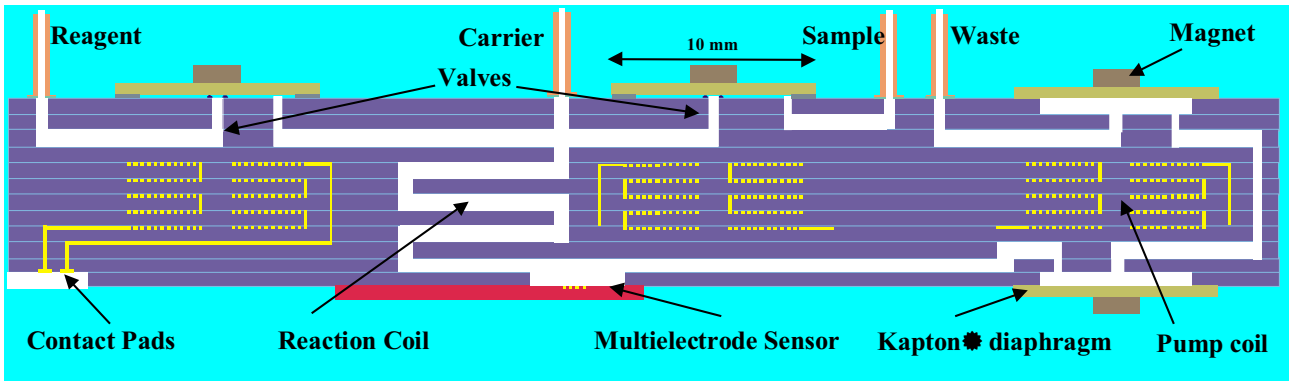

Figure. 13 FIA integrated system conception using LTCC hybrid techniques.

6. Conclusions

We have shown that LTCC multilayer ceramic technology provides several devices and methods suitable to implement microfluidic meso-systems. The ability of 3-D packaging for MEMS/MST extends application possibilities.

The suggested LTCC technology approach has the advantages of enabling custom applications, lowering prototyping costs and accelerating time to market for medium volume productions.

In this work we reported sensors, actuators and other fluidic components that can be suited for several fluidic control functions exploring LTCC ceramic multilayer tape possibilities; rendering integrated building blocks and packaging modules for more complex applications in the emerging field of MEMS/MST.

7. Aknowledgements

MRGR would like to acknowledge PRODENGE/RECOPE/FINEP for partial supporting of this research.

8. References

Amey D.I., Dirks M.T. Draut R.R. Horowitz S.J. & Needes C.R.S., 2000, “Opening the door to wireless innovations”, Advanced Packaging, p-37-39.

Bauer R, Rebenklau L, Wolter K-J & Sauer W., 1999, “Aspects of LTCC utilization for Microtechnical application” in : The third IEMT/IMC Symposium , April 21-23, Tokyo.

Benecke W.and Wagner B., 1990, “Magnetically Driven Micro-actuators: Design and Considerations”, in Micro-system Technologies 90, Berlin, p- 838, H. Reichl (ed).

Bhedwar H.C.and Sawhill H.T, 1990, “Ceramic Multilayer Package Fabrication”, Packaging, Electronic Materials Handbook, ASM (ed.), p.460-469.

Darpa Programs, 2000, http:\\www.darpa.gov.

Fontes M. B., Furlan R, Santiago Aviles J. J, Araki K. & Agnes L. 1998, “A study of modified silicon based microelectrodes for nitric oxide detection”, Ibersensor'98, First Iberoamerican Congress on Sensors and Biosensors, Havana.

Gongora-Rubio M. R., Solá-Laguna L.M., P.J. Moffet & Santiago Aviles J. J., 1999, “The utilization of low temperature co-fired ceramics -LTCC-ML -technology for meso-scale SEM, a simple thermistor based flow sensor”, Sensors-and-Actuators,-A:-Physical. v. 73 n 3, p 215-221.

Gongora-Rubio M.R., 1999, “Em direção a uma tecnologia híbrida de meso-sistemas. Sensores e atuadores com ceramicas verdes: Propostas e realizações”, PhD dissertation, EPUSP, São Paulo,

Gongora-Rubio M.R., Solá-Laguna L.M., Smith M. & Santiago Aviles J. J., 1999, “Integrated LTCC coils for multiple applications in meso-electro-mechanical systems”, Proceedings of International Mechanical Engineering Congress, Symposium on MEMS, Nashville, TN, p-189-194.

Gongora-Rubio M.R., Solá-Laguna L.M., Smith M. & Santiago Aviles J. J., 1999, “A meso-scale electromagnetically actuated normally closed valve realized on LTCC tapes”, Proceedings of SPIE, Conference on Micro-fluidic devices and systems II, Santa Clara, CA, SPIE Vol 3877, p-230-239.

Gravesen P et al., 1993 “Micro-fluidics”, J. of Micro-mechanics and Micro-engineering, Vol 3., p.168-182.

Harley J. C., Huang Y., Bau H., Zemel J., 1995, “Gas flow in micro-channels”, J. of Fluid Mechanics, v.284, p-257-274

Kawakita K., 1999, “Estudo sobre escoamentos críticos em microorifícios e capilares” PhD dissertation, EPUSP, São Paulo,

Moon K. et al, 1998. “The fabrication of Flow conduits in ceramic tapes and the measurement of fluid flow through this conduits”. ASME, International Engineering Congress, Anaheim, CA. Nov 15-20.

National Semiconductor, 1999, “ Design Rules for Physical Lay-out of LTCC modules”, version 8, 50 pages.

Pereira, M.T. Desenvolvimento de um venturi sônico como padrão para medição de vazão. São Paulo, 1990. 163p. Dissertação de Mestrado – Escola Politécnica, Universidade de São Paulo.

Pfahler, J. N. Liquid transport in micron and sub-micron channels, Ph.D. dissertation, U. of Pennsylvania, 1992.

Ruzicka J. Hansen E.H. 1975, “Flow injection Analysis”, Anal. Chim. Acta, 78, p-145-157.

Shuenemann M., Grosser V., Leutenbauer R., Bauer G., Schaefer W. & Reichl H., 1999, “A highly flexible design and production framework for modularized microelectromechanical systems”, Sensors & Actuators A: Physical, v. 73, p 153-168.

Trimmer W, Jebens R. 1.989, “Actuators for Micro Robots”, MEMS-IEEE Micro Electro Mechanical Systems Workshop, p-1547-1552.

Wagner B. & Benecke W. 1.991, “Microfabricated Actuator with Moving Permanent Magnet”, Proc. MEMS IEEE Micro- Electro Mechanical Systems Workshop, Nara Japan, p. 27-32.

XVI CONGRESSO BRASILEIRO DE ENGENHARIA MECÂNICA
16th BRAZILIAN CONGRESS OF MECHANICAL ENGINEERING

IMPLEMENTATION OF AN OPTICAL INTEGRATED PRESSURE SENSOR BASED ON MACH-ZEHNDER INTERFEROMETER (MZI)

Acácio Luiz Siarkowski
Integrated Systems Laboratory – Polytechnic School – University of São Paulo
Av. Prof. Luciano Gualberto, trav. 3, 158 São Paulo – SP – Brazil
acacio@lsi.usp.br

Nilton Itiro Morimoto
Integrated Systems Laboratory – Polytechnic School – University of São Paulo
Av. Prof. Luciano Gualberto, trav. 3, 158 São Paulo – SP – Brazil
morimoto@lsi.usp.br

Douglas A. Pereira Bulla
Integrated Systems Laboratory – Polytechnic School – University of São Paulo
Av. Prof. Luciano Gualberto, trav. 3, 158 São Paulo – SP – Brazil
bulla@lsi.usp.br

Abstract. *This paper describes the principle of operation, simulation results and fabrication of an integrated optical pressure sensor based on Mach-Zehnder interferometer using a micromachined membrane. The results show the feasibility of implementation of this optical device based on a silicon substrate.*

Keywords*. Sensor micromachining, optical waveguide, pressure sensor, Mach-Zehnder Interferometer.*

1. Introduction

Planar processes are widely used in integrated circuits fabrication technology. Optical sensors can be fabricated using the same technology, which open the possibility to integrate these sensors with electronic circuits in a same substrate or package. Silicon oxide and silicon nitride thin films have suitable optical proprieties for these devices and they are compatible with usual microelectronics processes [1-3]. Optical sensors have the main advantage to be immune to electromagnetic interference. In this paper, we describe the principle of operation of such optical sensor, the design approach used in the project of the optical sensor as well as the fabrication method used to implement the sensor.

2. Principle of Operation

In the MZI, the laser coherent light (Io) is split into two waveguides (arms) by θ angle and, after traveling in these two arms, the light beams are recombined in the coupler. This recombination leads to an interference of the laser beams, because the movement of the membrane (located under the sensor arm) modifies the optical path through the sensor arm. Figure 1 shows a schematic drawing of this sensor device.

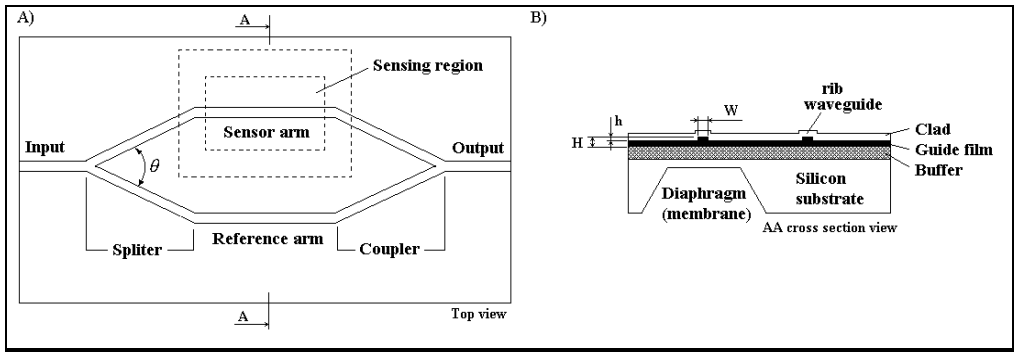

Figure 1. Schematic diagram of an optical pressure sensor based on MZI. A) Top view B) AA cross section view, where W_core is the rib-waveguide width, H_core is the guide film thickness, and h_core is the partial etching step.

The output intensity (I) is a function of the phase difference ($\Delta\varphi$), induced on the sensor arm during the membrane deformation under pressure. The phase difference $\Delta\varphi$ is mainly influenced by two effects [7]:

a) increase in optical pathlength;
b) elasto-optic effect.

If a phase difference is introduced between the light guided into the two arms, the output can be expressed by [6]:

$$I=Io/2(1+\cos\Delta\varphi)$$

3. Waveguide Structure

The waveguide structure was defined in previous works [1,2], in which we developed and characterized the silicon oxide and silicon nitride films structure deposited on a silicon substrate to obtain optical waveguides. These waveguides showed good optical characteristics, a high confinement and low loss. The losses during the propagation were lower than 1dB/cm and the main source of optical attenuation was the light scattering due the roughness on the films interfaces. Figure 2 shows the waveguide structure designed by Bulla [2]. Three layers compose the waveguide structure. The first layer (buffer) is a thick thermal SiO_2 layer with a refractive index of 1.46 and it is used to isolate the dielectric optical medium (waveguide core) from the substrate [7,8] (when red laser is used as light source).

The waveguide film core is a Si_3N_4 layer, with a refractive index of 2.02, deposited by LPCVD (Low Pressure Chemical Vapor Deposition). The horizontal beam confinement can be obtained by etching partially the top of the waveguide film core (h_core) in the areas out of the waveguides. This procedure promotes the decrease of the effective a refractive index in these areas. This type of structure is called by rib-waveguide. The covering film is a SiO_2 layer, with a refractive index of 1.44, deposited by PECVD (Plasma Enhanced Chemical Vapor Deposition).

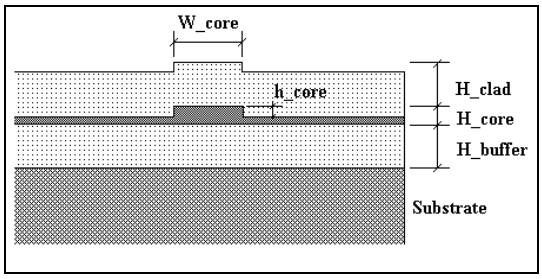

Figure 2: Schematic of a $Si/SiO_2/Si_3N_4/SiO_2$ rib-waveguide.

4. Simulation of the waveguides

We simulated the rib-waveguides and the MZIs using an integrated optic simulation software [6] to determinate the appropriate thickness of the layers (SiO_2 buffer and Si_3N_4 waveguide core layers) and the depth of etching that allow single mode propagation for a laser wavelength of 632.8nm.

We obtained the following results:

- thickness of the SiO_2 buffer layer - 1 μm;
- thickness of the Si_3N_4 layer – 200 nm;
- etching depth of the Si_3N_4 layer – 1 nm;
- thickness of the passivation SiO_2 layer – 200 nm;
- waveguide width - 4 μm.

The TE0 mode (transversal electric field) is showed in the figure 3.

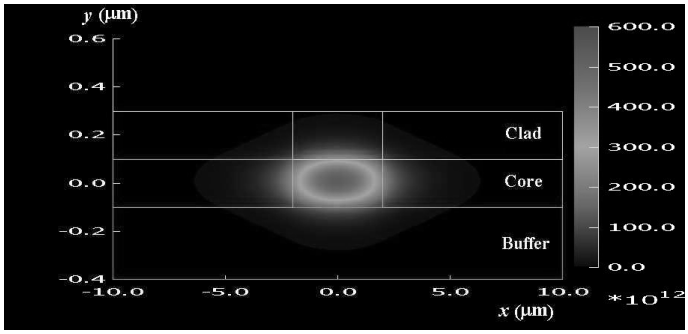

Figure 3. Simulation of electrical field (V/m) confinement in a single-mode rib-waveguide / H_clad=200nm, W_core=4μm, H_core=200nm, h_core=1nm and H_buffer=1μm.

The simulation software can also determines the light scattering in function of the branching angle (θ) in the MZI structure and we found the lowest light attenuation around $\theta = 1^o$.

4. Experiment

A (100) silicon wafer was cleaned (standard RCA) and thermally oxidized at 1150ºC, giving a thick SiO_2 layer (H_buffer). After that, it was deposited a Si_3N_4 guiding layer (H_core) on the both sides of the wafer using LPCVD at 800ºC. The waveguides path was defined on Si_3N_4 guiding layer using photolithographical definition aligned with the primary flat and a BOE (Buffered Oxide Etchant) wet etching. The clad film is a SiO_2 layer (H_clad) deposited by PECVD.

In order to fabricate a thin membrane, various windows aligned with the waveguides were opened up in the Si_3N_4 and SiO_2 layers on the backside of the substrate using a plasma etching and BOE wet etching. The membrane was placed underneath the measurement arm of the interferometer and it was generated by anisotropic KOH etching (27% solution at 85ºC results in an etch rate of 1.2μm/min). So that, a 30μm thick membrane could be produced from a wafer with a nominal thickness of 320μm. From geometrical and mechanical considerations linked to optimization of induced effects, the ration between the length "a" and the width "b" of the membrane must be b/a=2 [2]. The thermal oxide and the Si_3N_4 layers worked as an etch-mask whose etch rate compared to silicon is 1:300 and the topside was protected using the experimental apparatus showed in the Figure 4.

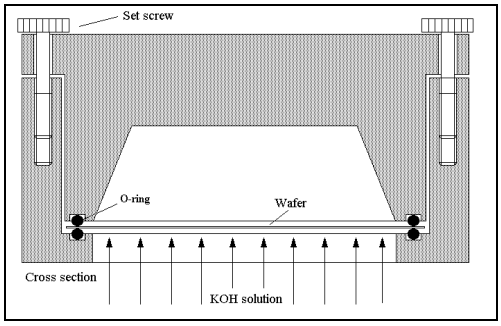

Figure 4. Experimental apparatus used in the KOH etching.

The films, waveguides and the membrane structure can be characterized by RBS, FTIR, SEM, AFM, ellipsometry, stress measurement, number and shape of the guided modes and optical attenuation.

5. Results and conclusions

We have demonstrated the fabrication feasibility to an optical pressure sensor, based in the IMZ structure, using MOS thin films compatible processes.

The Si/SiO2/Si3N4/SiO2 rib-waveguides obtained presented good optical characteristics and a high confinement. The loss during the propagation was lower than 1dB/cm, where the main source of optical attenuation was the scattering on the interfaces of the structures, therefore the roughness in the interfaces must be smallest.

The thin film structure has the following dimensions for mono mode propagation in the waveguide: thickness of the silicon oxide buffer layer of 1 μm, thickness of the silicon nitride layer of 200 nm, etching depth of the silicon nitride layer of 1 nm, thickness of the passivation silicon oxide layer of 200 nm, wide of waveguide of 4 μm, and branching angle $\theta = 1^o$.

The construction of a system based on the use of this device in a coherence modulation scheme is under progress, and the final tests of the optical pressure sensor will be performed soon.

6. Acknowledgements

Financial support from FAPESP, FINEP, CNPq is gratefully acknowledged. In addition, the authors want to thank L. S. Zambom for the thermal oxidation and silicon nitride deposition processes.

7. References

[1] Bulla, D. A. P.; Morimoto, N.I.; "Deposition of thick TEOS PECVD silicon oxide layer for integrates optical waveguide applications", Thin Solid Films, v.334. n.1-2, p.60-64, 1998.

[2] Bulla, D. A. P., et al; "Design and Fabrication of SiO_2/Si_3N_4 CVD Optical Waveguides", Proc. 1999 SNMO/IEEE International Microwave and Optoelectronic Conference, Rio de Janeiro, 1999

[3] Porte, H.; Gorel, V.; Kiryenko, S.; Goedgebuer, J. P.; Daniau, W.; Blind, P; "Imbalanced Mach-Zehnder Interferometer Integrated in Micromachine Silicon Substrate for Pressure Sensor", J. Ligthwave Technol., v. 17, n. 2, p. 229-233, 1999

[4] Najafi, S.I.; "Introduction to Glass Integrated Optics", Boston, Artech House, 1992

[5] Wu, M. J.; Tabib-Azar, M.; “Theorical Analysis of Deformed Optical Waveguides Used in Pressure and Displacement Sensors”, Society of Photo-Optical Instrumentation Engineers, Opt. Eng. 35 (3), p. 870-881, March 1996
[6] BBV Software BV, Professional Solutions for Integrated Optics, 1999
[7] H.P.Zappe, Introduction to Semiconductor Integrated Optics, Artch House, Boston, 1995.
[8] Stutius, W.; Streifer, W.; Appl. Opt., 16 (1977) 3218.

XVI CONGRESSO BRASILEIRO DE ENGENHARIA MECÂNICA
16th BRAZILIAN CONGRESS OF MECHANICAL ENGINEERING

Micro Trocadores de Calor de Ultraprecisão para Satélites

Rodrigo Lima Stoeterau, Dr.-Eng.
Federal University of Santa Catarina
Campus Universitário – Trindade
CxP – 476 EMC 88.010-970 – Florianópolis – SC – Brazil
jgdst@emc.ufsc.br

Marcia B. H. Mantelli, PhD.
Federal University of Santa Catarina
Campus Universitário – Trindade
CxP – 476 EMC 88.010-970 – Florianópolis – SC – Brazil
marcia@emc.ufsc.br

Walter Lindolfo Weingaertner, Prof. Dr.-Ing.
Federal University of Santa Catarina
Campus Universitário – Trindade
CxP – 476 EMC 88.010-970 – Florianópolis – SC – Brazil
wlw@emc.ufsc.br

Resumo. A troca de calor em componentes eletrônicos e mecânicos operando em ambiente de espacial é um dos grandes desafios enfrentados por muitas equipes de projeto de satélite, assim como outras equipes de pesquisadores. Uma das possíveis soluções pode ser através da otimização das superfícies de troca de calor, atarvés da utilização de superfícies com rugosidade nanométrica. Este tipo de superfície pode ser obtido por meio da técnica de usinagem de ultrprecisão com ferramenta de gume único de diamante. Este trabalho refere-se ao desenvolvimento de micro trocadores de calor para aplicações espaciais, fabricados por meio desta tecnologia de usinagem, abordando aspectos dos problemas de projeto e fabricação.

Palavras chave. *Trocadores de calor, usinagem de ultraprecisão, componentes para satélites.*

1. Introdução

A excessiva geração de calor tem sido um dos grandes limitantes no aumento do desempenho de componentes eletrônicos, especialmente microprocessadores. Independentemente do tipo de satélite, geo-estacionário, de movimento orbital fixo ou variável, esses estão submetidos a condições térmicas que variam do extremo calor, quando suas superfícies estão expostas a radiação solar, ao frio extremo. Esta condição de operação forma um interessante problema de engenharia termodinâmica. Em condições de microgravidade ou vácuo a troca de calor em componentes eletrônicos tem sido um dos grandes desafios enfrentados por pesquisadores, cientistas e engenheiros. Muitos estudos tem sido feitos no sentido de se desenvolver formas mais eficientes para promover a retirada do calor gerado em circuitos eletrônicos operando em ambiente espacial.

1. Objetivos

Entre os diversos requisitos de projeto presentes no desenvolvimento de satélites, alguns apresentam importância ímpar, tais como: massa e confiabilidade, principalmente de componentes eletro-eletrônicos. Ambos os requisitos apresentam uma relação direta pois a confiabilidade destes sistemas é afetada pelo aumento excessivo da temperatura, e o uso de sistemas de troca de calor convencionais ou resfriamento forçado em muitos casos implica em aumento de massa.

Várias são as formas de promover a retirada de calor em sistemas eletrônicos ou mecânicos, sendo que o uso de componentes aletados umas das soluções mais difundidas. Em ambiente aspecial o uso desses componentes pode ser afetado pela inexistência de um meio (vácuo) para propagação de calor por condução e convecção, ou pela existência de um meio confinado, onde a presença de uma fonte contínua de geração de calor pode levar a mudanças operacionais internas à estrutura do satélite. Em ambiente de vácuo um aumento na eficiência de trocadores de calor pode ser feita com a melhoria da qualidade superficial das aletas, priorizando a torca de calor por radiação.

O desenvolvimento de micro trocadores de calor pode ser uma solução capaz de atender a ambos os requisitos de peso e eficiência na remoção de calor desses componentes.

1. Materiais e Métodos

O desenvolvimento dos micro trocadores de calor não fez considerações do ponto de vista termodinâmico, ou de transferência de calor, tendo sido projetados de empírica, pois o objetivo básico foi o de demonstrar a viabilidade tecnológica de fabricação deste tipo de componente miniaturizado. Neste sentido foi projetado um trocador de calor básico, cujas as dimensões foram definidas arbitrariamente, conforme apresentadas na figura 1, sendo o comprimento

limitado a um valor máximo de 90 mm. Havendo a necessidade de se testar componentes com comprimento menores do que 90 mm estes podem ser obtidos pelo corte de uma peça padrão. Para dimensões diferentes das originalmente arbitradas, existe a necessidade de se projetar novos dispositivos, ou selecionar novas ferramentas.

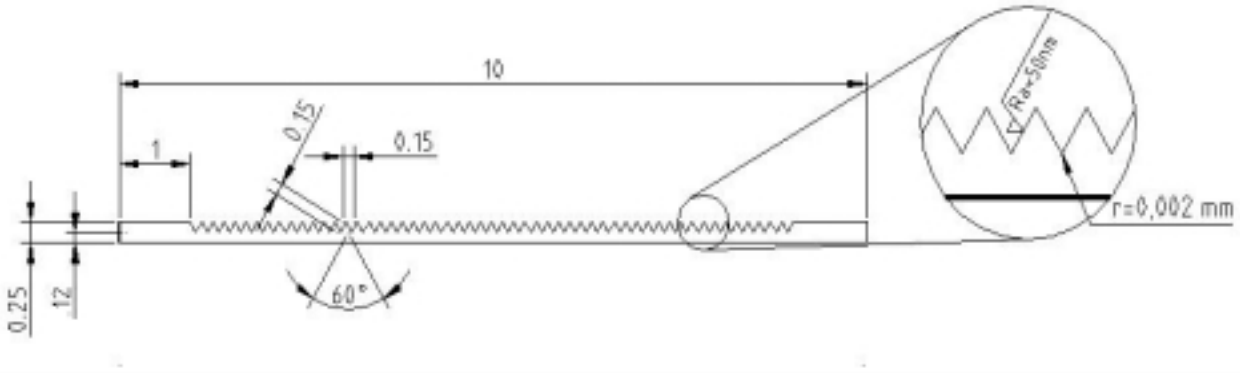

Figura 1. Dimensões gerais para o micro trocador básico (dimensões em mm).

Devido a impossibilidade de se obter cantos vivos no fundo das ranhuras em -V-, foi especificado um raio canto de 2 ?m na interseção das superfícies das aletas. O micro trocador básico foi projetado para ser fabricado em cobre, dada a sua elevada condutividade térmica desse material, além das características de usinabilidade e compatibilidade química deste material com o diamante.

I1 Fabricação

A usinagem de ultraprecisão com ferramenta de diamante de gume único, pode ser definida como sendo o estado da arte da tecnologia de fabricação com ferramentas de geometria definida. Os estudos iniciais surgiram em meados dos anos 60, do século XX, com os trabalhos pioneiros de Bryan no Lawrence Livermore National Laboratory nos Estados unidos, essa tecnologia surgiu como uma alternativa a fabricação tradicional de elementos ópticos. Com o aumento da demanda por produtos de alta tecnologia nas áreas de energia, defesa, espacial, computação, eletrônica e outras, a usinagem de ultraprecisão com ferramentas de diamantes monocristalinos permitiu que certos elementos pudessem ser produzidos de forma rápida, com menores custos e elevada qualidade (Ikawa, 1991; Koenig, 1991; Patterson, 1986; Saito, 1975; Schroeter, 1997; Tanigushi, 1983-1994).

Desta forma usinagem de ultraprecisão com ferramentas de diamantes monocristalinos pode ser definida como a técnica que permite fabricar produtos com elevadas tolerâncias dimensionais e geométricas, geralmente no campo do submicrométrico, independente de tamanho e forma, com ou sem qualidade superficial, que geralmente chega na ordem de alguns nanometros R_a (Saito,1975; Brehm et all, 1979; Patterson, 1986; Ikawa, 1991; Koenig, 1991; Schroeter, 1997).

I1 A Máquina.

A máquinas-ferramenta para usinagem de ultraprecisão utilizada no desenvolvimento dos micro trocadores de calor, está baseada na estrutura de um torno de ultraprecisão Moore-Ex-Cell-O, desenvolvido em meados dos anos 70, do século XX. Este torno foi *retrofitado* através da instalação de uma nova árvore aerostática, essa encontra-se integrada a uma guia linear também aerostática, acionada por motor linear. O torno original também recebeu novos motores de acionamento e eletrônica de controle. Confrontando os requisitos de projeto espeficados para os micro trocadores de calor, com as características de rigidez, suavidade de movimento e exatidão de posicinamentos do obtidos no torno retrofitado, levou ao desenvolvimento da infra-estrutura necessária, e ao estabelecimetos dos procedimentos para a fabricação. A figura 2 apresenta a visão geral do torno retrofitado Moore-Ex-Cell-O, indicando alguns de seus principais componentes.

O torno de ultraprecisão utilizado apresenta as seguintes características técnicas:

- curso na direção Z principal: 400 mm;
- exatidão de posicionamento teórica na direção Z principal: 10 nm;
- curso na direções Z secundária: 60 mm;
- exatidão de posicionamento teórica na direções Z secundária: 100 nm;
- curso na direção X: 650 mm;
- exatidão de posicionamento teórica na direção X: 10 nm;
- velocidades de avanço controladas até 0,01 mm/min.;
- velocidades de rotação da árvore variando de 1.800 até 3.500 rpm.

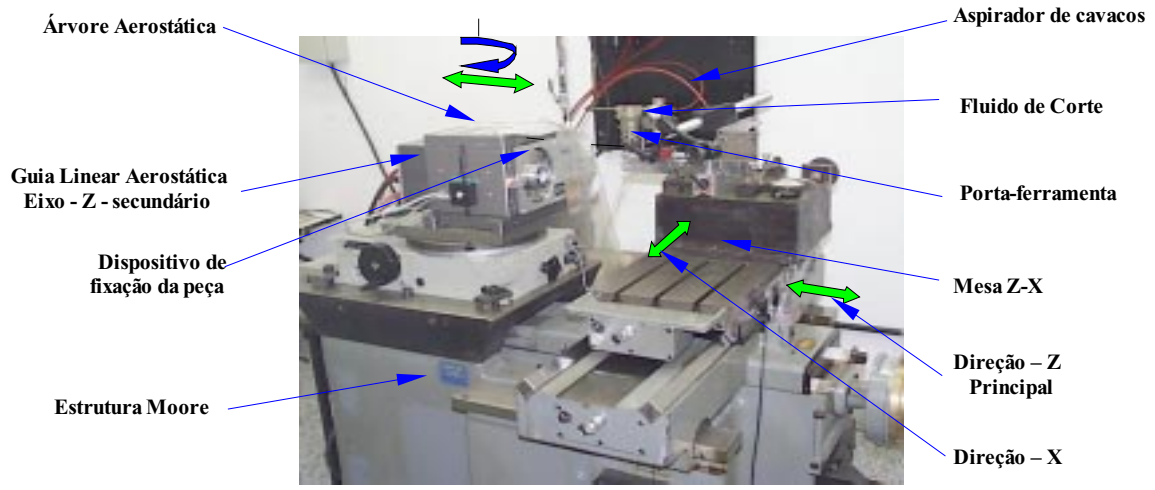

Figure 2. Torno de ultraprecisão retrofitado Moore-Ex-Cell-O.

A integração dos sistemas foi realizada por meio de um CNC de arquitetura aberta. O torno opera em ambiente controlado (20 ?1 ^{o}C), sendo que a estrutura da máquina está montada sobre um sistema de isolamento passivo de vibrações.

I1 O Processo de Fabricação

A escolha do cobre como material da peça deu-se em função de suas características de condutividade térmica e facilidade de usinagem, como forma de prevenir danos ao gume da ferramenta, principalmente lascamentos devido a inclusões de impurezas ou empastamento na superfície de saída, foi selecionado cobre com 99,9991 % de pureza, sem oxigênio (OFHC) e laminado a frio, fornecido na forma de chapas quadradas com 100 mm de lados e 1 mm de espessura.

Um dos problemas encontrados foi o de como manter a peça tracionada o suficiente, pois um tracionamento excessivo ou a falta desse podem levar a variações na profundidade das ranhuras. A figura 3 apresenta uma visão geral do dispositivo de fixação da peça, juntamente com os erros consequentes da falta de um tracionamento correto. Todo o conjunto foi balanceado após a montagem para evitar dados aos mancais aerostáticos da árvore, ou imperfeições nas superfícies da ranhura decorrentes de vibrações.

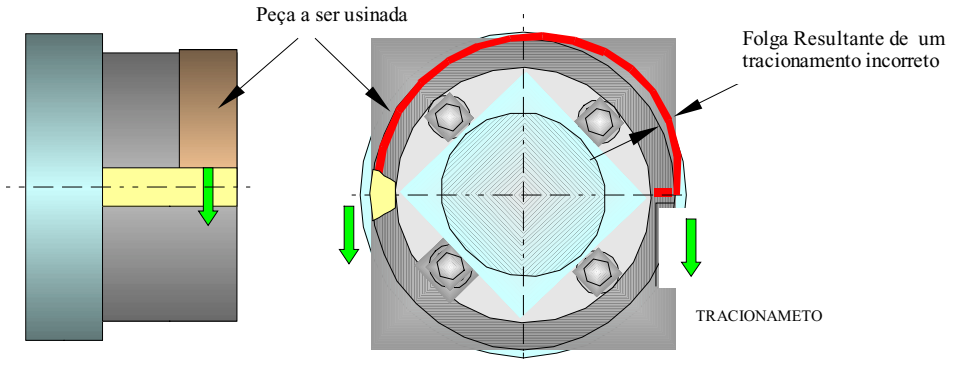

Figure 3. Dispositivo de fixação.

Os parâmetros de usinagem utilizados foram 1800 rpm, avanço transversal de 0,01 mm/min, como fluido de corte foi utilizado uma mistura de ar/álcool. Os cavacos apresentam seção micrométrica e têndem a retornar e aderir na superfície recém usinada da peça, vindo a produzir riscos ou danos na mesma. Desta forma o uso de fluido de corte teve como objetivo principal facilitar o escoamento dos cavacos na superfície de saída., evitando que esses venham a empastar ou retornar sobre a ferramenta. A figura 4 apresenta uma visão geral do microtrocador de calor durante a usinagem.

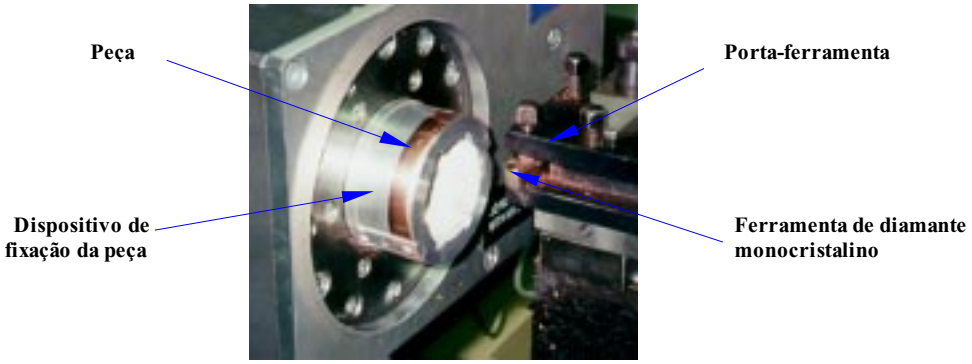

Figura 4. Micro trocador de calor durante a usinagem.

1. Resultados

A avaliação das ranhuras após a usinagem, figura 5, revelou que as mesmas ficaram livres de rebarba, e com superfícies qualidade superficial espelhada, o que caracteriza um valor de R_a inferior 50 nm. Sendo a rugosidade média R_a definida como a média aritmética dos valores absolutos dos afastamentos h_i do perfil médio. Em alguns casos foram observadas superfícies opacas nos vértices das ranhuras, o que sugere que nesses casos as condições de remoção dos micro cavacos foi deficitária. O escoamento deficitário dos micro cavacos na superfície de saída pode levar ao empastamento nesta região, o que pode ter propiciado arranque de material ou adesão nas superfícies de incidência. Este problema posteriormente foi eliminado com o reposicionamento e aumento da presão nos injetores de fluido de corte.

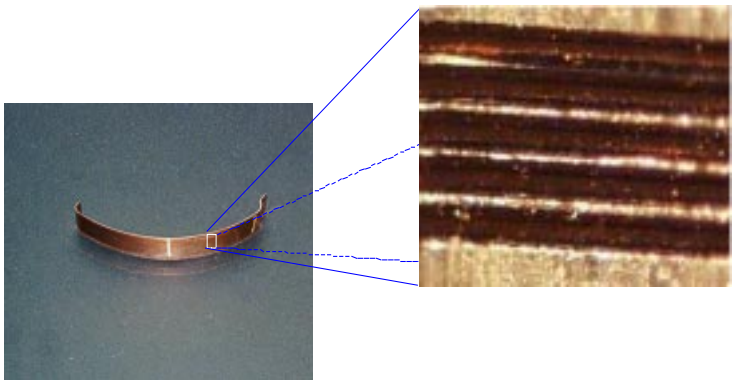

Figura 5. Visão das ranhuras após a usinagem do micro trocador de calor.

1. Conclusões

Se comparado com os trocadores de calor convencionais, os micro trocadores de calor apresentarem pouca eficiência térmica, porém com a vantagem de apresentarem pequenas dimensões e consequentemente pouca massa. A eficiência destes tipo componente pode ser melhorada em muito pela adoção da tecnologia de *heat pipe,* ou seja, a adoção confinada de fluido de baixo ponto de ebulição em meio poroso. Contudo o uso da tecnologia de usinagem de ultraprecisão com ferramenta de geometria definida comprovou ter viabilidade para a produção desses micro componentes. O desenvolvimento de micro trocadores de calor pode ser considerada como uma primeira etapa no desenvolvimento da tecnologia de fabricação para micro *heat pipes.*

1. Agradecimentos

Os autores gostariam de agradecer aos graduandos Hugo M. Perine, Marcus R. Coelho, Victor E. Gomes and Giovani B. Fabris por sua dedicação e empenho neste trabalho.

1. Referencias

Brehm, R.; Dun, K. van; Teunissen, J. C. G.; Haisma, J., 1979, "Transparent Single Point Turning of Optical Glass", Precision Engineering,

Ikawa, N.; et all., 1991, “Ultraprecision metal cutting - the past, the present and the future”, Annal of CIRP, vol. 40.

Koenig, W.; et all., 1991, “Diamond machining technology.”, Tutorial of 6° IPES/UME 2.

Patterson, S. R., 1986, “Development of precision turning capabilities at Lawrence Livermore national laboratory.”
Schroeter, R. B., 1997, “Usinagem de ultraprecisão de elementos ópticos transmissivos no espectro infravermelho.” PhD tesis – Universidade Federal de Santa Catarina.
Saito, T. T., 1975, “Machining of optics: an introduction”, Applied optics, vol. 14, number 8, pp. 1773.
Tanigushi, N., 1983, "Current Status in, and Future Trends of, Ultraprecision Machining and Ultra-fine Materials" Processing. CIRP. Anais. V. 32, fev. 1983.
Tanigushi, N., 1994, "The State of the Art of Nanotechnology of Ultraprecision and Ultra-fine Products". Precision Engineering, v. 16, n. 1, jan. 1994.

Ultraprecision Micro Parts for Satellites Heat Exchanges

Abstract. Heat exchanges in electronics and mechanical components operating in vacuum environment, is a great challenger faced by many satellites developments team, as other researchers groups. One solution is optimize the exchange surface by means of a nanometric roughness, provide by ultraprecision machining with single point diamond tool. This paper concern about the development of small ultraprecision heat exchange, from the design point of view until manufacturing problems.

Keywords. *heat exchange, ultraprecision machining, satellites parts*

XVI CONGRESSO BRASILEIRO DE ENGENHARIA MECÂNICA
16th BRAZILIAN CONGRESS OF MECHANICAL ENGINEERING

FABRICATION OF NEEDLE SHAPE MICROSTRUCTURES FOR CHEMICAL SENSOR

Marcelo Bariatto Andrade Fontes
Laboratório de Sistemas Integráveis Escola Politécnica da Universidade de São Paulo, São Paulo - S.P. - Brazil - C.E.P 05508-900 - Fax: +551138185665
e-mail: bariatto@lsi.usp.br

Roberto Eduardo Bruzetti Leminski
Laboratório de Sistemas Integráveis Escola Politécnica da Universidade de São Paulo, São Paulo - S.P. - Brazil - C.E.P 05508-900 - Fax: +551138185665
e-mail: leminski@lsi.usp.br

Rogério Furlan
Laboratório de Sistemas Integráveis Escola Politécnica da Universidade de São Paulo, São Paulo - S.P. - Brazil - C.E.P 05508-900 - Fax: +551138185665
e-mail: furlan@lsi.usp.br

Jorge Juan Santiago-Avilés
Center for Sensor Technologies – Electrical Engineering Dept. of University of Pennsylvania - USA
e-mail: santiago@ee.upenn.edu

Abstract. The necessity of in situ measurements of many biologically important chemicals, is a driven force to produce multidetection needle shape microsensors. The fabrication of such structures can be achieved by using different techniques. Glass micropipette or metal microfiber – electrochemically or flame sharpened – are considered standard techniques. On the other hand this approach presents drawbacks producing usually just a single electrode, with lack of reproducibility. Recently, the development of the silicon micromachining technology opened a new horizon on the fabrication of microstructures, providing high scale, reproducible and low cost per unit. In this way, we have explored etching stop and plasma etching techniques to produce needle shape microstructures as a mechanical support for electrochemical sensors. Optical and scanning electron microscopy (SEM) were used to characterize the microstructure morphology. Secondary Ion Mass Spectroscopy (SIMS) was used to quantify the boron concentration in the diffusion process and numerical simulator (Ansys®) was used to estimate the mechanical strength of the microprobes. It is also presented an electrochemical characterization of the fabricated sensor. Typical dimensions of the microstructures varying from 90 μm to 340 μm at the silicon tip end (depending on the electrodes number) and thicknesses from 15 μm to 60 μm were achieved.

Keywords: silicon micromachining, chemical microsensor, microstructure.

1. Introduction

Chemical microsensors have had a tremendous development in many different applications (Najafi, 1985) including pH determination, gas sensing and analysis of complex biological molecules. Miniaturized needle-shape probes have been used in many biological applications that require single cell detection, such as: neural activities, intracellular recording and ionic distribution (Prohaska, 1986). Our main application is related with the nitric oxide (NO) detection (Malinsky, 1992 and Fontes 1995-1999).

The NO molecule have attracted attention in the recent years because the many interactions in the human body such as: it helps to maintain blood pressure by dilating blood vessels, it helps to kill foreign invaders in the immune response, is a major biochemical mediator of penile erection and is probably a major biochemical component of long-term memory (Acher, 1993). The detection of the activity of such molecules in small concentrations is vital in many studies *in vitro,* and *in vivo* as well as in diagnostic and therapy.

The fabrication of the microprobes can be achieved by using different kinds of techniques, Fig. 1, such as: glass micropipette, metal microfiber – both usually producing just a single electrode - or silicon micromachining (Cobbolt, 1974 and Geddes, 1989).

The fabrication of the probe in a silicon substrate by using boron etch stop technique is based on the property of the silicon to be anisotropically etched in alkaline solutions (Madou,1997), like KOH, where the (100) crystallographic plane is preferably corroded. Other silicon property is related to the decrease on its etching rate, in the same alkaline solutions, by high ($> 10^{19}$ atoms/cm^3) dopant concentrations usually (Boron), where the structure shape is defined by a deep diffusion profile. We have used silicon dioxide patterned with the probe shapes as a mask in the diffusion process, see Fig. 2(a).

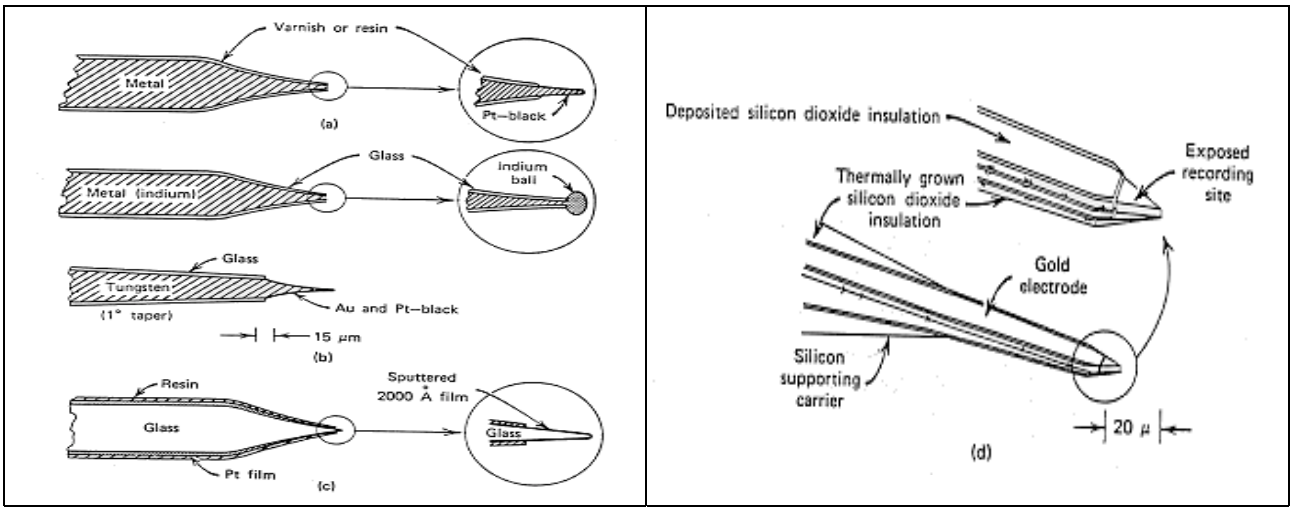

Fig. 1. Example of microfabricated electrodes: a) resin-insulated etched metal wire electrode; b) sharpened metal-filled glass micropipette; c) metal sputtered and resin insulated glass electrode and d) silicon micromachining and IC technologies.

On the other hand, silicon plasma etching can be used to produce probes by masking the silicon with a metallic mask, patterned with the probe shapes, as described in the Fig. 2(b). This technique has advantages over the previous one such as (Madou,1997 and Fontes, 1999): relatively low temperature process (does not reacquire diffusion step), better shape definition (without lateral diffusion) and thickness control, quick process (without long diffusion times) and low silicon crystalline orientation dependence.

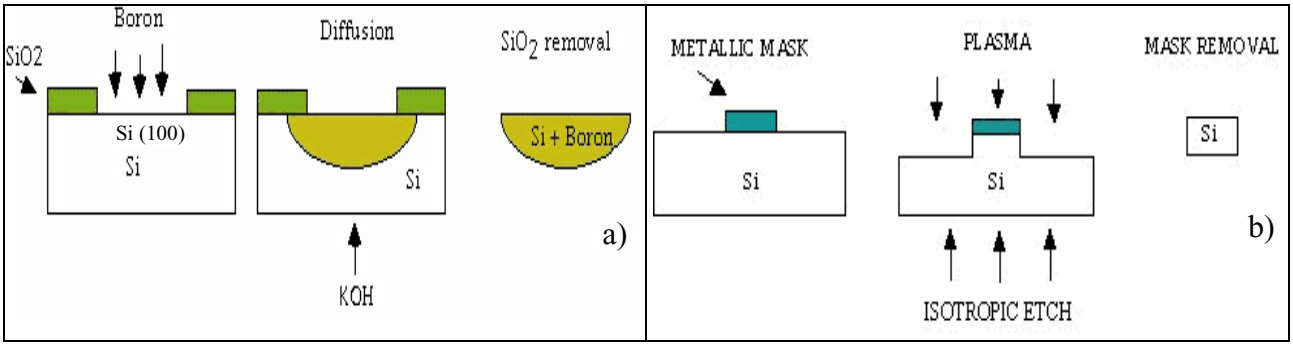

Figure 2. Schematic sequence of two different ways of producing micromachined probes: a) using boron etch stop and b) plasma etching techniques.

In this paper, we explore several silicon probe shapes to define our microstructure used as a mechanical support for electrochemical sensors, as described in the next section.

2. Sensor design and fabrication

The micromachined multidetection electrochemical sensor was designed to have a number of sensing areas varying from 2 to 10. This has a direct influence on the sensor dimensions as described in Fig. 3. The sensor is composed of a silver/silver chloride reference electrode, a platinum auxiliary electrode – located at the backside of the structure - and several gold detection microelectrodes (10 μm x 10 μm). Typical dimensions of the sensor are: a length of 10 mm, a width of 3 mm at the contact pads area and a tip width varying from 90 μm to 340 μm. The gold interconnection lines have a width of 20 μm. Silicon dioxide was used to insulate the electrodes from the silicon substrate and silicon nitride was used as a passivation material and insulator for the back electrode.

A concern on the fabrication of such thin structures is related to the stress induced by the several films used. A proper combination (thickness ratio of 4:1) of thermal silicon dioxide and low pressure chemical vapor deposition (LPCVD) silicon nitride films on silicon tips have been used successfully in literature (Najafi, 1985). In our case, a sputtered deposited nitride was used, due to presence of the gold. In this case, an uncompensated stress was observed, as discussed in the next section.

In order to produce such geometry on the silicon substrate, we have used two different micromaching techniques: boron etch stop and plasma etching. Previous experiments concerning handling, limited the probe thickness to at least 10μm (Fontes, 1999). Therefore we designed our experiments to achieve high yield with a safe thickness around 15 μm.

For the boron etch stop technique, we used an SOG boron source (Filtronics B-155) applied by spin coating. Typical diffusion process parameters were: 26 hours at 1150°C in conventional furnace and an extra sintering step at 1075°C and 90 minutes, for silicon stress relief (Bruce, 1997).

For the plasma etching we used a reactor that combines inductively coupled plasma (ICP) with reactive ion etching (RIE) (Mansano, 1996-1999). Typical plasma parameters were: gas pressure of 30 mTorr, ICP (30 W) and RIE (100 W) powers, and gas flows of SF_6 (5 sccm) and Ar (15 sccm). The etching rate was 0.35µm/min.

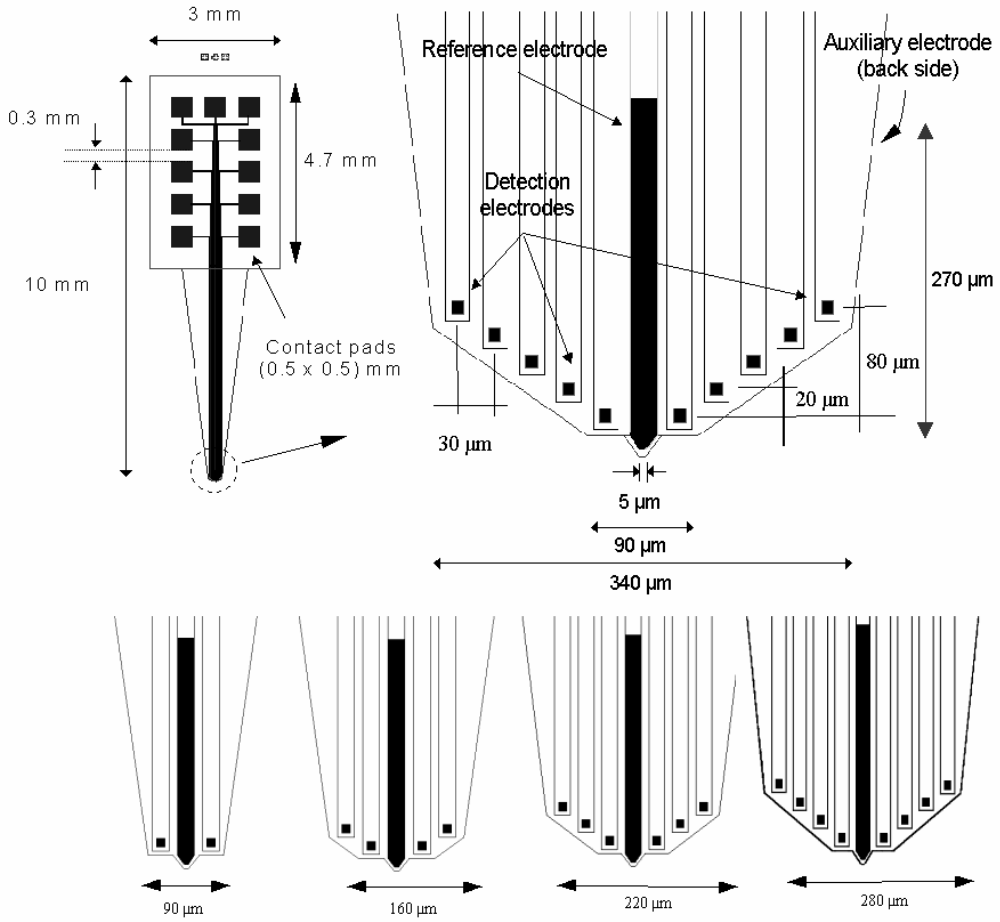

Figure 3. Drawing of the sensor design and dimensions for 2 to 10 sensing areas.

To release the probes from the silicon substrate, KOH etching (40% wt.) was used in both cases. This process was performed at 50 ^{0}C in a rotatory holder with the silicon wafer facing up.

Figure (4) shows schematically the sensor fabrication sequence for both micromachining techniques.

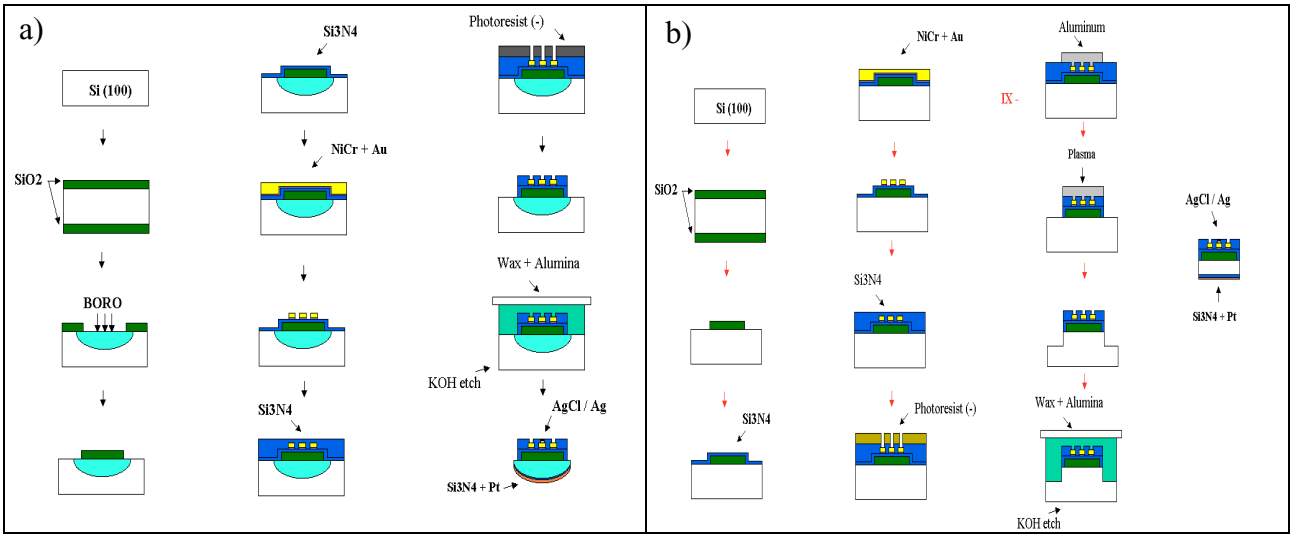

Figure 4. Sensor fabrication sequence for both: a) etch stop and b) plasma etching processing.

The sensors were fabricated using the sequence described below, where (**P**) = plasma processing, (**B**) = boron etch stop and (**C**) = common processes:

- Wet oxidation of 2" silicon wafers (p type, orientation: <100>, resistivity 1 - 10 Ω.cm) to obtain 1.2 μm of SiO_2, previously cleaned (RCA) **(C)**;
- Oxide patterning with probe shape mask (M1) **(C)**;
- Spin coat boron doped SOG and diffusion (**B)**;
- New oxidation and oxide patterning to produce a insulation from the silicon substrate (**B)**;
- Si_3N_4 deposition by sputtering (~300 nm), for stress compensation due to the oxide layer **(C)**;
- NiCr e-gun evaporation (adhesive material) **(C)**;
- Gold film e-gun evaporation (300 nm) **(C)**;
- Gold and NiCr electrode lines, contact pads, reference and detection electrodes areas, patterning with mask (M2) **(C)**;
- Si_3N_4 deposition by sputtering (~300 nm), as a protective layer **(C)**;
- Si_3N_4 plasma etching (CF_4+O_2) to open contacts, detection and reference areas, defined by mask (M3), using a negative photoresist as a etching mask **(C)**;
- Aluminum e-gun evaporation (~1μm) and patterning with the mask (M1) (**P)**;
- Silicon plasma etching (SF_6+Ar) to the desired thickness **(P)**;
- A wax application over the top side of the wafer and attachment to an alumina plate **(C)**;
- KOH etch of the wafer back side, until probe separation **(C)**;
- Si_3N_4 (~300 nm) followed by platinum (~100 nm), on the back side of the probes, both deposited by sputtering. This nitride layer has two objectives: electrical insulation and stress compensation for the top protective layer **(C)**;
- Wiring bonding to a carrier with silver epoxy applied for back contact **(C)**;
- Selective silver electrodeposition and silver chloride formation by chemical reaction, on the reference electrode **(C)**.

After fabrication, the microsensors were characterized by scanning electron microscopy (SEM) and atomic force microscopy (AFM). Secondary Ion Mass Spectroscopy (SIMS) was used to quantify the boron concentration in the etch stop process and numerical simulator (Ansys®) was also used to estimate the mechanical strength of the microstructure.

3. Fabrication results and discussion

Figure (5a) shows SEM images of the fabricated sensor before the substrate removal, where the contact pads, detection, reference and auxiliary electrodes are indicated. Typical AFM results of one microelectrode is shown in Fig. 5(b). Measured surface roughness was around 12.5 nm leading to a slight increase (16 %) on the whole area. This is particularly interesting since the sensor response is directly proportional to the area. Indeed, we are performing experiments by electrodepositing gold produce even higher electrode areas.

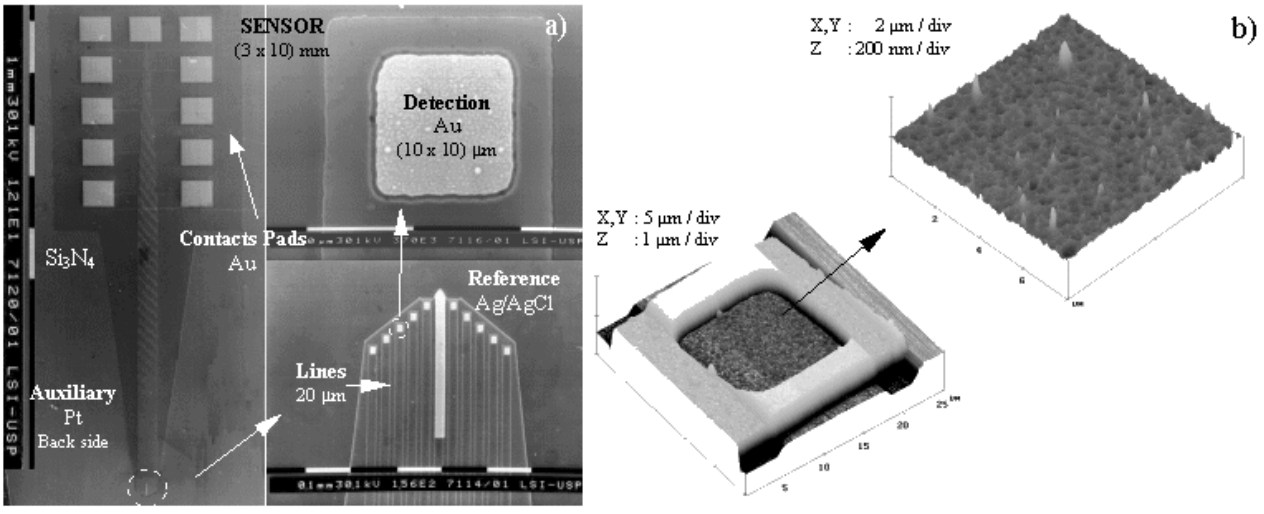

Figure 5. a) SEM images of the sensor front side and details, before the substrate removal, b) AFM image of a microelectrode surface.

SEM images of the silicon microstructures for both micromachining techniques are presented in the Fig. 6. It can be seen that both processes produced flat structures, Fig. 6(a). Clearly the lateral diffusion produced a broadening in the probe tip for the etch stop technique, as shown in Fig. 6(b). On the other hand, probes fabricated by plasma etching technique presented a better shape definition, Fig. 6(c), following the expected geometry due to the anisotropy of the process. Also, some residual silicon, located at the edges, can be observed, as shown in Fig. 6(d). This material is removed by extending the etching in the KOH solution.

SIMS analyses were performed to determine the boron concentration in the obtained tip, which acted as silicon etch stop in the KOH solution. We analyzed both bottom and top tip surfaces. We used a boron implanted (BF_2) silicon wafer, with a known concentration of $1.25x10^{20}$ at./cm^3, as a standard. The obtained boron etch stop concentration of $2.4x10^{19}$ boron at./cm^3 corresponds to a decreasing of the silicon etching rate of approximately 5 times (Madou, 1997).

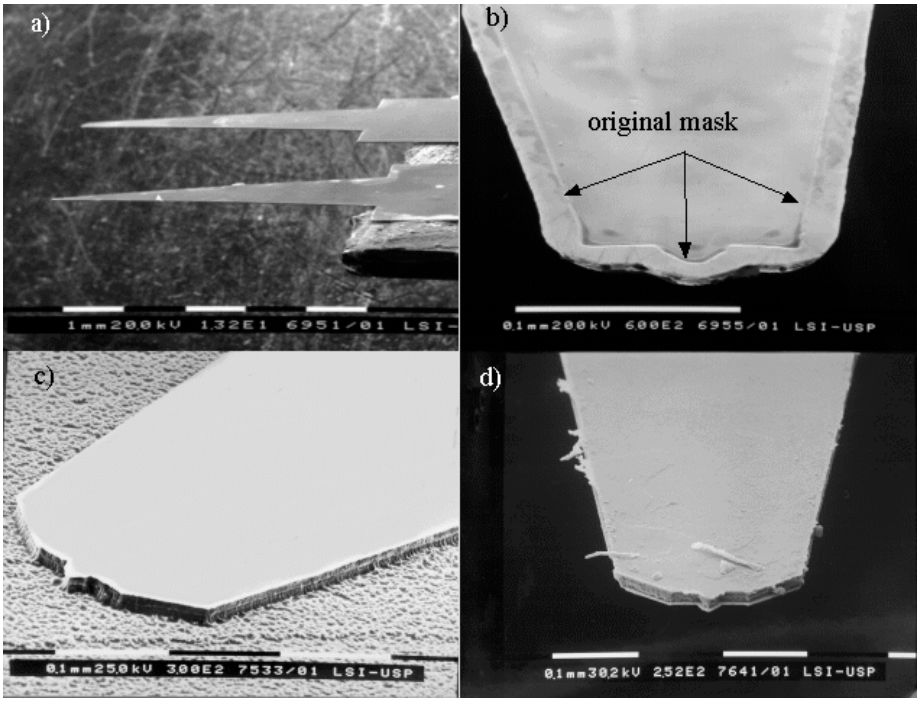

Figure 6. SEM images of micromachined probes (without electrodes), fabricated using boron etch stop (a-b) and plasma etching (c-d) techniques.

After the complete sensor fabrication, a pronounced bending in the probe structure was observed, independently of the fabrication technique used, Fig. 7(a). This mechanical deformation caused a damage in the nitride protective layer and even an interruption in some gold interconnection lines, Fig. 7(b).

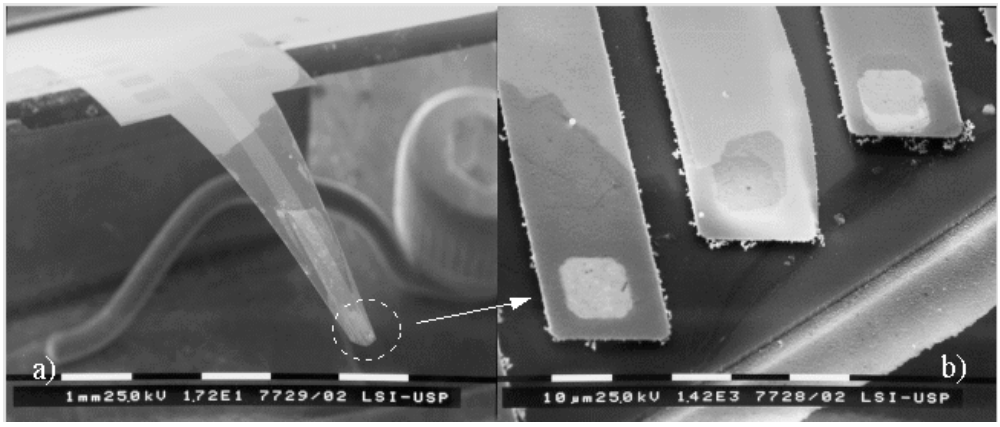

Figure 7. Probe after the KOH etching. The bended structure (a), caused damage in the protective layer (b).

A possible source of this bending is due to an uncompensated stress caused by the mechanical characteristics of the silicon nitride film, which is strongly dependent on the deposition technique (Madou,1997), as shown in table 1. Furthermore, in plasma depositions, the mechanical stress for a nitride film can vary from compressive to tensile as a function of deposition parameters.

Table 1. Mechanic stress data for SiO_2 and Si_3N_4. (C) = compressive, (T) = tensile.

MATERIAL	MECHANICAL STRESS 10^7 (N / m^2)
SiO_2	3 (C)
Si_3N_4	LPCVD : 10 (T)
	PLASMA : 2 (C) – 5 (T)

A way to overcome this problem and promote a higher yield processing was to increase the probe thickness with a compromise between layers integrity and minimum probe thickness.

Simulations performed with the process simulator program Suprem 4®, showed that the boron diffusion time needed to double the probe thickness could take several days, making this technique not useful.

Plasma etching fabrication processing provides a better solution. Just by monitoring the etching time one could easily reach any desirable thickness.

We produced probe thicknesses of 30 µm, 45 µm and 60 µm, checking for covering integrity and structure bending. The results are shown in Fig. 8, where the probes were placed up side down (30 µm probe not shown). It can be easily seen that increasing the probe thickness the bending decreases. Probes with 45 µm thick did not presented any integrity problems, but for the 30 µm thick some problems were found. Therefore we choosed probes of 45 µm as a compromise between a thin and reliable structure.

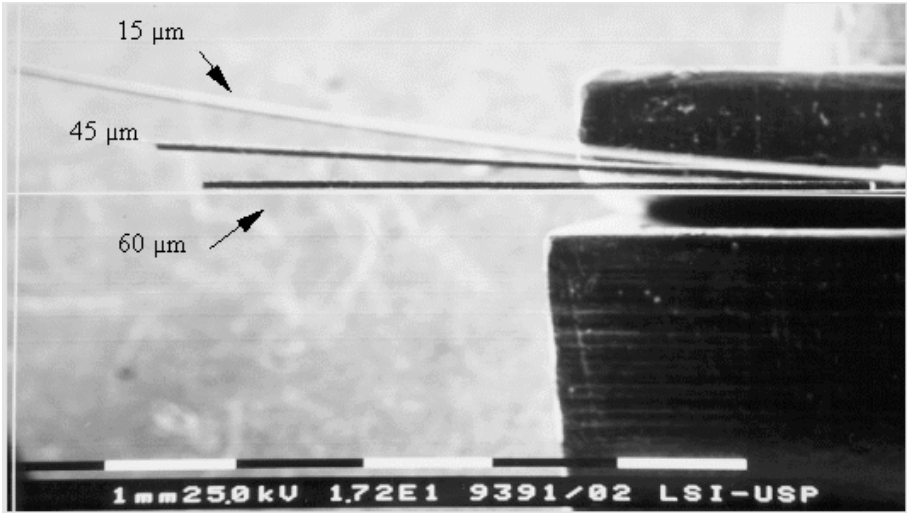

Figure 8. SEM images of the progressive decreasing of the probe bending as its thickness increases.

Figure (9) presents a 45µm thickness probe assembly into its carrier, ready to use. It is also shown in inset a comparison with a American cent coin. The obtained yield at this thickness was around 80%. This promising result effectively shows how powerful the micromaching technique is as a tool to produce multielectrode probes. In the next section we present some results from ANSYS® mechanical simulation of the microstructures.

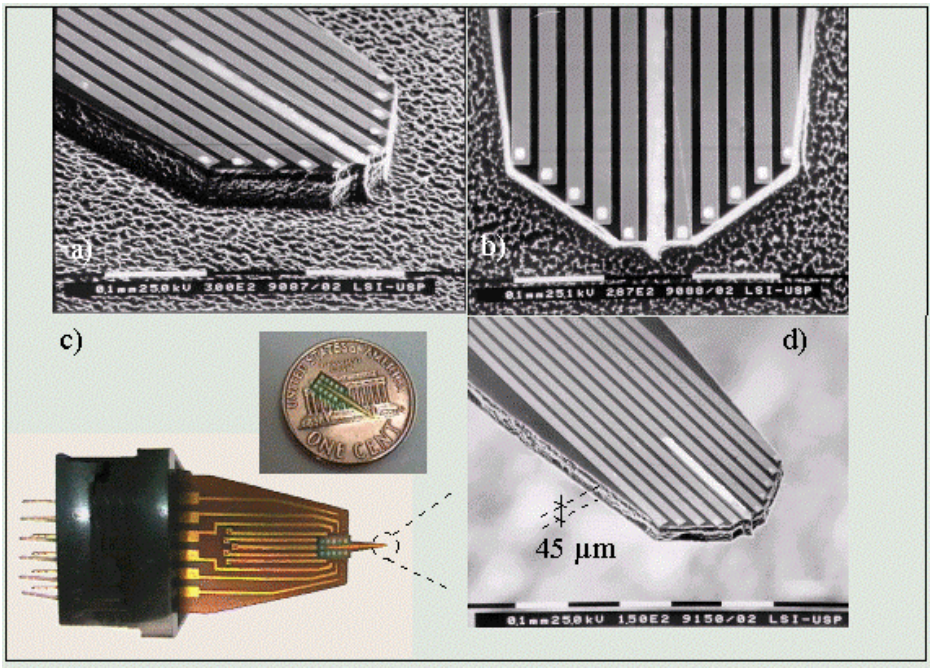

Figure 9. a,b) plasma etched microstructures, c,d) final assembly of a 45µm thick probe. Inset a comparison with one-cent of American dollar.

4. Microstructures simulation

We used the numerical simulator Ansys® (ver. 5.4) to perform an initial study on the mechanical strength of the microstructures which plays an important role on its reliability. For this preliminary study, just plain silicon structures were simulated with thicknesses of 5µm, 10µm, 50µm, 100µm and 500 µm, in a compressive assay. The following assumptions were adopted for the simulations:

- The simulation was performed in the structural mode and used finite element SOLID 73, which is the most indicated for this kind of simulations (Ansys® User's Manual, 1994).
- All microstructures are considered to be made of silicon, without any extra film on it.
- The silicon was considered isotropic, with mechanical characteristics of the crystalline orientation <100>, table 2.
- A load of increasing value was applied to the bottom part of the structures, e.g. on the tip, and the top part was kept fixed.
- Pressure condition instead of a force condition was performed to apply the load, this condition was observed, previously, to results in a more coherent results.
- Devices that presented mechanical stress higher than the silicon rupture stress (table 2) were assumed to be fractured.

Table 2: Silicon bulk mechanical characteristics for <100> orientation (King, 1988)

Mechanical Characteristic	Value
Young's Modulus	165 GPa
Density	2330 kg/m^3
Poisson Ratio	0,222
Rupture Stress	181 MPa

Simulation results showed that for all types of structures and thicknesses, the maximum internal stress occurred at the tip region of the probe. These results were indeed expected since this region presents the lowest cross section (Timoshenko, 1988 and Popov, 1968). An example of the stress distribution for a load of 340 µN is presented in Fig. 10, for a configuration with 2 detection electrodes and 500 µm thick.

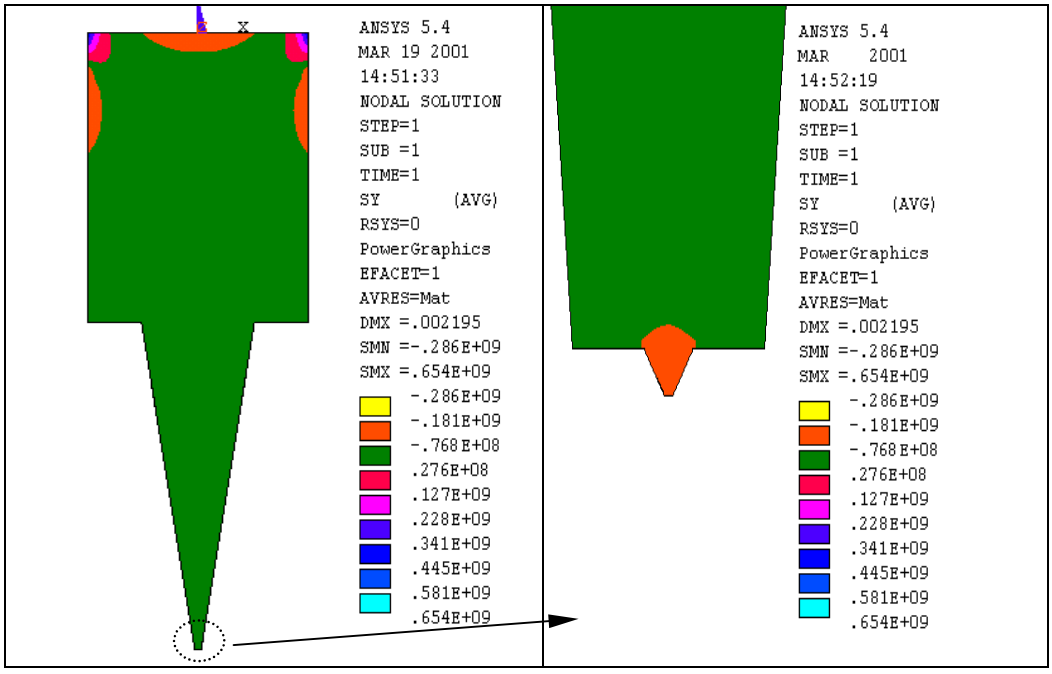

Figure 10. Mechanical stress distribution (N/m^2) for a microstructure with 2 sensing electrodes and 500 µm thick, with applied force of 340 µN.

Results obtained for the maximum load for all structures and thicknesses are presented in table 3. Since the tip part of all microstructures has the same geometry, we observe that regardless the number of sensing electrode, the structures breaks at the tip and for a given thickness, the same maximum load was obtained. Furthermore, the maximum load is linearly proportional to the microstructure thickness, as shown in Fig. 11. This can be explained due to a smaller cross-sectional area; increasing the thickness, the maximum load also increases.

Table 3. Maximum load applied to the microstructure before break for all geometry configurations and several thickness.

	Maximum load (mN)				
	Microstructure thickness				
Number of detection electrodes	5 µm	10 µm	50 µm	100µm	500 µm
2 to 10	3.4	6.8	34	68	340

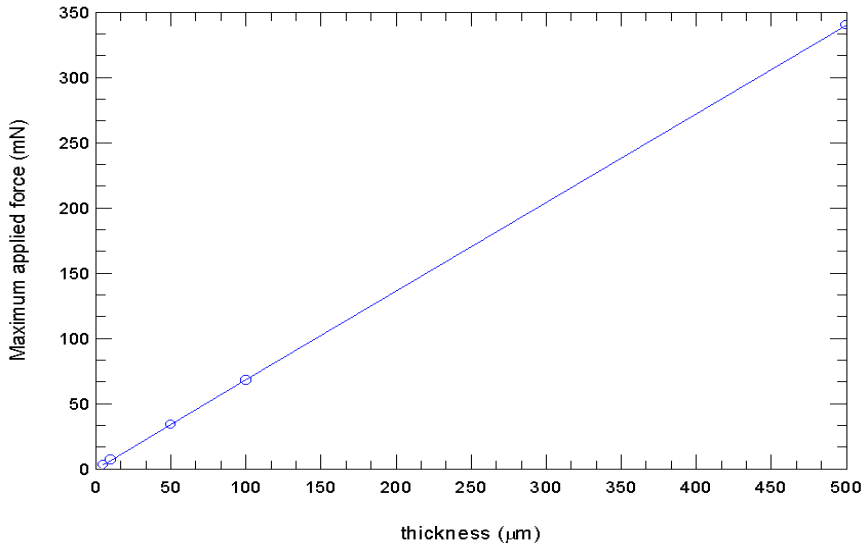

Figure 11. Variation of the maximum applied force to break the microstructures as a function of its thickness.

From the results of Fig. 11, we extrapolate the force of your 45µm microstructure and obtained a value around 30 mN which correspond approximately to a weight of 3 grams (3gf).

We are now applying this method to analyze the buckle of the microstructure induced to the not compensated mechanical stress caused by the overlaying films.

5. Electrochemical characterisation

In order to analyse the microelectrode area, we used an electrochemical technique called cyclic voltammetry, performed by a computer controlled electrochemical workstation - CV-50W (BAS), as detailed in a previous work (Fontes, 1998).

This experiment is based on a redox process of an ion (Montenegro , 1990 and Brett, 1994), produced by sweeping the electrode potential and recording the current (I) generated from the electron exchanged between the electrode and the ion in solution. For a constant sweep rate, the maximum current called diffusion current (I_L), is directly proportional to the electrode geometry, manly its radius (r) and to the redox species concentration (C), as described in equation 1. The square shape electrode area (L^2) is obtained by area equivalency with the circular shape electrode, Eq. (2).

We have used a standard solution of potassium ferricyanide $K_3(Fe(CN))_6$ in 0.5 M KCl at room temperature. The ferricyanide concentration was varied from 1mM to 10 mM (2.5 mM step) and the applied potential was from 600mV to -300mV with sweeping rate of 100mV/s. From equation 1, a linear relationship between the peak current and the concentration is expected. This procedure was performed to all the eight working electrodes and an external (Ag/AgCl) reference electrode was used. We evaluated the diffusion current at the potential of -100mV.

$$I_L = 4.n.F.D_o.C.r \quad (1)$$

$$L^2 = \pi.r^2 \quad (2)$$

In Eq.(1) n is the electron transference in the reaction (n =1 in our case), F represents the Faraday constant ($F=9{,}6485x10^4$ C/mol), D_o is the ferricyanide diffusivity ($D_o=7{,}6x10^{-6}$ $cm^2.s^{-1}$), C is its concentration (10 mM/dm^3) and r is the electrode radius.

Figure (12) presents the results for one of the working electrodes. Fig. (12a) displays the cyclic voltammograms. The expected linear increase of the peak current with the ferrycianade concentration was observed, Fig. (12b). From the calculated area for all electrodes we obtained a mean value of 129.9 μm^2 (L=11.4µm) showing a good agreement with AFM measurements.

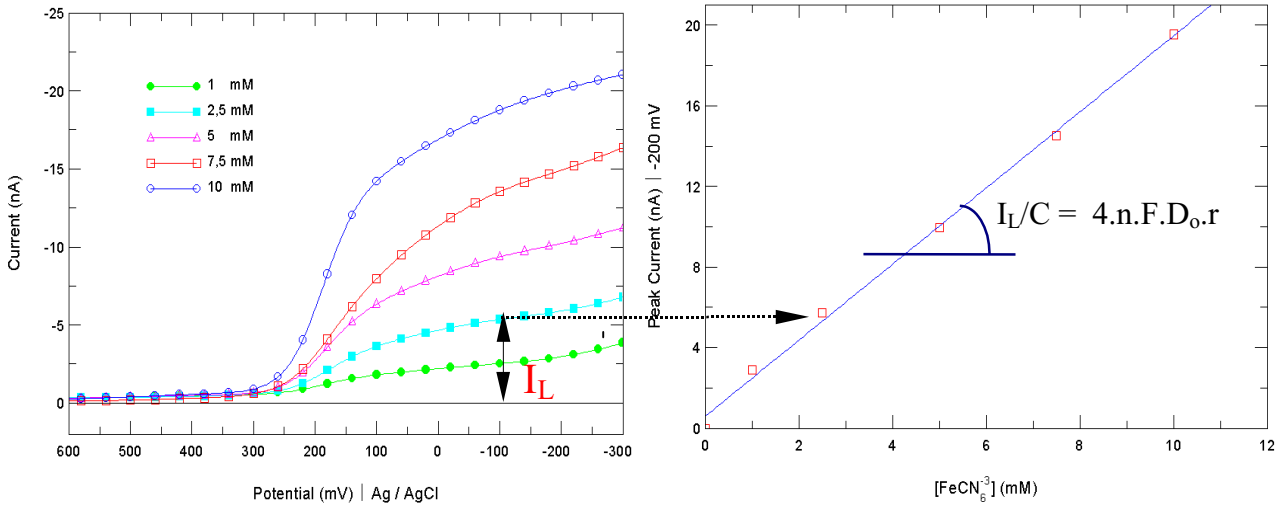

Figure 12. Results for the sensor electrochemical characterisation: a) response from one of the detection electrodes in the cyclic voltammetry experiment for increasing ferricyanide concentrations; b) diffusion current as a function of the $[Fe(CN)_6^{-3}]$ evaluated at -100 mV.

Conclusions

We have presented in this paper a complete fabrication of a high reproducible micromachined multidetection silicon probe for biological applications. Two techniques were proposed for the probe fabrication: etching stop and plasma etching, where this last one presented better characteristics of shape definition and processing time.

Several probe designs were explored by varying the number of the detection electrodes. Silicon tips dimensions from 90 µm to 340 µm were obtained with a thickness of 15 µm.

For the etch stop processing, SIMS analysis was used to quantify the boron concentration, resulting a value of $2.4x10^{19}$ at./cm^3 which corresponds to a decreasing of the silicon etching rate around 5 times.

Bent structures were obtained after the complete process due to an uncompensated mechanical stress between SiO_2 and Si_3N_4, probably caused by deposition technique used. This mechanical deformation caused damages in some protective layer and interconnection lines, decreasing the processing yield.

By increasing the probe thickness, using plasma etching technique, we found a compromise between layer integrity and minimal probe thickness, resulting in a thickness value higher than 30 µm.

Final devices of 45 µm were produced with a yield of up to 80%, showing the expected silicon micromachnig reproducibility.

Results from numerical simulation using Ansys® pointed that a force around 30 mN would be enough to break the microstructure with 45 µm in its tip part, where the internal mechanical stress surpass the silicon rupture stress.

Electrochemical characterization of the sensing areas of the fabricated sensor reveal a value of around 130µm^2 (L= 11.4 µm) with good agreement with AFM measurements.

Changes in the processing are being carried out by taking advantage of materials fully compatible with the silicon microelectronic technology, such as aluminum and polysilicon and producing thinner probes.

Acknowledgements

The authors wish to acknowledge the financial support of the Brazilian agencies: Capes, CNPq, and CNPq/PADCT/CDCT. Also, we would like to thank the Center for Sensor Technology and LRSM at UPENN. At last but not the least the authors wish to thanks Dr. Ronaldo Mansano for the plasma etchings and Dr. Eliphas Simões for the valuable discussions on the Ansys® simulations.

References

Acher S., 1993. Measurements of Nitric Oxide in Biological Models, The FASEB Journal, vol. 7, Feb.

"Ansys User's Manual, 1994, Volume I - Procedures", chapter 3 and Volume III – Elements, chapter 4.

Brett, C.M.A. and Brett, A.M.O.; 1994, Electrochemistry - Principles, Methods, and Applications; Oxford University Press.

Bruce, D.M., 1997, Annel Treatment Studies of Heavily Boron-Doped Silicon Proceedings of SPIE, Micromachining and Microfabrication Process Technology III, Volume 3223, pp. 270-275. Chang, Pang (Ed.), Austin.

Cobbold, R.S.C, 1974, Transducers for Biomedical Measurements: Principles and Applications, John Wiley & Sons, cap. 10 (3).

Fontes , M.B.A., 1999, Development of a Nitric Oxide Sensor based on Silicon Planar Technology, Phd Thesis.

Polytechnic School, University of São Paulo, Brazil.
Fontes, M. B. A., Araki, K., Furlan, R., Santiago-Avilés, J. J., 1999, A Simple Silicon Based Nitric Oxide Sensor, Procceding of IMECE, Mems vol. 1, pp. 603-607, Nashville, Tennessee, 14-19 Nov.
Fontes, M. B. A., Angnes, L., Araki, K., Furlan, R., Santiago-Avilés, J. J., 1999, Nitric Oxide Sensor based on Silicon Planar Technology, International Conference on Microelectronics and Packaging - ICMP'99, pp. 252-256, Campinas, SP, Brazil, 3-6 August.
Fontes, M. B. A., Angnes, L., Araki, K., Furlan, R., Santiago-Avilés, J. J., 1998, A Study of Modified Silicon Based Microelectrodes for Nitric Oxide Detection, First Iberoamerican Congress on Sensors and Biosensors - IBERSENSOR'98, Havana , Cuba, 9-13 Nov.
Fontes , M. B. A., Furlan, R., Santiago-Avilés, J. J., 1997, Development of a Silicon Microprobe for NO Detection, in Proceedings of SPIE, Micromachining and Microfabrication Process Technology III, Volume 3223, pp. 64-71. Chang, Pang (Ed.), Austin.
Fontes, M. B. A., Pilloud, D.L., Farid, R.S., Rabanal, F., Araki, K., Santiago-Avilés, J.J., Dutton, P.L., Toma, H., 1995. Detection of NO Using NI-Porphyrins and a Self-Assembled Monolayer of Hemopeptide as Modified Electrodes for a Silicon Integrated Microsensor, Electrochemical Society Proceedings Volume 95-27, 192.
Geddes, L.A., Baker, L.E., 1989, Principles of Applied Biomedical Instrumentations, John Wiley & Sons, cap. 9.
King, J. A., 1988, "Materials Handbook For Hybrid Microelectronics", Artech House, London, pp 106.
Madou, M., 1997, Fundamentals of Microfabrication, CRC Press.
Malinsky, T., Taha, Z, 1992, Nitric Oxide Release from Single Cell Measured In Situ by a Porphyrinic-Based Microsensor, Nature, vol 358, August.
Mansano, R.D., Silicon Plasma Etching for Microchannel Application, PhD Thesis1998, Polytechnic School, University of São Paulo, Brazil.
Mansano, R.D., Verdonck, P., Maciel H.S., Massi M. 1999, "Anisotropic inductively coupled plasma etching of silicon with pure SF6", "Thin Solid Films" vol. 343-344, pp. 381 –384.
Mansano, R.D., Verdonck, P., Maciel, H.S., 1998 " Anisotropic reactive ion etching in silicon, using a graphite electrode" Sensors and Actuactors A, 65, 180.
Mansano, R.D., Verdonck, P., Maciel, H.S., 1997, "Mechanisms of surface roughness induced in silicon by fluorine containing plasmas" in Vacuum, vol. 48, number 7-9 pp. 677-679, Sept.
Mansano, R.D., Verdonck, P., Maciel, H.S , 1996. "Deep trench etching in silicon with fluorine containing plasmas" Applied Surface Science vol. 110/101 pp. 583-586.
Montenegro, M.I et al, 1990; Microelectrodes: Theory and Applications; Proceedings of the NATO Advanced Study Institute on Microelectrodes: Theory and Applications, , Alvo, Portugal, May 14-26.
Najafi, K., Wise, K.D., Muchizuki, T., 1985, A High-Yield IC-Compatible Multichannel Recording Array, IEEE Trans. Elect. Dev., vol ED-32, No.7, July.
Popov, E. G., 1968, "Introduction to Mechanics of Solids". Prentice Hall, New Jersey, pp. 527.
Prohaska, O., J., Olcaytug, F., Pfundner, P., Draguan, H., 1986, Thin-Film Multiple Electrode Probes: Possibilities and Limitations, IEEE Trans. Biom. Eng., vol. BME-33, no 2, Feb.
Timoshenko, S. P., Gere, J. E., 1988, "Mechanics of Materials", Wadsworth International Group, New York, chapter 1.

XVI CONGRESSO BRASILEIRO DE ENGENHARIA MECÂNICA
16th BRAZILIAN CONGRESS OF MECHANICAL ENGINEERING

MICROSENSOR FOR GAS FLOW MEASUREMENTS

Roberto Jacobe Rodrigues
University of São Paulo, LSI – PSI – EPUSP
Av.: Prof. Luciano Gualberto, Trav.: 3 – n°.: 158 – Cidade Universitária – São Paulo – S.P. – CEP.: 05508 - 900
e-mail: rjacobe@lsi.usp.br

Rogério Furlan
University of São Paulo, LSI – PSI – EPUSP
Av.: Prof. Luciano Gualberto, Trav.: 3 – n°.: 158 – Cidade Universitária – São Paulo – S.P. – CEP.: 05508 - 900
e-mail: furlan@lsi.usp.br

Abstract: This work presents the design of a gas flow microsensor that was implemented by using silicon microelectronics technology. Its main features are a low power consumption (tens of mW) and the possibility of integration in flow microactuators. It was adopted a calorimetric device with free - standing microfilaments as thermoresistive sensor elements. Analytical and numerical modelings were developed for device analyses and design. The free - standing microfilaments were fabricated using surface micromachining. Experimental characteristic curves of output voltage vs. flow were obtained by using a commercial flow sensor for calibration. A good agreement was obtained comparing the flow microsensor experimental characteristic curves with numerical simulation results. The miniaturization of sensor devices using semiconductor technology results in higher performance, as faster response, lower power consumption, and measurement of small flow. Important applications of a flow sensor can be found in chemical, medical, automotive, and industrial areas.

Keywords: flow sensors, micromachining, thermoresistive and calorimetric principle

1. Introduction

The application of microelectronics technology permits to build high performance flow microsensors on silicon substrates (Hocker, 1985;Yoon, 1990 and Qio, 1996). These devices have been successfully used in medical, chemical, industrial and automotive areas, among many others (Yoon, 1990). Besides, there is the possibility of integration with flow microactuators (Zemel, 1996 and Jiang, 1999).

The microsensor presented in this work is based on the calorimetric principle (Qio, 1996) and consists of three free -standing microfilaments fabricated by surface micromachining (Simões, 1997). These microfilaments are aligned as showed in the Fig. (1). The middle one is used as a heater and the other two as sensors (thermoresistors), symmetrically positioned on either side of the heater. The difference between the downstream and upstream temperatures depends on the flow velocity and can be detected by a Wheatstone bridge (Yoon, 1990 and Qio, 1996).

Analytical and numerical modelings were developed to help in the microsensor design. The designed structure was fabricated and analyzed in terms of nitrogen flow.

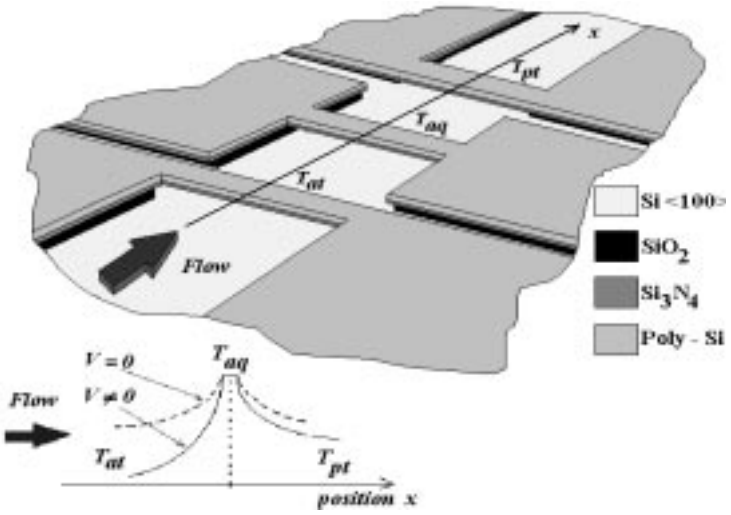

Figure 1. Schematic illustration of the flow microsensor based on the calorimetric principle built in this work (Rodrigues, 1999).

2. Analytical Model

The temperature distribution in the flow field is governed by the energy equation, which can be derived by writing an energy balance according to the principle of conservation of energy for a differential area element in the flow field. This balance is presented by Incropera and DeWitt (1996).

We assume the flow as: external, laminar, steady and with an incompressible fluid. The velocity components are considered only in the x direction as showed in the Fig. (2a). Other approximation, as suggested by Lammerink et all (1993), will be to consider the temperature distribution in the fluid as being linear in the y direction as showed in the Fig. (2b).

Thus, the energy equation used to obtain the temperature distribution, $T(x)$, is a non-homogeneous and linear differential equation, with constant coefficients. This differential equation corresponds to Eq. (1):

$$D.\frac{\partial^2 T(x)}{\partial x^2} - u.\frac{\partial T(x)}{\partial x} - \frac{D}{R^2}.T(x) = -\frac{D.T_a}{R^2} \tag{1}$$

Where u is the x direction velocity component and the thermal properties are: ρ the fluid density (kg/m^3), k the fluid thermal conductivity (W/m. K) and c the fluid heat capacity (kg/m^3). The thermal diffusivity of the fluid is $D = k/\rho.c$ (m^2/s). The flow channel diameter is 3 mm.

This differential equation will be solved for a heater resistor with width, $2L$ = 10 μm and heater temperature, T_0 = 373 K. It was considered an ambient temperature, T_a = 300 K. The temperatures are calculated, after solving Eq. (1), in x_m positions as showed in the Fig. (2a).

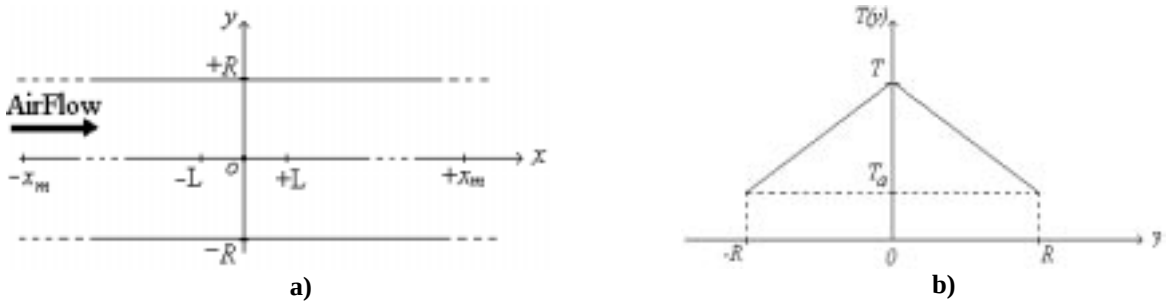

a) **b)**

Figure 2. Analytical model: a) x-y plane of flow channel with important dimensions and b) considered temperature profile in the y direction.

The temperature distribution $T(x)$ is obtained from the solution of the energy equation, Eq. (1), subjected to the appropriate boundary conditions, presented below:

$$\begin{aligned} |x| >> L \quad &\Rightarrow \quad T(x) = T_a \\ |x| > L \quad &\Rightarrow \quad T_a < T(x) < T_0 \\ -L \le x \le L \quad &\Rightarrow \quad T(x) = T_0 \end{aligned}$$

After solving the Eq. (1), the solutions below were obtained:

$$x < -L \Rightarrow T(x)=(T_0 - T_a).\exp[\lambda_1.(x + L)] + T_a; \tag{2a}$$
$$-L \le x \le L \Rightarrow T(x)=T_0, \tag{2b}$$
$$x > L \Rightarrow T(x)= (T_0 - T_a).\exp[\lambda_2.(x - L)] + T_a \tag{2c}$$

The Eq. (2b) consists in the heater resistor temperature. The λ_1 and λ_2 values, presented in the Eq. (2a) and Eq. (2c), are found from Eq. (3).

$$\lambda_{1,2} = \frac{1}{2.D}.\left[v \pm \sqrt{v^2 + 4.\left(\frac{D}{R}\right)^2} \right] \tag{3}$$

Figure (3) shows the obtained temperature distribution on positions in the *x* direction upstream and downstream to the heater. It was considered airflow.

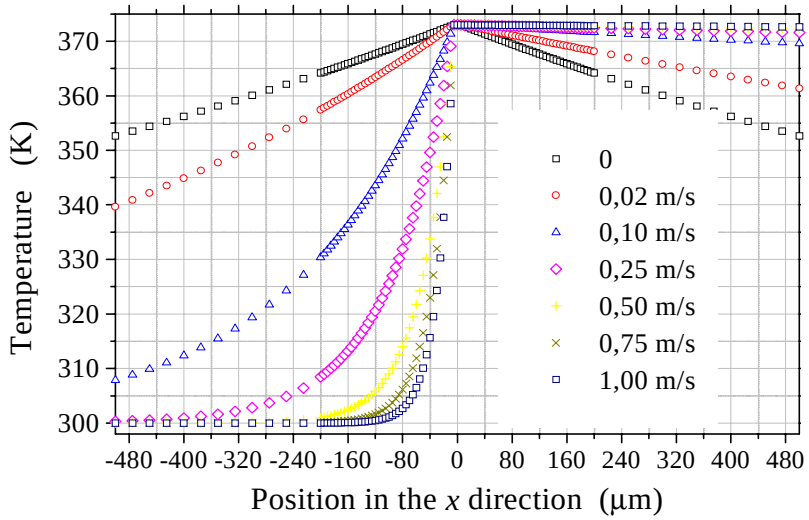

Figure 3. Temperature distribution obtained with the analytical model (Rodrigues, 1999).

Figure (4) shows the temperature difference between the downstream ($+x_m$) and upstream ($-x_m$) sides of the heater as a function of the flow velocity.

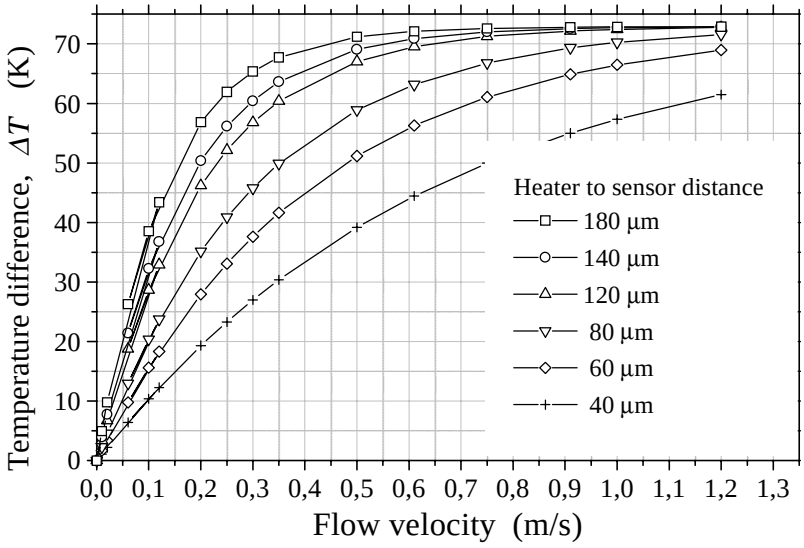

Figure 4. Characteristic curves obtained with the analytical model of the flow microsensor (Rodrigues, 1999).

The analytical model results agree qualitatively with previous results found in literature (Hocker, 1985; Yoon, 1990 and Qio, 1996) as presented in the Fig. (5). Also, the sensor – heater distance could be found in the range of 100 µm.

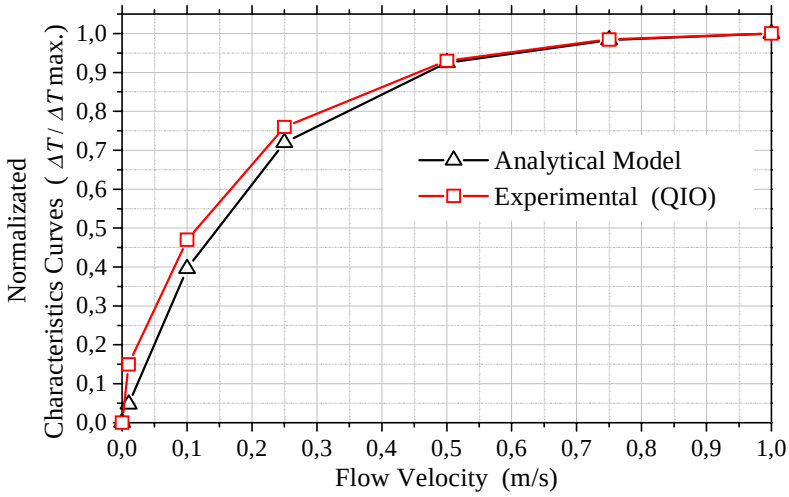

Figure 5. Comparison between experimental results presented by Qio et all (1996), and the developed analytical model (Rodrigues, 1999).

3. Numerical Simulation

The simulations were performed using the software package ANSYS®/FLOTRAN® after to consider a two – dimensional model corresponding to the cross – section through the sensor and channel system. The heater resistor with a width of 10 μm and a thickness of 0,8 μm was considered as built on a silicon substrate with a width of 3 mm and a thickness of 300 μm. The heater to substrate distance was 0,7 μm. The heater resistor was formed by polysilicon and silicon nitride layers.

The velocity of the airflow was varied from 0 to 1 m/s with corresponding flow rates in the range of 0 to 500 sccm, for a channel with a diameter of 3 mm. The heater temperature was 373 K.

Figure (6) presents a two-dimensional representation of the temperature distribution around heater in the flow channel.

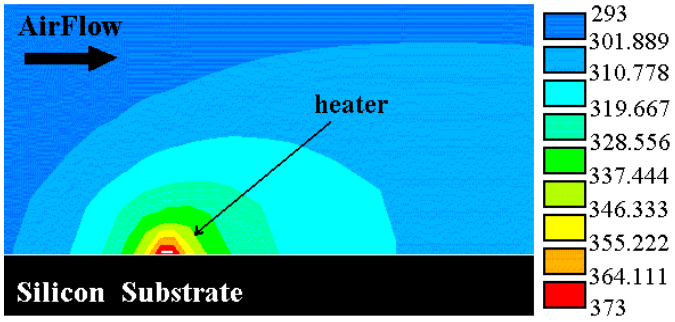

Figure 6. Temperature distribution in the flow channel, in the nearness of heater and for a flow of 500 sccm.

Figure (7) shows the temperature distribution obtained from the simulations results.

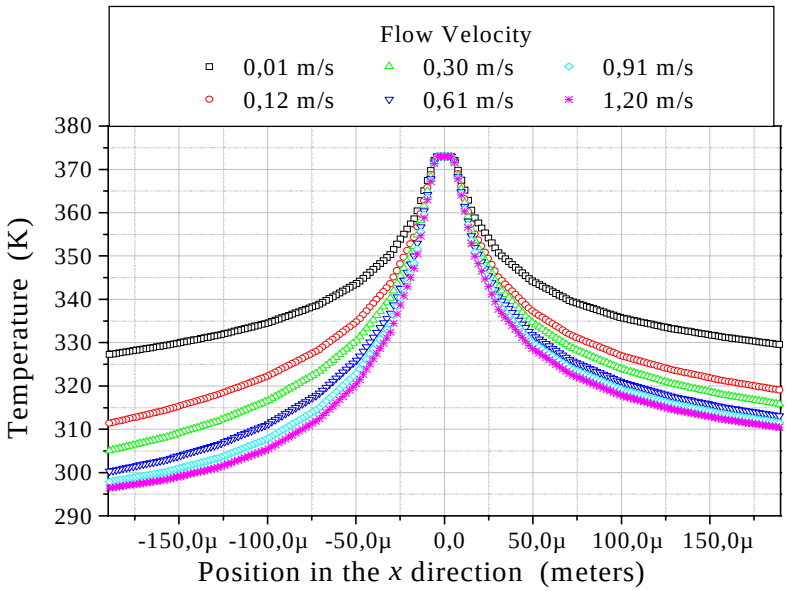

Figure 7. Temperature distribution obtained from the simulation results.

The corresponding characteristic curves, presented in Fig. (8), were obtained for different, upstream and downstream, symmetrical positions on either side of the heater.

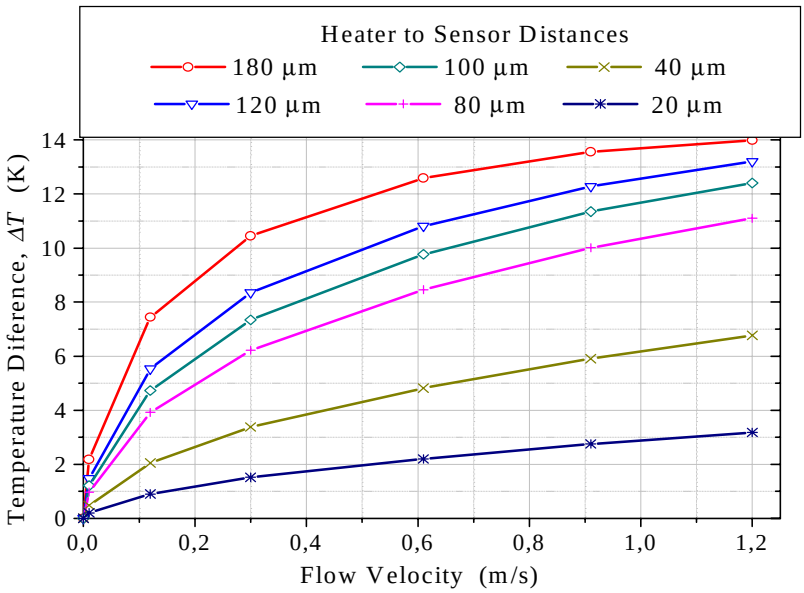

Figure 8. Characteristic curves obtained from numerical simulation performed for different heater to sensors distances, used in the device design.

Thus, the better distance between heater and temperature sensors was determined as either 80 µm or 120 µm. High sensitivity was considered in this choice.

Only the heater resistor is considered in the simulation because the heat dissipation in the sensors is so small that they do not significantly modify the temperature distribution resulting from the dissipation in the heater resistor and the fluid flow (Lammerink, 1993).

4. Device Fabrication

Figure (9) shows the schematic cross section of the main processing steps for fabrication of the flow microsensor (Rodrigues, 1999). Silicon wafers were used as substrate.

A layer of 0.6 µm of PECVD oxide was deposited in TEOS (Tetra-Ethyl-Ortho-Silicate) ambient (Silva, 2000). Layers of Si_3N_4 and polysilicon were deposited by LPCVD, with thickness of 0.15 µm and 0.5 µm, respectively. The polysilicon doping was performed through phosphorus (PSG) diffusion after thermal step.

Plasma etching was performed for polysilicon electrical contacts and temperature sensors definition after photolithography. The aluminum layer was deposited by evaporation and patterned to form electrical contacts through wet chemical etching.

The wafers were cut for devices definition and the sacrificial layer removal was performed in DLV solution, 6NH4F + 1HF (25 °C).

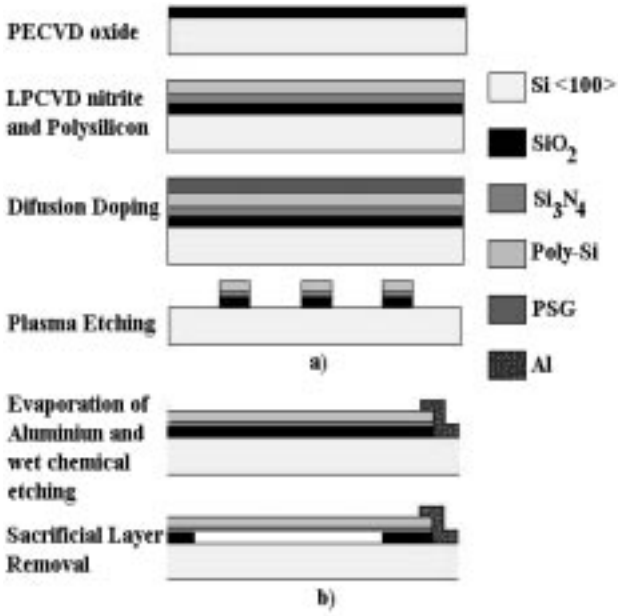

Figure 9. Main process steps for fabrication of the flow microsensor for: a) transversal and b) longitudinal view of filaments.

Figure 10 shows a microphotograph of the fabricated microsensor.

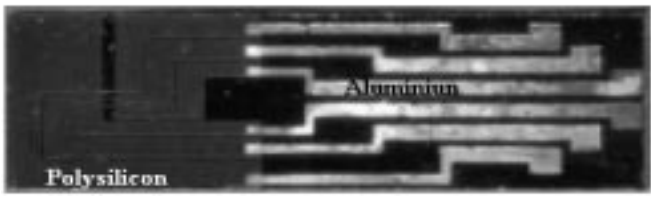

Figure 10. Microsensor top view.

The device was glued in a plate and attached in tube with a diameter of the 3 mm, as shown in the Fig. (11), for the experimental measurements.

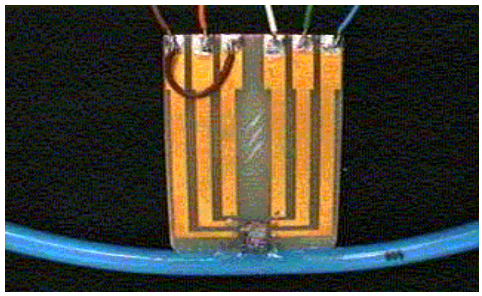

Figure 11. Photograph of the mounted device attached in a tube, for tests.

5. Results and Discussions

The free - standing filaments obtained were tested through *i* x *v* curves. Red - light emission was observed only for free - standing filaments under voltages close to 11 V. Thus, becoming evident that the filaments were released (Simões, 1997 and Rodrigues, 1999). The power dissipation in the heater is close to 50 mW, for an applied voltage of 6 V.

Tested devices were installed in series with a commercial mass flow meter, as shown in the Fig. (12). Thus, characteristic curves were obtained, i.e. output voltage of Wheatstone bridge as a function of the flow measured by means of commercial mass flow meter (Rodrigues, 1999). With this aim, the microsensor was inserted in a tube with 3 mm of diameter as showed in Fig. (11), and tested with nitrogen in a flow range of 0 to 500 sccm.

Characteristic curves were obtained for different heater voltages and compared with numerical results. The characteristic curves obtained for heater to sensors distance of 80 µm showed smaller sensitivity than those obtained for 120 µm (Rodrigues, 1999).

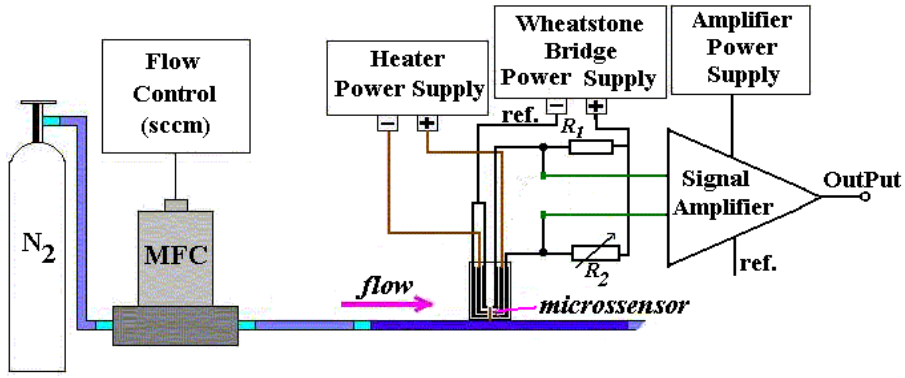

Figure 12. Experimental Setup.

To make possible the direct comparison between numerical and experimental results, voltage was used instead of temperature. Thus, the temperatures obtained numerically were converted to voltage obtained in the Wheatstone bridge amplified output by considering linear dependence between electrical resistance of temperature sensors and temperature.

Figure (13) shows the comparison between characteristics curves obtained for numerical simulation and experimental results for distance heater – sensors of the 120 µm.

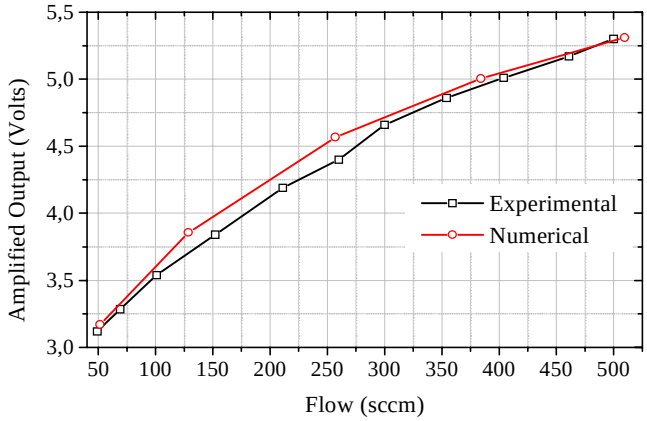

Figure 13. Comparison between characteristic curves obtained from numerical and experimental results for quantitative analysis after to consider the possibility of a partial removal of the sacrificial layer on the numerical results.

The two curves display a similar behavior. The possibility of a partial removal of the sacrificial layer is pointed as the cause of a sensitivity decrease.

Notice that the gas flow unit is usually presented in terms of the “standard cubic centimeters per minute”(sccm), that corresponds to the fluid volume, in cm^3, that through a transversal section per minute. This measurement is made in the standard conditions: 1013 mbar and 0 ^oC (Douglas, 1985).

6. Conclusions

A low power flow microsensor (about 30 mW) consisting of three free - standing microfilaments has been fabricated and tested.

An analytical model and numerical simulations have been used to predict the experimental results through temperature distributions around the heater. The good agreement between analytical, numerical and experimental results obtained in this work shows the consistence of our design methodology.

The comparison between experimental and numerical results was performed through characteristic curves. The appropriate distance between the heater and the sensor elements was determined and resulted in the range of 120 µm. Differences in the qualitative analysis between numerical and experimental results suggest that part of the filaments are in thermal contact with the substrate, what is probable due to both small thickness of the sacrificial oxide layer (0,6 µm) and stress in the polysilicon structures.

7. Acknowledgements

We would like to acknowledge the financial support of FAPESP, CNPq, and PADCT.

8. References

Douglas, J.F.; Gasiorek, J.M.; Swaffield, J.A., 1985, “Fluid Mechanics”, Longman Scientific and Technical, 2.ed. England.

Hocker, G. B., Johnson, R. G., Higashi, R. E. and Bohrer, P. J., 1985, “A microtransducer for Air Flow and Differential Pressure Sensing Applications”, Micromachining and Micropackaging of Tranducers, Amsterdam, pp. 207-214.

Incropera, F. P. and DeWitt D. P., 1996, “Fundamentals of Heat and Mass Transfer,” 4°ed., John Wiley and Sons, Inc.

Jiang, L., Wang Y., Wong M. and Zohar Y., 1999, “Micro-Channels with Suspended Temperature Sensors for Heat Transfer Study”, Microelectromechanical Systems (MEMS), vol.1, pp. 567-573.

Lammerink, T. S. J., Tas, N., Elwenspoek, R., M. and Fluitman, J.H.J., 1993, “Micro-Liquid Flow Sensor”, *Sensors and Actuators A37-A38*, pp.45-50.

Qio, L., Hein, S., Obermeier E. and Schubert A., 1996, “Micro-Gas-Flow Sensor with Integrated Heat Sink and Flow Guide”, *Sensors and Actuators A5*4, pp. 547-551.

Rodrigues, R. J., 1999, “Microsensor de Vazão Implementado em Silício”, Ms. Dissertation, University of São Paulo, September.

Silva, A. N. R., 2000, “Estudo e Caracterização do Processo PECVD-TEOS para a Deposição de Filmes de Óxido de Silício e Estudo de Interfaces”, Ph.D. Thesis, University of São Paulo, April.

Simões, E. W., Furlan, R., Morimoto, N. I., Bonnaud, O., Da Silva, A. N. R. and Da Silva, M. L. P., 1997, “PECVD SiO2 Sacrificial Layers for Fabrication of Free-Standing Polysilicon Filaments”, Proceedings of International Conference on Microelectronics and Packaging, July.

Yoon, E., 1990, “An Integrated Mass Flow Sensor with On-Chip CMOS Interface Circuitry”, Ph.D. Thesis, University of Michigan.

Zemel, J. N. and Furlan, R., 1996, “Microfluidics”, Handbook of Chemical and Biochemical Sensors, J. S. Schulz, Editor, Inst. of Phys. Inc, Philadelphia, PA.

XVI CONGRESSO BRASILEIRO DE ENGENHARIA MECÂNICA
16th BRAZILIAN CONGRESS OF MECHANICAL ENGINEERING

Deposition and Characterization of LPCVD Polycrystalline Silicon

Ricardo Cotrin Teixeira
Centro de Componentes Semicondutores – Universidade Estadual de Campinas.
Cidade Universitária Zeferino Vaz
Rua Pandiá Calógeras, 90
CEP: 13083-970 Caixa Postal 6061
Campinas – SP – Brasil
ricardocotrin@ig.com.br

Ioshiaki Doi
Departamento de Máquinas, Componentes e Sistemas Inteligentes
Faculdade de Engenharia Elétrica e de Computação, e
Centro de Componentes Semicondutores – Universidade Estadual de Campinas
Cidade Universitária Zeferino Vaz
Rua Pandiá Calógeras, 90
CEP: 13083-970 Caixa Postal 6061
Campinas – SP – Brasil
ioshiaki@uol.com.br

Maria Beny Zakia
Centro de Componentes Semicondutores – Universidade Estadual de Campinas
Cidade Universitária Zeferino Vaz
Rua Pandiá Calógeras, 90
CEP: 13083-970 Caixa Postal 6061
Campinas – SP – Brasil
beny@led.unicamp.br

Jacobus Willibrordus Swart
Departamento de Semicondutores, Instrumentos e Fotônica
Faculdade de Engenharia Elétrica e de Computação, e
Centro de Componentes Semicondutores – Universidade Estadual de Campinas
Cidade Universitária Zeferino Vaz
Rua Pandiá Calógeras, 90
CEP: 13083-970 Caixa Postal 6061
Campinas – SP – Brasil
jacobus@led.unicamp.br

José Alexandre Diniz
Centro de Componentes Semicondutores – Universidade Estadual de Campinas.
Cidade Universitária Zeferino Vaz
Rua Pandiá Calógeras, 90
CEP: 13083-970 Caixa Postal 6061
Campinas – SP – Brasil
diniz@led.unicamp.br

Abstract:
Polycrystalline Silicon (Poly-Si) is a widely used material in microelectronic industry since the 70's. Recent researches have pointed its use in electro-mechanical systems, like floating bridges and membranes or micro-robots and micro-machines. Aiming for these and other applications a low-pressure chemical vapor deposition reactor (LPCVD reactor) was adapted from an old reactor working at atmospheric pressure and set up at Center for Semiconductor Components in Campinas State University. Poly-Si thin films were grown from pure or hydrogen diluted Silane (SiH_4) and had been analyzed by AFM, X-Ray Diffraction and Raman Spectroscopy. The results showed that poly-Si films can be grown in this reactor in a wide range of conditions, varying deposition pressure from 1.5 up to 100 Torr and temperature deposition between 680° to 1000° C, with growth rates of some hundreds Å/min. Sheet resistance measured by 4-point probe method showed that ion implanted phosphorus doped films annealed in RTP are of high quality and can be used as gate electrode in MOS transistors.

Keywords: *Polycrystalline Silicon, LPCVD, Thin Films, Deposition, Characterization*

1. Introduction

Polycrystalline Silicon (poly-Si) is a well-known and widely used material in microelectronics. Its importance and variety of applications can be seen by the great amount of publications about the film and its properties.

Among a variety of applications of poly-Si, we can emphasize its use as gate electrode in MOS (Metal–Oxide–Semiconductor) structures in replacement of Aluminum. This is the main goal of this work. The poly-Si gate electrode MOS structure presents several advantages in comparison with the Aluminum gate technology, such as the following (Kamins, 1998):

- Poly-Si–Silicon Oxide interface is more stable than Aluminum–Silicon Oxide. Al reacts with the Oxygen and produces Al_2O_3, which changes device characteristics as the threshold voltage (V_T) and dielectric breakdown. The poly-Si-Si interface at the source and drain areas is also of higher quality. In Al electrode technology a problem of junction spiking that occur at the Al-Si interface when this interface is heated, is one of the concerns. This problem is related to the Silicon solubility in Aluminum that rises as the temperature increases and to a quite high diffusibility of Silicon along the grain boundaries of the Aluminum at the temperature used for the process. Thus a significant quantity of silicon can move from the region below metal-Si interface into aluminum film and, simultaneously, Aluminum from the film will move to fill the voids created by the departing Si. If Aluminum penetration takes place deeper than p-n junction depth below the contact, it leads to a junction spiking, which can also destroy the device.
- Poly-Si makes possible the use of self-aligned structures, which simplifies the fabrication sequence, increases packing density and reduces the gate-source and gate-drain parasitic capacitances. These capacitances limit speed operation and they arise from the fact that the gate area must cover the whole channel area, joining source and drain for transistor operation. Since in Aluminum technology the active areas have to be doped prior to the gate oxide deposition, an extra border is needed to ensure gate coverage of the whole extension of the channel and operation of the device. Poly-Si allows the gate area to be defined before the formation of the active areas, unlike Al technology. Source and drain are open through the poly-Si layer and the doping is simultaneous to the gate area or even afterwards. Thus, alignment problems are minimized and a smaller number of masks are necessary in Si-gate technology. The exclusion of the overlap areas in self-aligned structures also increases integration of devices.
- While in Al's technology V_T is solely defined by gate oxide thickness, poly-Si technology allows V_T value to vary more than 0,5 V by just changing the gate doping. Poly-Si doping changes its material work function as well as its Fermi level position and as its consequence, the metal-semiconductor work function difference (Φ_{MS}), used in V_T calculation. (Ferreira 1984)

In spite of all these advantages, the use of the metal cannot be totally discarded for applications in the advanced VLSI technology. Even when doped at the highest practical concentration, the poly-Si still presents a significantly higher resistivity when compared to Al. A 0,5 μm thick poly-Si has sheet resistance of about 20 Ω/ , compared to 0,05 Ω/ for a 0,5 μm thick Al film. The resulting high values of the interconnect line can lead to a propagation delays and dc voltage variations within the circuits. Thus, in the Si-gate technology, two interconnection plans for the devices are available, the one of the poly-Si and the other one of Al, what allows the construction of more complex circuits and offers a very larger flexibility for IC design (Ferreira, 1984; Kamins, 1998).

Among other applications, poly-Si is used in resistors; bipolar transistors; Thin Film Transistors (TFT); Micro-Electro-Mechanics Systems (MEMS) and solar cells. Each application requests poly-Si films with specific characteristics and several types of reactors and growth and doping conditions are used for this trend.

Looking for these advantages and the wide application of poly-Si, an epitaxial CVD Vertical Reactor (Vertical Reactor) originally projected to deposition of single-crystalline Silicon (epi-Si) from Silane (SiH_4) at atmospheric pressure was modified to allow Low Pressure Chemical Vapor Deposition (LPCVD) of poly-Si thin films.

In this work, we present some morphological and electrical characteristics of poly-Si thin films deposited in this reactor in several LPCVD process conditions.

2. Experimental

The poly-Si films were deposited in a modified vertical type CVD epitaxial reactor using 100% SiH_4 and Hydrogen diluted SiH_4. The experimental arrangement is schematically shown in Fig (1). The reaction chamber is constituted by a quartz bell jar, and a graphite made susceptor. Gases used in the process are introduced into the reactor in an ascending flow from a 3/8 in. diameter quartz tube located in the middle of the susceptor. Substrates are heated to the required deposition temperature by a RF heating (10 KHz, 30 KVA) by a induction coil located just below the graphite susceptor. The susceptor is provided with a rotating mechanism in order to ensure uniform gas and temperature distribution on the samples.

The depositions proceed in 2 different reaction atmosphere: of 100% SiH_4 and Hydrogen diluted SiH_4. Process parameters for each one are presented in Table (1):

The substrates used for poly-Si deposition was a 2-in. <100> oriented p-type silicon wafer covered with a 0,6 μm thermal oxide layer. The deposition temperature was monitored by an infrared optical pyrometer and rate flow of reagent gases were controlled with a Mass Flow Meter ($QSiH_4$) and rotameter type flow meter (QH_2). All experiments were carried out with a deposition time of 30 minutes.

Table 1: Process Conditions used in the PMC 200 CVD Vertical Reactor for Poly-Si low-pressure deposition

	100% SiH_4	$SiH_4 + H_2$
Pressure	0,3 – 5 Torr	5 – 100 Torr
Temperature	580 – 800 °C	620 – 1000 °C
$QSiH_4$	10 – 60 sccm	10 – 60 sccm
QH_2	0 sccm	980 – 36.100 sccm

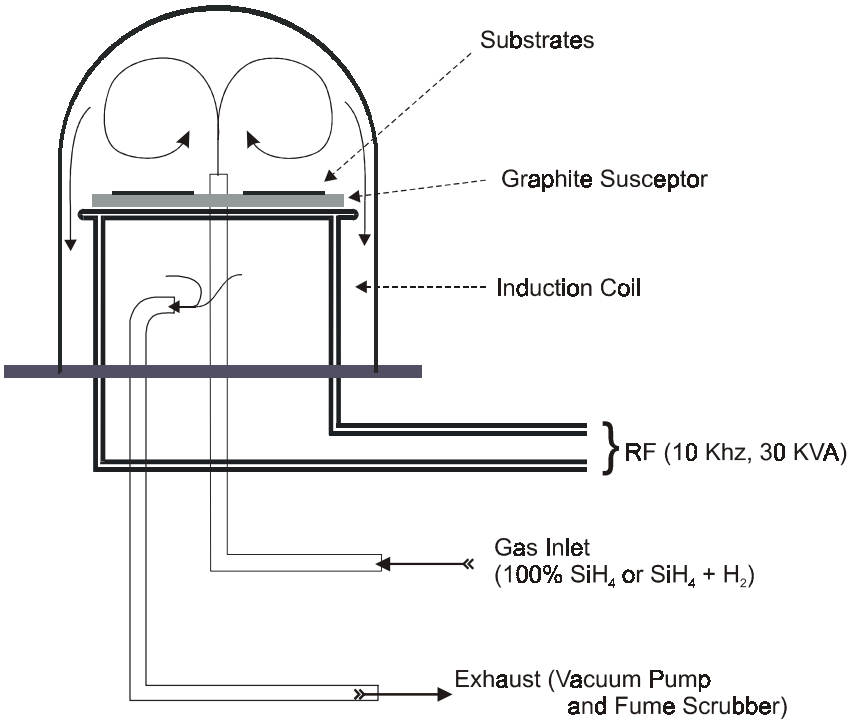

Figure 1: Schematic of the Experimental Assembly used for poly-Si deposition.

Raman Spectroscopy (Raman spectrum) and X-Ray Diffraction (XRD) were used to characterize crystal structures and grain size and Atomic Force Microscopy (AFM) in contact mode to determine surface roughness. Electrical properties (sheet resistivity) were measured in P-doped implanted samples (150 keV, $1x10^{16}$ cm^{-2} and $2x10^{16}$ cm^{-2}) by 4-point probe technique.

3 Results and Discussion

3.1 Raman Spectroscopy

Micro-Raman Spectroscopy gives a fast qualitative view of the deposited film and is non-destructive.

Single-crystal Si or poly-Si Raman Spectrum is well known, presenting a strong and strain peak around 522 cm^{-1}, due to well defined energy levels, characteristic of a periodic bonds structure (crystal). The amorphous phase presents a broadband in the 460-490 cm^{-1} range (maximum at about 483 cm^{-1}), because the disordered bonds don't present any kind of symmetry and several vibration modes are detected (Harbeke, 1984). Once poly-Si is composed of small crystalline grains, each one a single-crystal, and amorphous areas in the boundaries between one and another grain, its spectrum comes as an overlap of both Silicon phases. Fig. (2) shows the characteristic spectra of amorphous-Si and poly-Si obtained in the Vertical Reactor in different process conditions. (500 mTorr; 660 °C and 50 sccm of SiH_4 in 100% Silane atmosphere for the amorphous film at bottom and 90 Torr, 740 °C; 50 sccm of SiH_4 and 25.300 sccm of Hydrogen for poly-Si film at top). The perturbation due to the amorphous phase observed in the Fig (2) indicates a presence of very small quantity of this material in the poly-Si deposited film. As the amorphous phase does not become electrically active (Seto, 1975; Lu, 1980; Lu, 1981; Joshi, 1984; Kamins, 1998), the amount of this phase should be kept at a allowable minimum level for MOS gate application, with crystallinity poly-Si film as close as of single-crystalline Silicon.

The films deposited in both diluted and non-diluted Silane Atmosphere in the Vertical Reactor presented a good quality poly-Si Raman spectrum for pressures above 1 Torr and Temperature above 650 °C. Fig (3) presents some obtained spectra of films deposited in different process conditions. In all the cases the perturbation due to amorphous phase is very small.

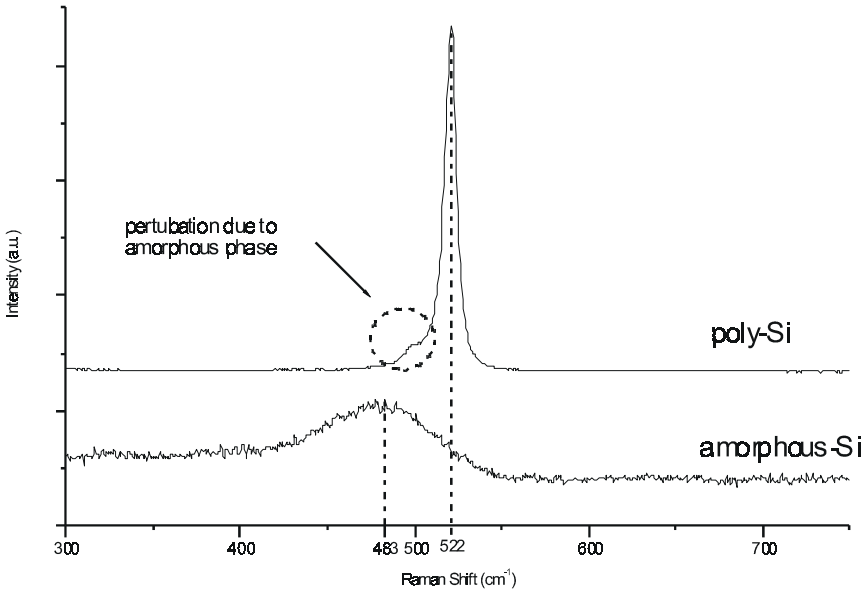

Figure2: Raman Spectrum of an amorphous Silicon film (bottom; P = 500 mTorr; T = 660 °C; Q SiH4 = 50 sccm) and polycrystalline Silicon film (top; P = 90 Torr, T = 740 °C; Q SiH4 = 50 sccm; QH2 = 25.300 sccm) deposited in the PMC 200 CVD Vertical Reactor.

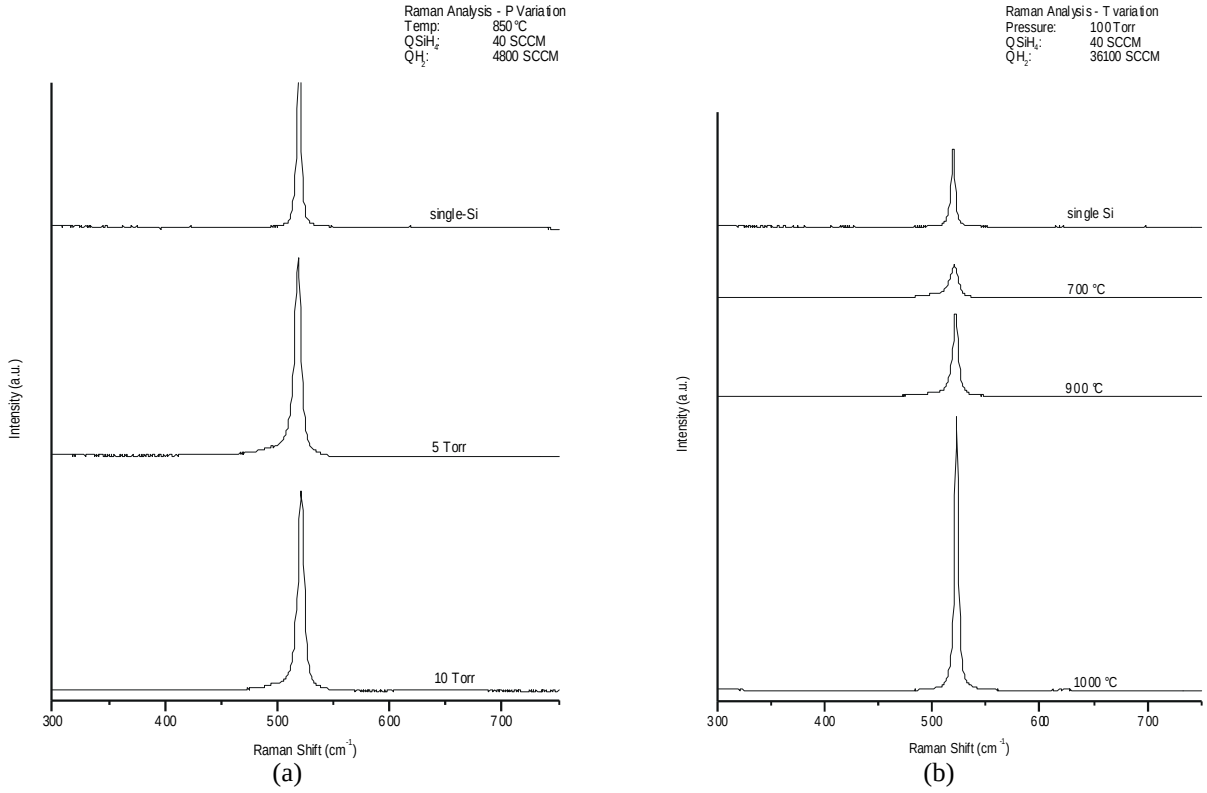

Figure3: Comparison of Raman Spectrum of films obtained in different LPCVD process conditions in the PMC 200 CVD Vertical Reactor. Intensity variation in (b) is due to the different crystalline characteristics of the films. In both figures, single-crystalline Silicon spectrum is presented as reference.

Maximum intensity variation in the Raman Spectrum observed in Fig. (3-b) is related to crystalline lattice perfection in the obtained films. Defects as displacements or twin grain will cause a less intense spectra. Stress and lattice disturbances like impurities can also broad spectrum. A very intense and wide peak or a narrow and large one is indicative of a film with low crystalline quality. Even amorphous sign is not seen in the two presented situations; these conditions indicate a bad quality film with high internal stress and/or grains with great amount of defects (displacements, stacking faults, etc.) respectively (Harbeke, 1983; Harbeke, 1984).

The quality of deposited films depends on several process parameters used for their deposition. According to Kamins (1997), it is largely influenced by the relationship between temperature and total pressure through equation (1):

$$L \approx \sqrt{Dt} \sim \frac{1}{\sqrt{R_D}} \exp\left(-\frac{E_a}{kT}\right) P^{-n} \tag{1}$$

Where L is the surface diffusion length; D is the surface diffusion coefficient; t the time available for diffusion; R_D is the deposition rate; E_a, is the activation energy for surface diffusion; k is Boltzman's constant; T, temperature; P, total pressure and n are positive and much less than unity. The surface diffusion length is the distance that an atom can diffuse on the surface of the substrate between the adsorption and the fixation in the crystal lattice.

From the equation (1) one can easily note that pressure and temperature have inverse effect on the surface diffusion length and that a great increase in Pressure can be compensated by a small increase of Temperature, because the exponential dependence of T. From Fig (3) we can note the difference in L dependence on Pressure (3-a) and Temperature (3-b) being this difference stronger in the last one. If L from eq. (1) is big (high value of T and/or low value of P) the formation of crystals will be improved by the surface diffusion, because the adsorbed atoms can diffuse at relatively long distances until finding an available surface site for incorporation in a crystalline nucleus. In opposite conditions it is not possible because the adsorbed atom doesn't have enough energy for diffusion or because new atoms are adsorbed over this one, hindering the migration and/or fixing it to the substrate as amorphous material.

3.2. X-Ray Diffraction (XRD)

The XRD measurements allow to analyze the texture of the deposited films, so to get informations about the structure of films, such as formed crystalline orientation, dominant crystalline directions of the growth, as well as their grain sizes. Fig. (4) shows XRD profile of the film obtained at pressure of 10 Torr, temperature of 770 °C, 40 sccm and 4800 sccm, respectively of SiH_4 and H_2 flow. All the poly-Si films deposited in the Vertical Reactor showed similar XRD profile, being the films constituted by crystalline structure orientation of <111>; <220> and <331> directions.

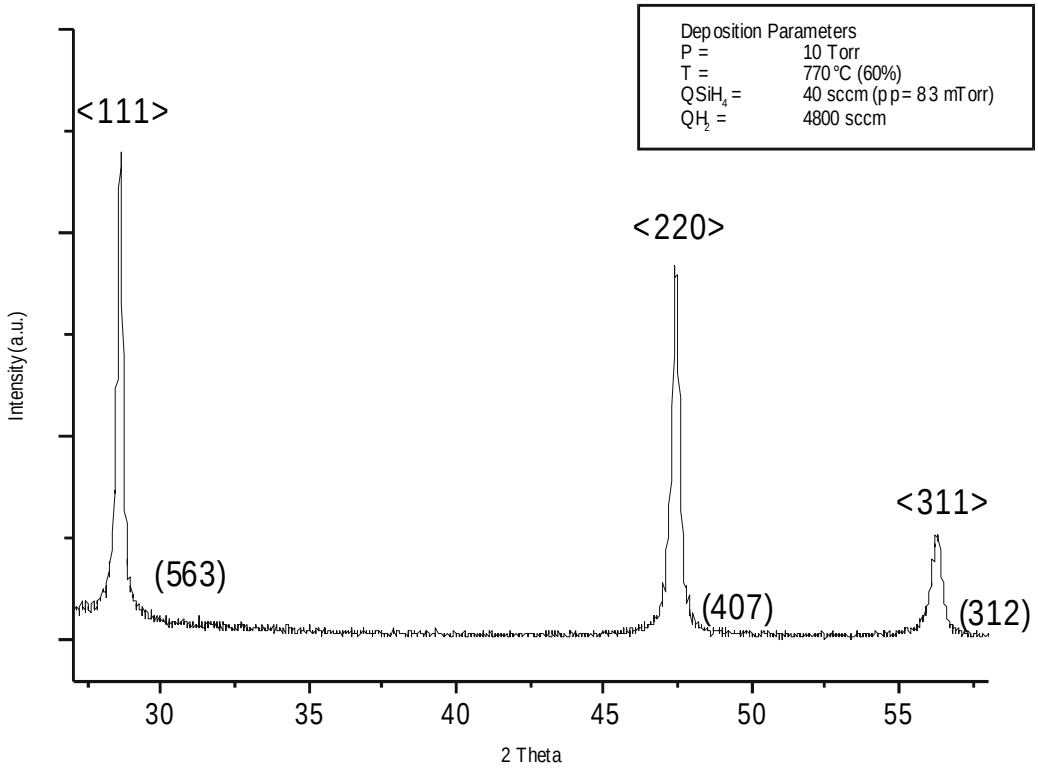

Figure 4: XRD profile of the sample obtained in the Vertical Reactor, at deposition conditions of P = 5 Torr; T = 800 °C; $QSiH_4$ = 40 sccm and QH_2 = 4800 sccm.

Grain size (D) presented in the fig. (4) beside the diffraction peaks, was calculated using Scherrer formula (Harbeke, 1984; Joubert, 1987) and it represents an average diameter in terms of grain volume in the limit of XRD depth analysis. At the deposition conditions of Fig. (4), grain size decreases from 563 nm for <111> to 312 nm for <311> crystalline directions. In tables (2) and (3) are presented values of D (Å) estimated for other films obtained in the Vertical Reactor using different deposition conditions. The results show that grain size is influenced by parameters

pressure and temperature, being more sensitive to the temperature variation. This effect can be explained as the result of the variation in the diffusion length, consequence of the changes in whole growth kinetics. The variation of one or more process parameters affects not only the grain size but also the relative intensity of the XRD spectrum. Since the grain size influences the electrical characteristics of the deposited film, the growth parameters need to be chosen carefully to produce films with appropriate morphology (Seto, 1975; Lu, 1980; Kamins, 1998).

Table2: Grain size and XRD diffraction intensity variation as a function of total pressure used in LPCVD deposition

Pressure (Torr)	QH_2 (SCCM)	$QSiH_4$ (SCCM)	Temperature (°C)	XRD (grain size in Å)					
				<111>	Int.	<220>	Int.	<311>	Int.
1,5	0	60	770	152	1	130	1	131	0,9
2,5				182	1	638	6,7	245	1,8
5	4800	40	800	290	1	216	0,9	212	1,4
10				536	1	407	2	312	1,2
5	4800	40	850	631	1	454	4,1	393	1,4
10				482	1	389	0,2	335	0,5

Table3: Grain size and XRD diffraction intensity variation as a function of temperature used in LPCVD deposition

Pressure (Torr)	QH_2 (SCCM)	$QSiH_4$ (SCCM)	Temperature (°C)	XRD (grain size in Å)					
				<111>	Int.	<220>	Int.	<311>	Int.
1,5	0	60	710	n/a	1	498	12,4	107	2,6
			770	152	1	130	1	131	0,9
5	4800	40	800	290	1	216	0,9	212	1,4
			850	631	1	454	4,1	353	1,4
10	4800	40	800	536	1	407	2	312	1,2
			850	719	1	735	0,2	574	0,5
100	36000	40	740	172	1	678	43,7	267	3,1
			900	732	1	974	0,2	503	0,4
			1000	1744	1	953	1,9	1765	0,4

XRD analysis still allows determining the dominant texture or preferred orientation (PO) of poly-Si thin films. PO determines the characteristics of the surface such as the rms roughness. The texture of the film influences, for instance, dopant diffusion, which is an anisotropic process (Kamins, 1998) as well as performance of devices like TFT's and piezoelectric sensors (Kakinuma, 1995). PO is obtained comparing the normalized intensities of the XRD spectrum with pre-defined values from a random oriented film (powder). Table (4) presents normalization factors for poly-Si (Kamins, 1978):

Table 4: Intensity normalization factors for the first three peaks of XRD spectrum for poly-Si

Orientation	Normalization Factor
<111>	1,00
<110>	0,37
<311>	0,18

In the Tables (2) and (3), columns denoted as “int” present the normalized relative intensity estimated according to the values in Tab. (4) for films deposited using different conditions.

As the results shown, PO of the deposited film has a complex dependence with pressure and temperature. While at lower pressures and temperatures the formation of the <110> texture is favored, at higher temperatures the <111> texture is more evident. This change of the PO with deposition parameters can be attributed to the variation of the microscopic geometry of the growing surface (Kakinuma 1995), therefore, to the variation of the number of bonds needed for the fixation of an atom in crystalline lattice (fig. 5). As illustrated in the Fig. (5), to the formation of the <110> structure, 2 atoms are necessary to became fixed, while for the <111> structure 3 atoms are necessary, which require more available energy (higher temperature) for continuous growth. Accordingly to Sze (1984), the number of available connections per cm^2 is 20% larger in <111> direction than in <110> direction, but this numeric superiority only implies in larger growth if there are enough conditions to take the advantage, which occurs only at relatively high temperatures.

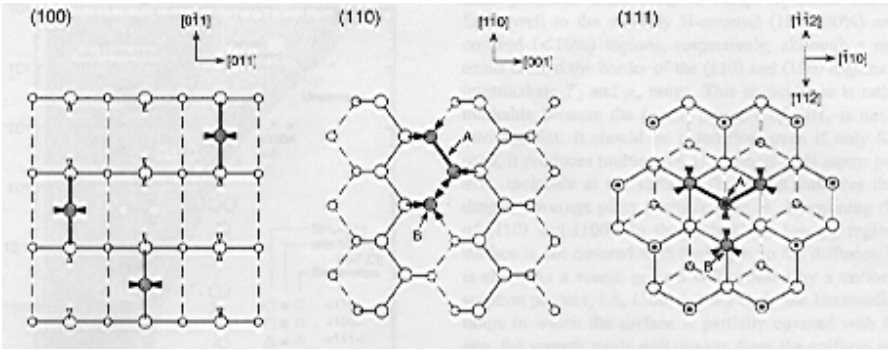

Figure5: Microscopic geometry of three low index surfaces of Silicon lattice (Diamond Structure). The smaller circles represent atoms in the inferior layers and the shadowed are adsorbed atoms. The letters A and B represent stable nuclei and adatoms to be incorporate to the nucleus, respectively. (Kakinuma, 1995)

3.3 Atomic Force Microscopy (AFM)

Surface analysis of samples was made by AFM in contact mode. Table (5) presents the rms roughness, in ascending order, measured over 5x5 μm^2 area in some of the deposited films. As can be observed from the table, the roughness is strongly influenced by the grain size (D) and the preferential orientation (PO) of the deposited film. The knowledge of this surface characteristic is an important factor for the necessary sub-sequent steps of the processes, such as growth of isolation and dielectric oxide layers.

Table 5: AFM Rms Roughness measured for deposited poly-Si films

Pressure (Torr)	QH_2 (SCCM)	$QSiH_4$ (SCCM)	Temperature (°C)	XRD (normalized intensities)			PO	D ave (Å)	Roug (nm)
				<111>	<220>	<311>			
100.000	36100	40	740	1	43,72	3,08	<110>	372,33	11,49
10.000	4800	40	800	1	2,07	1,22	<110>	418,33	37,51
10.000	4800	40	850	1	0,21	0,54	<111>	676,00	50,88
1.500	0	60	770	1	0,97	0,95	RAND	137,67	58,51
100.000	36100	40	1.000	1	1,93	0,43	<110>	1487,33	81,59

As one can see, roughness is strongly influenced by the average grain size (D) of deposited film. Larger grains become the surface of the film more roughly. As D tends to be larger at high temperatures and reduced pressures the roughness also follows this behavior (Kamins, 1998). For grains of relatively same size, the roughness increases in function of how random is the film (Tab. (5) - normalized intensities values closer the unit). From Fig. (5) ones can also notice that films with a strong <111> texture also present a larger roughness. Unlike other crystalline plans, a layer grown in <111> direction needs two atomic layers for growing. In the Fig. (5), the shadowed atom represented with darkened center is in a plan above the other shadowed ones, resulting in a larger height variation in relation to the base plan. The layers grown in <100> and <110> directions present a larger easiness for lateral growth, what implies in a more smooth film.

3.4 Resistivity

Sheet Resistivity (R_S) was measured in P doped implanted samples with doses of $1x10^{16}$ cm^{-2} and $2x10^{16}$ cm^{-2} and energy of 150 keV. Annealing of the films was carried out in a RTA process (960 °C, 40 seg) after RCA cleaning, in order to restore the damage caused to crystalline structure by ion implantation and to activate dopants. Sheet resistivity was calculated from V/I data measured by 4-point probe method. The resulted values are presented in Table (6).

Sheet resistivity values varied from 14 to 138 Ω/ and from 23 to 42 Ω/ for $1x10^{16}$ cm^{-2} and $2x10^{16}$ cm^{-2} doses respectively. With the exception of R_S value showed by one of the samples, all others characterized samples of poly-Si films deposited in the Vertical Reactor, exhibited sheet resistivity values that are within the 20–50 Ω/ , considered acceptable for applications in microelectronic devices. The variations verified in the resistivity value presented in Tab. (6) are related to the differences in deposition parameters used for the obtention of the films. The quality of the deposited layer and the annealing temperature affect the electrical resistivity of the poly-Si films. Annealing temperature influences the final morphology, such as crystallinity, crystal texture, and surface roughness of the layer. Accordingly to our measurement data presented in Tab. (6), films of similar grain size resulted in close resistivity values. If the grain size is larger, the sheet resistivity decreases and if the grain size is small, the resistivity increases. Thus, the electrical resistivity R_S variates inversely with grain size. The same trend was verified by Ibok (1993) in his studies of $POCl_3$ diffusion doped poly-Si samples. Moreover, the amount of amorphous material also affects R_S (Kamins, 1998; Seto, 1975). A high resistivity value verified in films of smaller grains sizes can be due to a larger

amount of amorphous phase present within the grain boundaries. The amorphous materials contain great number of incomplete bonds which links to dopant impurities in a non-substitutional position, creating intermediary states in the band gap capable to trap free carriers, besides forming a potential barrier to the carriers flow from a grain to another, hindering the formation of electric current. So, as small as is the crystalline area (smaller grains), higher are the electrical sheet resistivity values, because of the presence of the larger amount of amorphous material in the films. Due to these complexity of poly-Si films, resistivity values much larger than that of single-crystalline Silicon at low and moderate dopant concentrations ($<10^{18}$ cm^{-3}), has been verified by several authors (Lu, 1980; Joshi, 1984; Kamins, 1998). Moreover, the dopant segregation through the amorphous area in the grain boundaries and outdiffusion phenomena that reduces the amount of dopants, affect the sheet resistivity of the poly-Si films (Chow, 1985; Powell, 1985; Kamins, 1998).

Table 6: Sheet resistivity for P doped poly-Si.

Dose (cm^{-2})	Pressure (Torr)	Temperature (°C)	$QsiH_4$ (SCCM)	QH_2 (SCCM)	D ave (Å)	V/I (Ω)	R_S (Ω/)
$2x10^{16}$	2,5	710	60	0	/	9,41	42,63
	10	850	40	4800	676	5,24	23,74
	90	740	50	25300	647	5,20	23,56
$1x10^{16}$	100	740	40	36000	372	30,60	138,62
	100	900	40	22500	663	5,89	26,68
	100	1000	40	36000	1487	3,17	14,36
Ibok (1993) [10^{20} – 10^{21} cm^{-3}] $POCl_3$ diffusion doping (900°C; 25 min)							100-500

4. Conclusions

An old epitaxial CVD vertical reactor was re-built and modified to operate in low pressure conditions in order to be able to deposit poly-Si films, and was successfully implemented at the Center for Semiconductor Components at the State University of Campinas. Intensive deposition experiments were carried out in this reactor, in a wide range of operation parameters. The obtained results show that this vertical type CVD reactor allow us to fabricate poly-Si films of the quality desired for application in devices. Several deposited films were characterized by Raman Spectroscopy, Atomic Force Microscopy, X-Ray Diffraction, and V-I measurements. The characterization techniques allowed a good study of morphological and electrical characteristics of deposited films, and to correlate them to the used deposition parameters (P, T, $QSiH_4$ and QH_2). In the range of deposition parameters used in this work, all the deposited films were fully crystalline with a well defined texture, and of relatively small grain size. Lower pressures and temperatures favored the formation of the <110> texture, while at higher temperatures the <111> texture was dominant. The total pressure and the temperature are the main parameters that influence the growing layer and the surface roughness, related to the texture and grain size of the deposited film. The sheet resistivity measured in some P-doped implanted poly-Si films, varied from 14 to 138 Ω/ and from 23 to 42 Ω/ for $1x10^{16}$ cm^{-2} and $2x10^{16}$ cm^{-2} doses respectively. These resistivity values are almost all of them within 20–50 Ω/ , considered acceptable for applications in microelectronic devices. The displayed morphological and electrical characteristics assure that the deposited films are of quality, as good as most of the poly-Si films presented in the literature.

5. Acknowledgments

This work was partially supported by the UNICAMP, FAPESP, CAPES and CNPq.

The authors would like to thank José Godoy F° of the CCS-UNICAMP for his professional support and help in this work; Dailto Silva of the IG for Raman Spectroscopy measurement; Prof. Dr. Lisandro P. Cardoso of the IFGW-UNICAMP for X-Ray diffraction measurements and Profª. Dra. Mônica A. Cotta of the IFGW-UNICAMP for Atomic Force Microscopy measurements.

6. References

Chow, R.; Powell, R. A.; 1985, "Activation and Redistribution of Implanted P and B in Polycrystalline Si by Rapid Thermal Processing" J. Vac. Sci. Technol. A Vol. 3 No 3, pp. 892-895

Ferreira, E. C.; 1984, "Obtenção e Caracterização de Filmes de Silício Policristalino para Aplicação em Tecnologia MOS Porta de Silício"; Tese de Mestrado; Unicamp

Harbeke, G.; Krausbauer, L.; Steigmeier, E. F.; Widmer, A. E.; Kappert, H. F.; Neugebauer, G.; 1983, "High Quality Polysilicon by Amorphous Low Pressure Chemical Vapor Deposition"; Appl. Phys. Lett., Vol. 42 No 3, pp. 249-251

Harbeke, G.; Krausbauer, L.; Steigmeier, E. F.; Widmer, A. E.; Kappert, H. F.; Neugebauer, G.; 1984, "Growth and Physical Properties of LPCVD Polycrystalline Silicon Films"; J. Electrochem. Soc., Vol. 131 No 3, pp. 675-682

Ibok, E.; Garg, S.; 1993, "A Characterization of the Effect of Deposition Temperature on Polysilicon Properties – Morphology, Dopability, Etchability and Polycide Properties"; J. Electrochem. Soc., Vol. 140 No 10, pp. 2927-2937

Joshi, D. P.; Srivastava, R. S.; 1984, “A Model of Electrical Conduction in Polycrystalline Silicon”; IEEE Trans. Elect. Dev.; ED-31 No 7, pp. 920-927

Joubert, P.; Loisel, B.; Chouan, Y.; Haji, L.; 1987, “The Effect of Low Pressure on the Structure of LPCVD Polycrystalline Silicon Films”; J. Electrochem. Soc. Vol. 134 No 10, pp. 2541-2545

Kakinuma, H; 1995, “Comprehensive Interpretation of the Preferred Orientation of Vapor Phase Grown Polycrystalline Silicon Films”; J. Vac. Sci. Technol. A; Vol. 13, No 5, pp. 2310-2317

Kamins, T. I.; Mandurah, M. M.; Saraswat, K. C.; 1978, “Structure and Stability of Low Pressure Chemically Vapor Deposited Silicon Films”; J. Electrochem. Soc.; Vol. 125, No 6, pp. 927-932

Kamins, T. I.; Fischer-Colbrie, A.; 1997, “Effect of Total Deposition Pressure on the Structure of Polycrystalline Silicon Films”; Appl. Phys. Lett.; Vol. 71 No 16, pp. 2322-2324

Kamins, T. I.; 1998, “Polycrystalline Silicon for Integrated Circuit and Displays”; Kluwer Academic Publishers, 2ª edition,

Lu, N. C. C.; Gerzberg, L.; Meindl, J. D.; 1980, “A Quantitative Model of the Effect of Grain Size on the Resistivity of Polycrystalline Silicon Resistors”; IEEE Trans. Elect. Dev. Lett.; Vol. EDL-1 No 3, pp. 38-41

Lu, N. C. C.; Gerzberg, L.; Lu, C.; Meindl, J. D.; 1981, “A New Conduction Model for Polycrystalline Silicon Films”; IEEE Trans. Elect. Dev.Lett.; Vol. EDL-2, No 4, pp. 95-98

Powell, R. A.; Chow, R.; 1985, “Dopant Activation and Redistribution in As^+-Implanted Polycrystalline Si by Rapid Thermal Processing” J. Electrochem. Soc. Vol. 132, No 1, pp. 194-198

Seto, J. Y. W.; 1975, “The Electrical Properties of Polycrystalline Silicon Films”; J. Appl. Phys.; Vol. 46, No 12, pp. 5247-5254

Sze, M. S.; 1984 “VLSI Technology”; McGraw-Hill Book Co.

XVI CONGRESSO BRASILEIRO DE ENGENHARIA MECÂNICA
16th BRAZILIAN CONGRESS OF MECHANICAL ENGINEERING

Determinação da Razão entre as taxas R{411} e R{100} para Compensação de Cantos Convexos em Corrosão de Silício com KOH

Pedro Ricardo Barbaroto
Universidade Estadual de Campinas - FEEC/CCS - C.P. 6061, CEP 13083-970, Campinas, SP, Brazil
barbarot@lnls.br

Luiz Otávio Saraiva Ferreira
Laboratório Nacional de Luz Síncrotron - MIC - C.P. 6192, CEP 13084 –971, Campinas, SP, Brazil
lotavio@lnls.br

Ioshiaki Doi
Universidade Estadual de Campinas - FEEC
doi@led.unicamp.br

Jacobus W. Swart
Universidade Estadual de Campinas - CCS
jacobus@led.unicamp.br

Resumo. *É apresentado um método simplificado de determinação da razão entre as taxas de corrosão R{411} e R{100} para silício (100) em solução aquosa de KOH. Foram estabelecidas as relações geométricas que possibilitam a determinação de R{411} / R{100} a partir de um canto convexo alinhado com os planos {110}. Após 100 minutos de corrosão de um substrato de silício em KOH a 40% foi medida uma razão R{411} / R{100} igual a 1,6.*

Palavras chave: *Corrosão de Silício, Compensação de Cantos, Taxas de Corrosão, Microfabricação, "Bulk Silicon Micromachining".*

1. Introdução

A corrosão anisotrópica de silício em solução aquosa de KOH é o método mais utilizado de microusinagem de substratos de silício monocristalino, técnica também conhecida como "Bulk Silicon Micromachining" (Petersen, 1982).

As estruturas tridimensionais resultantes são definidas pela geometria das janelas da máscara de corrosão, que é um filme resistente ao ataque por KOH, depositado ou crescido no substrato de silício.

Alinhando-se as janelas de corrosão com os planos {110}, obtém-se estruturas delimitadas pelos planos {111} do cristal. Porém nos cantos convexos, definidos pelo encontro de dois planos {111}, ocorre uma deformação da geometria devido à exposição de outros planos cristalinos à corrosão, fenômeno esse denominado "erosão de cantos" (Bean, 1978).

A erosão de cantos pode ser evitada ou minimizada pela adição de estruturas compensadoras à geometria das janelas de corrosão (Mayer et al., 1990; Offereins et al., 1992), cujo dimensionamento exige o conhecimento da razão entre as taxas de corrosão dos planos {411} e {100} (Mayer et al., 1990; Offereins et al., 1992).

A motivação deste trabalho foi obter-se experimentalmente a razão R{411} / R{100}, necessária à microfabricação de estruturas mecânicas de silício monocristalino com geometrias precisamente definidas (Ferreira et al., 1998), sem precisar recorrer aos complexos métodos de determinação das taxas de corrosão apresentados na literatura (Offereins et al., 1992).

2. Teoria

Dado um substrato de silício (100) no qual há um canto convexo alinhado com os planos {110}, seu formato é definido pela taxa de corrosão dos planos {411}, conforme mostrado na Figura 1, onde as linhas tracejadas são a interseção das frentes de corrosão com a superfície do silício. O ângulo entre as frentes de corrosão (planos {411}) e os planos normais à superfície que passam nas linhas tracejadas (planos {410}) é $\alpha = 14{,}04°$.

Portanto, a taxa de corrosão R{411} projetada nos planos {410} nos dá a velocidade de avanço das linhas tracejadas. Seja **a** o avanço das frentes de corrosão na direção <410>. Então a projeção em <410> do avanço da frente de corrosão na direção <411> é dado pela eq. 1. Seja **b** o avanço da frente de corrosão na direção <110>. A projeção em <110> do avanço da frente de corrosão na direção <411> é dado pela eq. 2. Substituindo-se (3) em (2) e o resultado em (1) tem-se (4), que é a velocidade de corrosão na direção <110>.

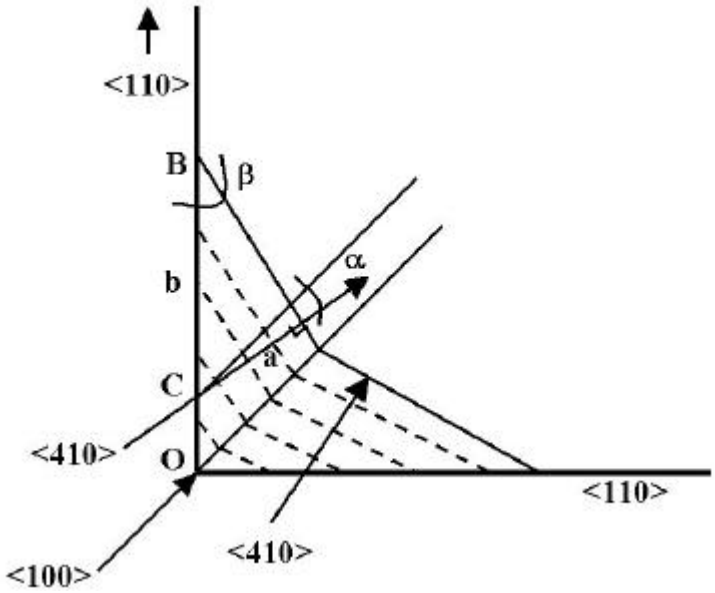

Figura 1: Frentes de Corrosão.

$$R\{410\}_{R\{411\}} = \frac{da}{dt} = \frac{R\{411\}}{\cos a} \tag{1}$$

$$R\{110\}_{R\{411\}} = \frac{db}{dt} \tag{2}$$

$$b = \frac{a}{\text{sen } b} \qquad b = 30{,}96° \tag{3}$$

$$\frac{db}{dt} = \frac{1}{\text{sen } b} \cdot \frac{da}{dt} = \frac{R\{411\}}{\text{sen} b \cos a} \cong 2 \cdot R\{411\} \tag{4}$$

Dados uma taxa de corrosão R{411} constante e um tempo de corrosão T_1, o avanço da frente de corrosão desde o canto inicial "O" ao longo da direção <110> é dado por:

$$OB = 2 \cdot R\{411\} \cdot T_1 \tag{5}$$

Portanto, conhecendo-se a distância OB e o tempo de corrosão T_1, a taxa R{411} é dada por:

$$R\{411\} = \frac{OB}{2T_1} \tag{6}$$

A taxa de corrosão R{100} é determinada medindo-se a profundidade H de corrosão no mesmo tempo T_1:

$$R\{100\} = \frac{H}{T_1} \tag{7}$$

Finalmente, a desejada razão entre as taxas de corrosão é dada por:

$$\frac{R\{411\}}{R\{100\}} = \frac{OB}{2H} \tag{8}$$

Que pode então ser determinada experimentalmente a partir da medida da erosão de um canto convexo e da profundidade da corrosão.

3. Experimental

O método foi aplicado a um substrato de silício (100) com máscara de corrosão de SiO_2, na qual foram fotogravadas janelas de corrosão com cantos convexos alinhados aos planos {110}. O substrato foi corroído em solução aquosa de KOH a 40% em massa durante 100 minutos, à temperatura de 80° C. A profundidade H da corrosão foi medida com um perfilômetro, e a distância OB foi medida com um microscópio óptico.

4. Resultados

A Figura 2 mostra um canto convexo corroído, a partir do qual mediu-se a distância OB=368 μm e a profundidade de corrosão H=115,8 μm.

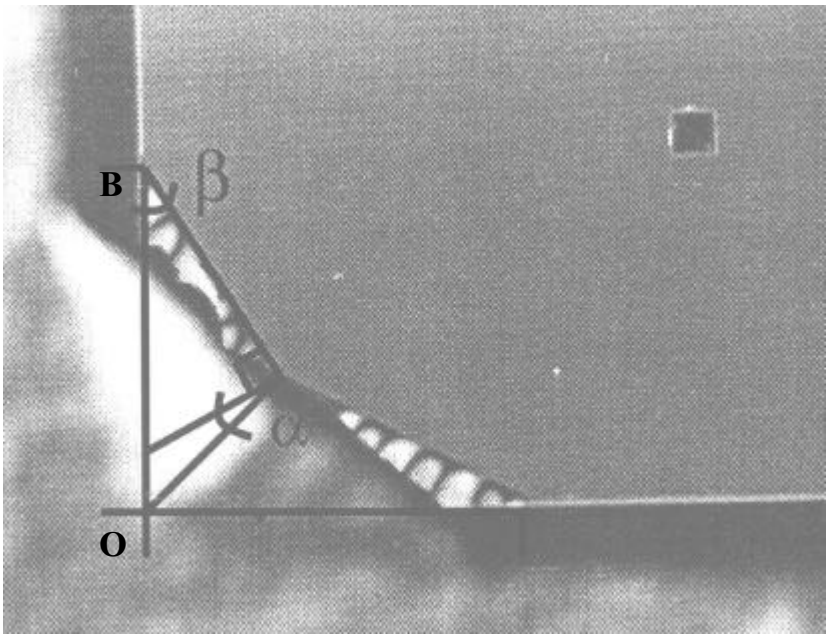

Figura 2: Canto Convexo corroído utilizado no experimento.

A partir dos valores medidos e da equação (8) calculou-se:

$$\frac{R\{411\}}{R\{100\}} = \frac{OB}{2H} \cong 1{,}6$$

5. Discussão

O método proposto requer condições de corrosão bem controladas e estáveis, que garantam uma taxa de corrosão constante, e duas medidas de comprimento: a distância OB e a profundidade H da corrosão.

A medida da distância OB foi realizada com um microscópio óptico provido de padrão de calibração, o que garantiu precisão melhor que 1%, e a medida da profundidade H da corrosão foi realizada com um perfilômetro, com precisão também melhor que 1%.

A temperatura da solução foi mantida entre 79 e 81ºC. Embora trabalhos anteriores (Mayer et al., 1990; Offereins et al., 1992) digam que a razão R{411} / R{100} não depende da temperatura entre 60 e 100°C, não se pode descartar totalmente sua influência nos resultados. A concentração da solução foi estabelecida pela massa de KOH e de H_2O, não se considerando o conteúdo de umidade do KOH, que pode chegar a 10%, o que implica em imprecisão da concentração obtida.

A razão R{411} / R{100} encontrada para 40% de KOH foi igual a 1,6, contra 1,5 (Enoksson, 1997) e 1,35 (Mayer et al., 1990; Offereins et al., 1992). Essa diferença poderia ser explicada tanto pelo conteúdo de umidade do KOH usado pelos diversos autores quanto pela variação de concentração durante o processo, causada tanto pela evaporação de H_2O quanto pelo consumo de KOH na reação com Si. A titulação da solução antes e depois do processo poderia fornecer elementos para esclarecer essa questão.

6. Conclusão

Foi desenvolvido e testado um método simplificado de determinação de R{411} / R{100}. O resultado obtido é coerente com os de outros autores, mas indica a necessidade de repetição do experimento para diversas outras concentrações de KOH, e o controle mais rígido da composição e da temperatura da solução.

7. Referências

Bean, K. E., 1978, "Anisotropic Etching of Silicon", IEEE Transactions on Electron Devices, Vol. ED-25, No. 10, pp. 1185-1193.

Enoksson, P., 1997, "New Structure for Corner Compensation in Anisotropic KOH Etching", J. Micromech. Microeng.,7, pp. 141-144.

Ferreira, L. O. S., Pourlborz, F., Ashar, P., Khan-Malek, C.,1998, "Torsional Scanning Mirrors Actuated by Electromagnetic Induction and Acoustic Waves", ICMP, pp. 155-162.

Mayer, G. K., Offereins, H. L., Sandmaier, H., Kühl, K., 1990, "Fabrication of Non-Underetched Convex Corners in Anisotropic Etching of (100)-Silicon in Aqueous KOH with Respect to Novel Micromechanic Elements", J. Electrochem. Soc., Vol. 137, No. 12, pp. 3947-3951.

Offereins, H. L., Sandmaier, H., Marusczyk, K., Kühl, K., Plettner, A., 1992, "Compensating Corner Undercutting of (100) Silicon in KOH", Sensors and Materials, 3, 3, pp. 127-144.

Petersen, K. E.,1982, "Silicon as a Mechanical Material", Proceedings of the IEEE, Vol. 70, No. 5, pp. 420-457.

Determination of the Ratio between the rates R{411} and R{100} for Convex Corners Compensation in KOH Silicon Etch

Barbaroto, P. R.
State University of Campinas, FEEC/CCS - C.P. 6061, CEP 13083-970, Campinas, SP, Brazil
barbarot@lnls.br

Ferreira, L. 0. S.
National Laboratory of Syncrotron Light, MIC – C.P. 6192, CEP 13084 –971, Campinas, SP, Brazil
lotavio@lnls.br

Doi, I.
State University of Campinas, Brazil, FEEC/CCS
doi@led.unicamp.br

Swart, J. W.
State University of Campinas, Brazil, FEEC/CCS
jacobus@led.unicamp.br

Abstract. *A simplified method for determination of the ratio between the rates R{411} and R{100} for (100) Si in aqueous KOH solution is presented. The geometric relations between R{411} / R{100} and the shape of convex corners aligned to {110} was derived and applied to a sample etched in 40% aqueous KOH for 100 minutes, resulting on R{411} / R{100} equal to 1.6.*

Keywords. *Silicon Etch, Corner Compensation, Etch Rates, Bulk Silicon Micromachining, Microfabrication.*

XVI CONGRESSO BRASILEIRO DE ENGENHARIA MECÂNICA
16th BRAZILIAN CONGRESS OF MECHANICAL ENGINEERING

SU-8 PHOTORESIT AS A COST REDUCING FACTOR IN LIGA-X TECHNOLOGY

Izaque A. Maia
National Synchrotron Light Laboratory – Microfabrication Laboratory/MIC
Caixa Postal 6192 CEP 13084 -971 Campinas – SP - Brazil izaque@lnls.br

Luiz O. S. Ferreira
Idem lotavio@lnls.br

Maria Helena O. Piazzetta
Idem nena@lnls.br

Graziele C. Natal
Idem graziele@lnls.br

Abstract In the present work it is demonstrated that the high sensitivity of SU-8, a commercial negative tone photoresist, allows lithography of 125 μm thick SU-8 layers using home made thick silicon membrane masks and synchrotron source without insertion devices to increase the photon flux of high energy X-rays. Moreover the exposure time for complete sensitization of bottom layer takes up to 4 minutes for an average 100 mA ring current. This means a significant cost reduction of LIGA-X when SU-8 replaces the mostly used polimetilmetacrylate (PMMA) photoresist. The exposures were carried out in the storage ring of the Brazilian Synchrotron Light Laboratory (LNLS). The fabrication steps of X-ray mask with silicon membrane are shown.

Key words: X-ray mask, SU-8 , MEMS, lithography, LIGA

1. Introduction

The LIGA (the German initials for Lithography, Electroplating and Molding) technology (Barcher et all, 1995; Ehrfeld et all, 1998; Guckel, 1998; Kupla et all, 2000; Madou, 1997; Peckerar, 1993; Tolfree., 1998) allows the batch production of high-aspect-ratio microstructures from metals, polymers and ceramics. It was first developed at Karlsruhe Nuclear Research Center in Germany in the late 1970s and is based on the production of polymeric molds with sub-micron precision by deep X-ray lithography (Cerrina, 1997). These molds are the starting point for production of high-aspect-ratio microstructures from metals, polymers and ceramics. Metallic microstructures like gears, turbines, filters, springs and molds for injection molding or for hot embossing are electroplated in the primary polymer molds produced by lithography. The more usual electroplated metals are Ni, Cu, Cr, Au and Ni-Fe alloys. The metallic molds are used to produce polymeric microstructures. The typical lateral dimensions of the microstructures are between a few microns and a few millimeters. Their typical thickness is below 500μm, and the lithography process precision is better than one micron. Filling the polymer molds with ceramic slurry, ceramic microstructures are produced by conventional drying and firing process steps of the lost mold method.

PMMA (polymethylmetacrylate) is the most used photoresist for deep X-ray lithography (Tolfree, 1998; El Kholi 1999). Usually it is exposed to photons in the 2-7keV range, presenting good contrast and surface finishing (less than 30nm roughness), but demands very high radiation dose and therefore exposure time to be sensitized (bottom dose higher than 2kJ/cm^3) using a synchrotron X-ray source like that of the LNLS (Laboratório Nacional de Luz Síncrotron), which operates at 1.37GeV/100mA. An alternative approach for reducing the exposure time and also to carry out lithography on thick PMMA layers would require equipping the LNLS synchrotron source with expensive insertion devices to give higher flux of higher energy X-rays. On the other hand replacing the PMMA for a more sensitive resist as SU-8 could be an affordable alternative for mold production and LIGA technology as a whole. SU-8, an epoxy based, negative tone, amplified photoresist, tailored to deep UV lithography, was announced late on 1996 (Despont et all, 1997). Thanks to its exceptional transparency to UV, it allows more than 1mm thick films to be exposed on conventional mask aligners, but the border diffraction effect results on non-vertical sidewall microstructures. This material presents also good mechanical (Lorenz et all, 1998) and chemical (Lee, 1995) stability. It was demonstrated for deep X-ray lithography (Malek, 1998) in the up to 7keV photon energy range.

In a previous work (Ferreira, 1999) good quality lithography of 125 μm thick SU-8 layers were obtained in only 60 seconds of exposure in the LNLS X-ray Instrumental Line (XRI) using a filtering set which consisted of kapton and aluminum films. The dose to sensitize SU-8 was 33 times lower than that required to sensitize the same thickness of PMMA. Moreover power spectrum simulations revealed that a 50μm silicon membrane alone, used as mask blank, would be equivalent to this kapton/aluminium filtering system. As PMMA requires masks having much thinner silicon blanks (2-3μm) this result is another advantage of SU-8 on PMMA. Thick silicon membrane masks are more robust, easy to fabricate and handle. The three advantages of SU-8 on PMMA, namely, thick silicon membrane masks, shorter exposure time and synchrotron sources without insertion devices have triggered the present work which deals with deep x-ray lithography of SU-8 photoresist using home made masks having thick silicon membranes and the current configuration of the LNLS synchrotron light source.

2. Experimental

2.1 Simulation

Simulations of power spectra were performed using the PC-Transmit software for the following filters: (a) 125 μm thick beryllium vacuum window only; (b) plus the aluminum (37.5 μm) /kapton (300 μm) filtering system or (c) plus the 50 μm thick silicon membrane.

2.2 The x-ray beam line

The LNLS 1.37GeV/100mA/λ_c=6Å electron storage ring was the X-ray source used for deep lithography of SU-8. The X-ray beam has 10mrad of horizontal divergence and 0.3mrad of vertical divergence, producing a 100mm wide, 3mm-height beam shape after passing through a 10m long beam line and reach the sample which is scanned vertically in front of the beam in a chosen velocity. The scanner is a stainless steel movable platform on which the mask/sample holder is screwed. The holder consists of two parallel stainless steel plates where the mask and sample, having a spacer in between, are pressed together with screws. A hole in one of these plates allows the X-ray beam to reach the mask.

2.3 Fabrication of the thick silicon membrane masks

The gold absorbers were electroformed in one face of the silicon plate before thinning the opposite side to form the blank. The electroforming molds were made of either negative (SU-8 100, Microchem Corp.) or positive (AZ4620, AZ Company) photoresist on a metallic base using two optical masks having different patterns. Each pattern consisted of a mosaic of small patterns which correspond to individual projects of microfabrication within the MUSA multi user project. The metal bases, consisting of Ti or NiCr bond layers and gold seed layer, were sputtered on silicon and the gold electroforming was performed with Auruna 515 gold bath (Degussa Galvanotechnik GmbH). Silicon wafers were thinned from 220 μm thickness to form membranes (approximately 35μm and 50μm thick) with KOH water solution (30% weight, 93 ^{o}C). The masks were either glued or sellotaped on a 3mm thick aluminum ring for safe handling.

2.4 Sample preparation, exposure and development

Samples were prepared by spinning SU-8 100 (MicroChem Inc) for 30 sec. at 2000 rpm, whereupon 125μm thick layers, on plain (111) silicon wafers. They were all prebaked at 95 ^{o}C (15 min.) and 75 ^{o}C (3 min.) and postbaked at 90 ^{o}C (20 min.). All exposures were carried out in a 9x10^{-4} mbar air atmosphere. The dose value of the first sample was chosen arbitrarily and the dose values of the remaining samples were chosen, greater or lower, according to the relative overall appearance of the samples shown in an optical microscope after the development step. The sample with best appearance had the following characteristics: (a) all structures attached to the substrate, meaning that enough dose reached the bottom of SU-8 layer, in all areas right below the transparent regions of the mask; (b) complete removal of the unexposed resist; (c) well defined structures and (d) minimum amount of defects which are presented and discussed below. Mask/sample gaps of 500 μm and 3000 μm were utilized. Photoresist developments were performed with commercial developer (Microchem Inc.) at room temperature under vigorous magnetic stirring for 3 to 5 minutes. Then the samples were washed with isopropanol alcohol and dried with gentle nitrogen blows before inspection using an optical microscope. This sequence was repeated till no significant changes was observed.

The doses values of this work are given in mAxmin units which are directly read from the PC program which controls the exposure dose.

3. Results

3.1 Power spectrum simulation

Power spectrum simulations Fig. (1) show that a 50 μm thick silicon membrane is nearly equivalent to the kapton/aluminum filtering system which was successfully used to sensitize a 125 μm thick SU-8 layer.

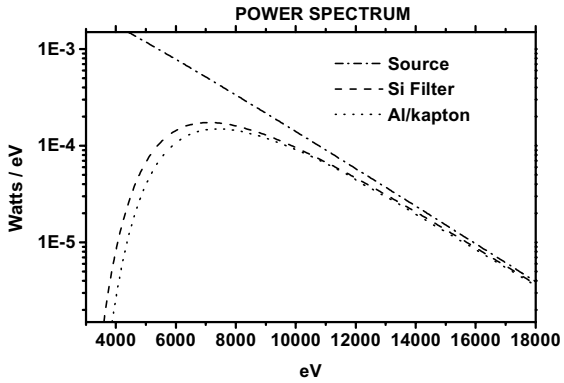

Figure 1: Simulations of power spectra related to the following filters: (a) 125 μm thick beryllium vacuum window only; (b) plus the aluminum (37.5 μm) /kapton (300 μm) filtering system or (c) plus the 50 μm silicon membrane.

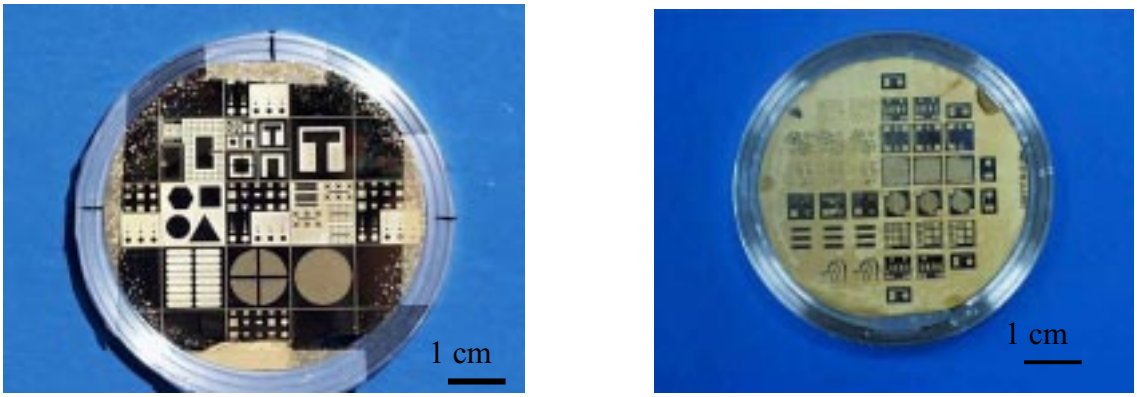

Figure 2. Mask 1 (left) and Mask 2 (right). The patterned area occupies the whole area of 2'' (100) silicon wafer

3.2 Mask Fabrication

Metallic layers were deposited on the whole area of 2"diameter (100) silicon wafers, Tab (1). Irrespective of the thickness of both, the vacuum deposited and electroplated layers, the silicon membranes did not cleave under the turbulence caused by the vigorous bubbling of the KOH etch at 93 ^{o}C. The absorbers in the mask border were 1 to 2 μm thicker than in the center. Thickness variations of the blank, up to ± 4 μm, were not confined to specific regions of the substrate and were distributed in a patchy manner. The AZ 4620 photoresist presented less resistance than SU-8 against the electroforming cyanide bath and as result the structures were not well defined. Severe bowing was exhibited by M3 and M4 masks. The gold thin film of the mask M1 was underetched on the borders by the KOH etching but the damage did not reached the structures of the inner regions. Mask M1 and M2, Fig. (2), were those chosen for the X-ray lithographic experiments. Bond and seed layers were not removed.

3.3 Exposition and Development

All samples where SU-8 was deposited presented cracks Fig. (3a) irrespective of dose values, mask patterns and mask/sample gap. Less rough surfaces were found in samples whose distance from the mask was 3000 μm rather than 500 μm. Three types of defects came out due to high doses, namely, the black stripe, Fig. (3b), SU-8 top layer, Fig. (3c), and, finally, bottom stain. Black stripes arouse in the pattern borders and has been accounted to tilted walls that deviates the light from the microscope objective. The bottom stains came out in areas where unexposed SU-8 was removed by the developer. A diagram associating the radiation dose range in which the above mentioned defects came out is given in figure 4. Dark spots and white spots were found in the M2 mask, and their associated samples. The positions of the dark spots match the positions of the white spots therefore it can be inferred that the dark spots are images of the white spots.

Table 1- Data of each step of fabrication of the absorber (deposition of thin metallic films, optical lithography and gold electroforming) and blank (KOH etching)

Mask	**Absorber**						**Blank**
	thin films deposition	lithography		gold electroforming			KOH etching
	Bond / Seed layers (/) Å	Patterns (fig. 2)	Resist type	Area (mm^2)	Center thickness (μm)	border thickness (μm)	Membrane thickness (μm± 4)
M1 #1	NiCr/Au (422/ 1419)	Mask 1	AZ 4620	471	4.4	4.0 – 6.0	35
M2 #1	Ti/Au (278 / 2119)	Mask 2	AZ 4620	1879	5.4	6.2-6.9	54
M3	Ti/Au (278 / 2119)	Mask 2	AZ 4620	1879	5.30	7.5-8.1	54 #3
M4	SiO_2/Cr/Au (-) #2	Mask 2	SU8	146	4.8	5.3-7.9	45 #3
M5	Ti/Au (278 / 2119)	Mask 2	SU8	146	9.1	9.40—10.0	225 #4
#1 Used in X-ray lithography #2 thermal evaporation #3 bowing #4 not etched							

4. Discussion

Gold electroforming followed by KOH silicon etch are techniques suitable to fabricate deep x-ray lithographic masks. As these masks have a 2" diameter silicon membrane (35 and 50 μm thick), without any supporting structure an appropriate ratio between the absorber and blank thickness must be achieved to avoid bowing. Another alternative to avoid bowing could be decreasing the absorber area.

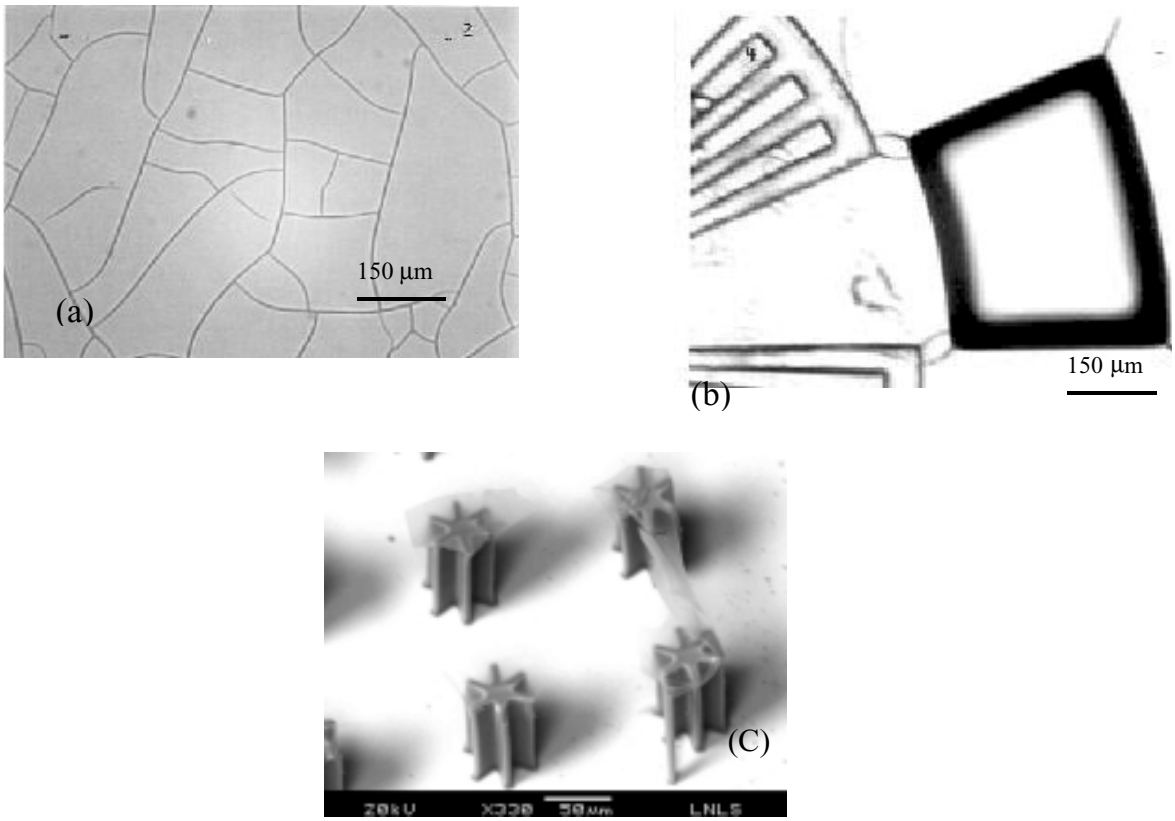

Figure 3 - Defects of SU-8 structures due to high X-ray doses: cracks (a), black stripe (b), top SU-8 layer (c). (a) and (b) are images from optical microscope and (c) are SEM images

The black spots on the SU-8 structures derives from the white spots of the mask. Their round shapes and their random size and space distribution all over the samples suggest that they arise from particle contamination on the mask. These particles would work as insulator spots which do not allow an effective gold electroforming whereupon small windows in the absorbers (the white spots) trough which the X-rays reach the sample giving as result the dark spots. It is intriguing the fact that black spots rather than SU-8 columns result from these undesirable windows in the absorber. It appears as if the white spots work as tiny filters that leave to pass only radiation that not sensitize SU-8 but promote photoreaction on the SU-8/silicon interface only. The black color of the black spots arises from scattering of visible light by a great number of tiny SU-8 structures which are probably the image of tiny structures present in the white spots of the absorber.

Black stripe defect is possibly the image of a tilted wall seen in an optical microscope without a deep focus depth as the one used here. It appears only when the samples are exposed to high doses. Such high doses would prompt the reproduction of tilted walls of the absorber on the SU-8 layer. Tilted wall on the absorber could be created by underetch or mass transport phenomena in the wet steps of mask fabrication, namely, photoresist development and gold electroforming bath.

Stains result probably from the secondary radiation on the substrate which sensitize a thin layer of SU-8 on the SU-8/substrate interface at high energy doses. Their patchy distribution on the surface sample associated to their systematic appearance under specific regions of the dark area of the mask suggests some correlation between the secondary radiation and the distribution of the absorber on the blank surface. Even in the cases where the bottom dose was so small that the microstructures were washed away by the developer the secondary radiation signs, shown by stains with the same shape of the structures, came out. As secondary radiation can not be avoided, an optimum dose must be found to confine the stains under the SU-8 structures without jeopardizing their adherence on the substrate. In doing so the seed layer is kept clean to allow electroforming which is the next step of the LIGA technique. Stains are made of a stable compound, insoluble in the developer, which is supposedly to be partially cross-linked SU-8.

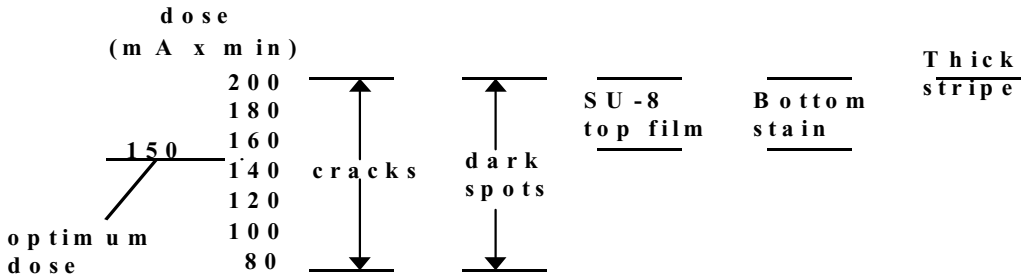

Figure 4. Diagram showing the dose range of the defects in SU-8 (125μm) deposited on (111) silicon wafers

Cracks spread all over the SU-8 layer and seems to be more common in X-ray than in optical lithography. This assertion is based on the fact that all steps of the X-ray lithography here performed, except exposure, follow the receipt used in optical lithography (Ferreira, 1998). In the latter cracks arouse only on the structure corners with 90^{o} or smaller angles. This could be indicating the generation of a greater number of radicals with X-ray than with UV exposure. Cross-linking from a great number of radical species, created by the more energetic X-rays radiation, would lead to higher stress and therefore to a larger cracks containing area. On the other hand suitable temperature ramp in the postbake step could prevent stress of the SU-8 layer and therefore the cracks (Chang, 2000)

SU-8 top layer results from exposure at high doses and its origin could be explained according to two mechanisms. The first one considers that, at high doses, the radiation passes through the absorber and penetrates into a very thin film of the SU-8 layer. This assumption seems not to be the case because the absorber thickness of our masks (M1: 4.5 μm and M2: 5.5 μm) are in the thickness range (2-20 μm) of the absorbers found in masks used for PMMA X-ray lithography (Vladimirsky et all, 1995; Coane el all, 1998; Maner et all, 1989; Malek, 1998). It is worth to bear in mind that if an absorber is opaque for the energy dose required for PMMA lithography it will be much more opaque for the energy dose required for sensitizing SU-8. The second mechanism Fig. (5) consider that the molecules of the air components, existing at the operating pressure (10^{-4} mbar) of de exposure chamber, became ionized during the exposure (Vladimirsky et all, 1995; Ohashi, 1996). The high reactivity of these ionized molecules could sensitize a thin film on the whole area of the SU-8 whereupon a fragile plaque which is supported on the top of the microstructures. The plaque would shatter under the turbulence due to the stirring of the developer solution leaving as result the pieces attached to the structures as shown in Fig.(3c).

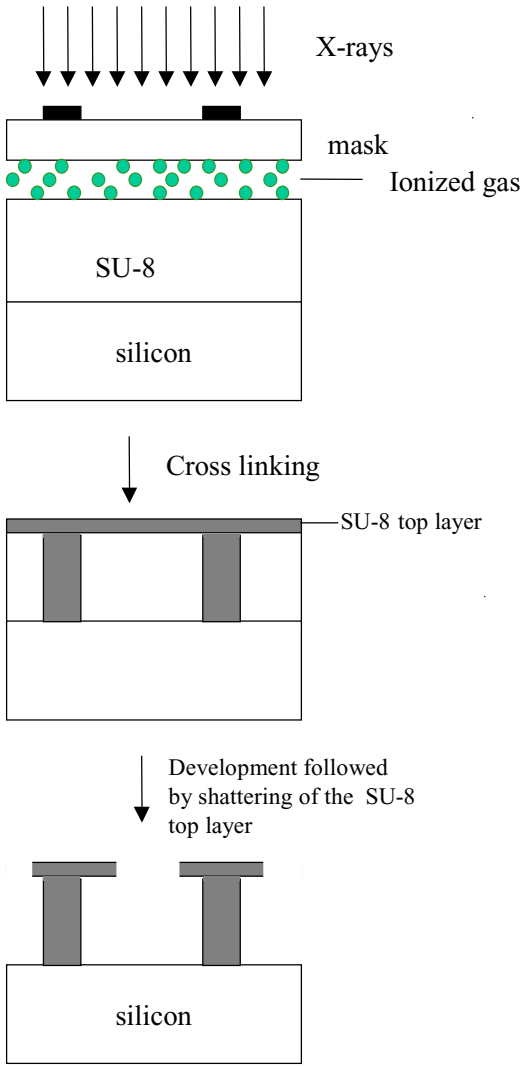

Figure 5. Diagram showing the formation of SU-8 top layer by the ionized atmospheric gases

The power spectrum related to the 50μm thick silicon membrane matched closely the filtering system composed of aluminum and kapton films. However, experimental results show that the exposure time to give a good lithography of 125 μm SU-8 layer is 2 to 3 fold higher for the silicon membrane mask than that for the aluminum/kapton filtering system (60 seconds). The main cause of this discrepancy, leaving aside the beam current at the moment of the exposures, could reside on the fact that the "good lithography" judgment was based solely on microscope image of the SU-8 microstructures. Other discrepancy factors could include the following items: (a) different mask patterns which could make comparisons based on microstructure images still more difficult; (b) the use of different exposure lines - the filtering system was used in the X-ray Instrumentation line (XRI) while the silicon masks in the X-ray lithography line (XRL); (c) poor absorber opacity. Absorber opacity depends on the gold density which in turn depends on its grain size and stress (Löchel, 1990;Kebabi, 1990; Reid et all, 1982). Grain sizes are expected to be different when different deposition techniques are utilized. Absorbers of the kapton masks (which is part of the filtering system) and of the silicon masks were produced by electroless and electroforming techniques respectively. All these three discrepancy sources show that a more refined experimental work must be made to validate the power spectrum simulation. Despite this, the fundamental consideration remains, i.e., the lithography of SU-8 can be satisfactorily performed, using thick silicon masks at short time in a synchrotron radiation source deprived of insertion devices for enhancing the photon flux of hard X-rays. Short time exposition allowed by SU-8 has inspired the use of a XRL line as a mass production of microstructures generated by a synchrotron source like LNLS (Ferreira el all, 1999). The commercial exploration of synchrotron sources for deep X-ray lithography has been recently reported (Zhang, 2000).

The SU-8 top layer is an indicative of the upper dose value for SU-8 as bubbles is for PMMA (El-Kholi, 1999). Then if the above model Fig. (5), which explains its origin, is correct atmospheric gases at low pressure will be necessary for revealing the upper dose value. The bottom stains can also be an indicative of upper dose particularly if it

prevents that the LIGA technological cycle be accomplished by covering the seed layer and therefore avoiding the electroforming step. The lower dose value for SU-8 is identified by the removal of the microstructures during the development processing. The difference in the upper/lower dose ratio for masks M1 (2.0) and M2 (1.3) suggests that the mask pattern can somehow play a role in these phenomena that indicate upper and lower dose. This suggestion is reinforced by the fact that some microstructures, particularly those having narrow bases, are more prone to be removed during the development step irrespective of the substrate.

5. Summary

2" diameter masks for deep X-ray lithography having blanks consisting of thick (100) silicon membranes were made using conventional photolithography, gold electroforming and KOH etching. X-ray deep lithography using these masks and the LNLS synchrotron source confirmed the simulations that showed that masks with thick silicon membranes could be suitable for performing SU-8 lithography with short exposure times in a synchrotron source not equipped with insertion devices for increasing the photon flux of high energy X-rays. This represents a considerable contribution to minimize the costs of X-ray deep lithography. Defects on the SU-8 microstructures were catalogued and their origin related to the mask, substrate/SU-8 interface, exposure chamber atmosphere and interaction of X-ray radiation with bulky SU-8. Based on these studies of defect origin the SU-8 top layer was identified as an indicative of the upper dose value. Further work will pursue the following goals: (a) refining the fabrication process of the absorber to eliminate the defects of the masks, i.e., wall tilting and covering failures; (b) elimination of the cracks by pre and postbaking experiments; (c) removal of the bottom stain by post lithographic treatment.

6. Acknowledgments

The authors thank the Electronic Microscopy Laboratory (LME) of the LNLS for the use of the JSM-5900LV microscope

7. References

Barcher W., Menz W., and Mohr J.,1995, "The LIGA Technique and Its Potential for Microsystems - A Survey", IEEE Trans. on Industr. Electron., Vol. 42, pp. 431-441.

Cerrina F. , 1997, "X-ray Lithography", Handbook of Microlithography, Micromachining and Microfabrication, Vol. 1:Microlithography, ed. P. Ray-Choudhury, SPIE Press, pp. 251-318.

Chang H. K., Kim, Y. K., 2000 "UV-LIGA Process for High Aspect Structure Using Stress Barrier and C-shaped Etch Hole". Sensors and Actuators, Vol. 84, pp. 342-350.

Coane P., Giasolli R., De Carlo F., Mancini D. C., Desta Y. and Gottert J. , 1998, Graphite-Based X-ray Masks for Deep and Ultradeep X-ray Lithography, J. Vac. Sci. Technol. B, Vol. 16, pp. 3618-3624. And references therein.

Despont M., Lorenz H., Fahrni N., Brugger J., Renaud P. and Vettiger P., 1997, "High Aspect Ratio, Ultrathick, Negative-Tone Near-UV Photoresist for MEMS Applications" , Proc. of X IEEE Intl. Workshop of Micro Electro Mechanical Systems – MEMS`97, Nagoya , Japan, pp. 1-5.

Ehrfeld W. and Schmidt A, 1998, "Recent Developments in Deep X-ray Lithography", J. Vac. Sci. Technol.B 16, pp. 3526-3534.

El-Kholi A. , 1999, "The Deep X-ray Lithography Step on Liga Process", Proceedings of V Escola Brasileira de Microeletrônica, Campinas –SP, Brazil. Not published.

Ferreira L. O S., Natal C. G., Gobbi A L, Vieira, 1998, "Desenvolvimento do Processo de Fabricação de Estruturas com Alta Razão de Aspecto em SU-8" Anais do IX Reunião de Usuários do LNLS, pp. 161.

Ferreira L. O S., Natal C. G., Gobbi A L, Vieira L. C. S., Bagnato O R., Francisco F. R., 1999, "Deep X-ray Lithography on SU-8 Photoresist", International Conference on Microelectronics and Packaging – ICMP99 Technical Digest, August 3-6, Brazil, pp. 37-40.

Ferreira L. O. S., Bagnato O. R., Natal G. C., Gobbi A. L., Francisco F. R., 1999, "Microfabrication of High-Aspect-Ratio Microstrucutures by LIGA Technology (Lithography, Electroforming and Molding)", 15th Brazilian Congress of Mechanical Engineering, November, pp.22- 26 Proceeding in CD-ROM.

Guckel H., 1998, "High-Aspect-Ratio Micromachining Via Deep X-Ray Lithography", Proceedins of the IEEE, Vol. 86, pp. 1586-1593.

Kebabi B, Malek K. C. , Ladan F. R. , 1990, "Stress and Microstructure Relationships in Gold Thin Films", Vacuum, Vol. 42, pp. 1353-1355.

Kupka R. K., Bouamrane F., Cremers C., Megtert S. , 2000, "Microfabrication: LIGA-X and Applications", Applied Surfaces Science, Vol. 164, pp. 97-110.

Madou M. J., 1997, "LIGA", Fundamentals of Microfabrication, , CRC Press, pp. 275-323.

Lee, K. Y., LaBianca, N., and Rishton, S. A., 1995 "Micromachining Application of a High Resolution Ultrathick Photoresist", J. Vac. Sci. Technol. B, Vol 13 (6), pp. 3012-3016.

Löchel B., Macioβek, Trube J., Huber H. L., 1990, "Pulse Plating of Quarter Micron Gold Patterns on Silicon X-ray Masks", Microelectronic Engineering, Vol. 11, pp. 279-282.

Lorenz, H., Loudon, M. and Renaud, P., 1998, "Mechanical Characterization of a New High-Aspect-Ratio Near UV-

Photoresist", Microelectronic Engineering, Vol. 41/42, pp. 371-374.
Malek C. K., 1998, "Mask Prototyping for Ultra-Deep X-ray Lithography: Preliminary Studies for Mask Blanks and High-Aspect-Ratio Absorber Patterns" , Proceedfing of the SPIE Conference on Materials and Device Characterization in Micromachining,Santa Clara CA, pp. 277-285.
Malek C. K, Wood R., Dudley B., Genova P., 1998 " Metrology Study of Structural Transfer Accuracy in Fabrication of High Aspect-Ratio Microelectromechanical Systems: From Optical Mask to Polished Electroplated Parts" J. Vac. Sci. Technol. B, Vol. 6 (6), pp. 3552-3557.
Maner A., Ehrfeld W., 1989, "Electroforming Techniques in the LIGA Process for the Production of Microdevices", Materials & Manufacturing processes, Vol. 4, pp. 527-537.
Ohashi H. , Ishiguro E., Sasano T., Shobatake K., 1996, "Synchrotron Radiation Excite Etching of Diamond", Applied Physics Letters, Vol. 68, pp. 3713-3715.
Peckerar M. C., Maldonado, J. R., 1993, "X-ray Lithography – an Overview" , Proceedings of the IEEE 81, pp.1249-1274.
Vladimirsky Y., Morris K., Klopf J. M., Vladimirsky O., Saile V. and Scott J., 1995, "X-ray Exposure System for Induced Chemistry and Dry Processes in Microlithography", J. Vac. Sci. Technol. B, Vol. 13, pp. 3109-3113.
Vladimirsky Y., Vladimirsky O., Saile V., Morris K., Klopf M., 1995, "X-Ray Mask Fabrication Techniques for Micromachining", 15th Annual Symposium on Photomask Technology and Management, 20-22 September, Santa Clara, C.A., SPIE ,Vol. 2621, pp. 399-405.
Reid H. F, Goldie W., 1982, "Gold Plating Technology, Electrochemical Publications Limited", pp. 316-321.
Tolfree D. W. L., 1998, "Microfabrication Using Synchrotron Radiation", Report on Progress in Physics, Vol. 86, pp. 313-351.
Zhang Y. and Hori T., 2000, " A Compact Warm Ring for Industrial Applications", Synchrotron Radiation News, Vol. 13, pp. 32-33.

XVI CONGRESSO BRASILEIRO DE ENGENHARIA MECÂNICA
16th BRAZILIAN CONGRESS OF MECHANICAL ENGINEERING

LIGA TECHNOLOGY – Cu, Au and Ni ELECTROFORMING

Izaque A. Maia
National Synchrotron Light Laboratory – Microfabrication Laboratory/MIC
Caixa Postal 6192 CEP 13084 -971 Campinas – SP - Brazil izaque@lnls.br

Luiz O. S. Ferreira
Idem lotavio@lnls.br

Maria Helena O. Piazzetta
Idem nena@lnls.br

Graziele C. Natal
Idem graziele@lnls.br

Abstract The objective of the present work is to present and discuss the delamination problem found in running the Multiuser Project (MUSA 2000 -Copper) where copper microstructures of different sizes and shapes and for various applications are electroformed together, on a same substrate, using LIGA technology. Delamination occurred when copper layers (40-50 μm) were electroformed on substrates having conductive thin films deposited on thick (1 μm) thermally grown silicon oxide layers (TTGSOL). Delamination was prevented by replacing commercial bath by homemade bath or by sending samples to be electroformed in an industry. This is an exploratory work that will be useful in a further refinement work. Few nickel electroforming experiments suggest the existence of the same problems and solutions found in the copper experiments. Gold electroforming was performed to produce absorbers for X-ray masks. The performance of photopolymer mold, rather than delamination, was the main issue addressed. The studies of mold performance, evaluated in terms of microstructure lateral resolution and mold removal after electroforming, revealed that a new photoplolymer should be found to meet the stringent X-ray mask requirements

Key words: delamination, LIGA, electroforming, MUSA, MEMS

1. Introduction

LIGA is a technology developed in the Research Center of Karlsruhe (FZK) in the late 70´s for producing small slotted nozzles for uranium isotope separation (Becker, 1982) and has been under development since then for mass-production of metallic and polymeric microdevices with high aspect ratio (height/width ratio) (Tolfree, 1998). It is the extension of the miniaturization capabilities for materials others than semiconductors which are the core of microelectronic and optoelectronic industries. LIGA is the acronym of its three major steps: lithography (**Li**thographie), electrodeposition (**G**alvanoformung) and molding (**A**bformung) Fig. (1). By lithography 3-D micromolds are sculptured on a thick layer (up to 2 mm) of a photopolymer adhered to a conductive base. The photopolymer is irradiated with X-ray (LIGA-X) or UV (LIGA-UV) through a mask containing the corresponding 2-D pattern (Lorentz, 1998). The 3-D micromolds exhibit a metallic bottom for electroforming a metallic mold which in turn is used in polymeric molding.

The polymeric mask influences the distribution of the current density during the electroforming step (Romankiw, 1997). In general, regions that are more densely populated with polymer tend to attract a higher current density whereupon thicker deposits. To improve the uniformity of current distribution on the substrate scale one can diminish the effective anode-cathode distance (Datta, 2000). However, on the microstructure scale, i.e., inside the recess of the photopolymer layer whose bottom expose the metallic surface, the thickness uniformity is under mass transport regime due to the presence of the stagnant (diffusion) layer. Under this regime leveling is achieved by additives (cathodic leveling agents) (Lyons, 1974) and surfactants are commonly added to electrolytes to facilitate evacuation of gas bubbles. A company has been claiming that a physical technique, called fibrillation, perform at the same time leveling and surfactant action and also decrease metal accumulation on the top corners of the microstructures.

Besides the effect of the polymeric mask, terminal effect is another one which causes thickness nouniformity on the substrate scale (Dini, 1992). This effect leads to higher deposit thickness in the vicinity of the current collector. It occurs mainly on poorly conducting substrate which requires a metallic thin film deposition for electroforming as is the case of LIGA technology.

The present work discusses qualitative data acquired on the course of the Multi User Project (MUSA 2000) of the Laboratório Nacional de Luz Síncrotron (LNLS), where metallic microstructures of different sizes and shapes and for various applications are electroformed together, on a same substrate, using LIGA technology. The MUSA 2000 mask Fig. (2) has patterns of microsieves, antennas for microwave radiation and also microstructures for various tests, namely, mechanical, adhesion, lateral resolution and layer thickness. The metal base for electroforming was formed by

thin layers called bond layer and seed layer which were deposited on this order on a silicon wafer. The bond layer works as a kind of glue for keeping the seed layer adhered to the silicon wafer. A third thin layer, called top layer, protects the seed layer against oxidation and also works as an adhesion layer for the photopolymer. This protective layer is removed soon before the electroforming starts in order to expose a fresh seed layer. The MUSA 2000 mask was used in the fabrication of masks for X-ray lithography using gold layer as the X-ray absorber.

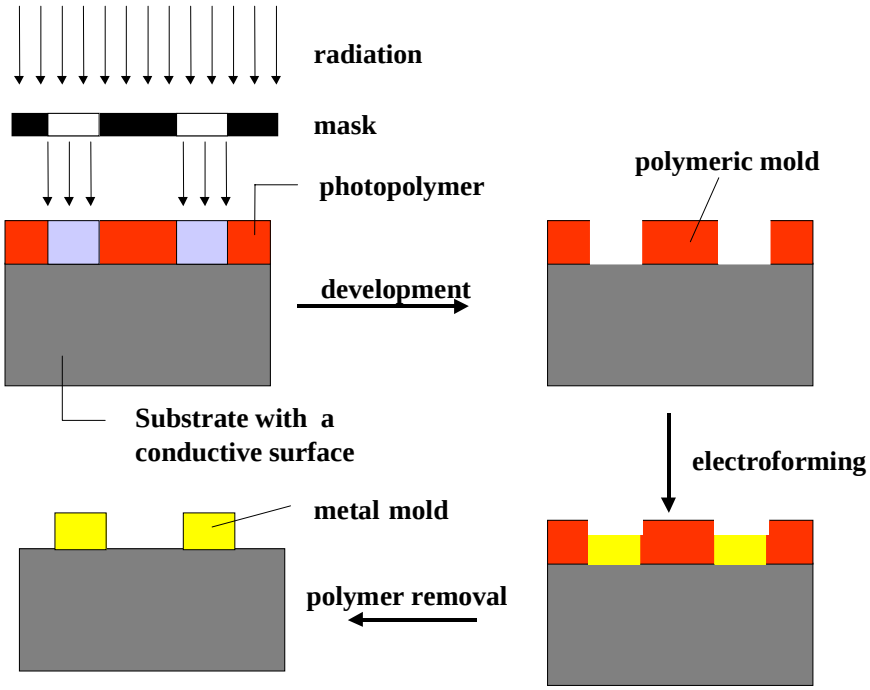

Figure 1 – LIGA steps

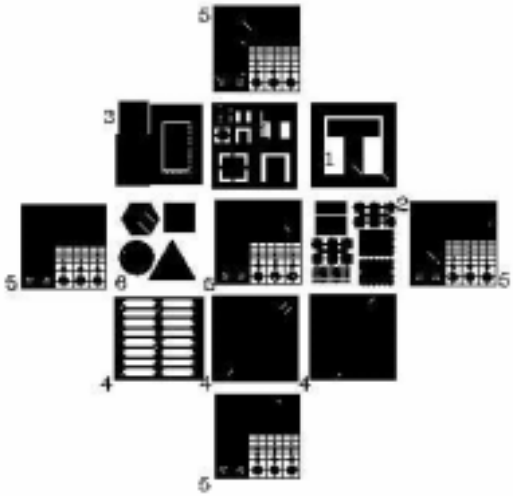

Figure 2 – MUSA 2000 mask layout and their corresponding projects (see reference numbers): (1) Flexible structures for mechanical properties measurements of the microfabrication materials used in the LNLS; (2) Photonic band gap matrix for using in microwave optics; (3) Antennas with photonic band gap for microwave; (4) Microsieves for fluids filtering and solids separation with regular 20μm diameter porous; (5) Resolution testing structures for lithography and electroforming; (6) Adherence testing structures for SU-8 e metal layers.

2. Experimental

2.1 Substrate preparation.

The substrates for copper and nickel electroforming were prepared by the following steps in Fig. (3): (100), (111), 2" diameter silicon wafers were cleaned with acetone, hot isopropanol alcohol and dried with nitrogen blows. (100) silicon wafers having a thermally grown thick (1μm) silicon oxide layer (TTGSOL) were not cleaned. A set of thin layers were deposited on silicon and TTGSOL in this order: titanium (200 Å) , copper (500 Å) and titanium (200 Å) with sputtering or, alternatively, chromium (200 Å), copper (500 Å), chromium (200 Å) with thermal evaporation. Following 50 μm thick layers of SU-8 , a negative tone photopolymer, were spinned and microstructures were patterned with the MUSA 2000 mask using UV radiation. Before electroforming the exposed titanium and chrome top layers were removed with HF 5%. The chromium etch composition was $K_3[Fe(CN_6)]$, NaOH, water (20g, 10g, 100ml). The appearance of red color indicates that the copper layer is exposed and ready for electroforming. The Si/Cr/Cu/Cr substrates used for cooper electroforming were also used for nickel electroforming.

The substrates for gold electroforming were prepared by sputtering titanium and gold, in this order, on (100) silicon wafer. SU-8 (Microchemical Co.) and AZ4620 (Shippley Co.), 10-15 μm thick layers, were spinned on these substrates and patterned with UV lithography using the MUSA 2000 mask.

2.2 Electrolytic bath

The electrolytic cell design, for each metal, was kept with the same geometry in all experiments and the current density values and bath composition used followed the technical bulletin of the supplier. The suppliers are: Orwek Química (Nickel bath DWK 720), Tecnorevest (Copper Gleam PCM) and Degussa (Gold – Auruna 552). Homemade bath was prepared following also the composition and current density of the technical bulletin but P.A. reagents were used.

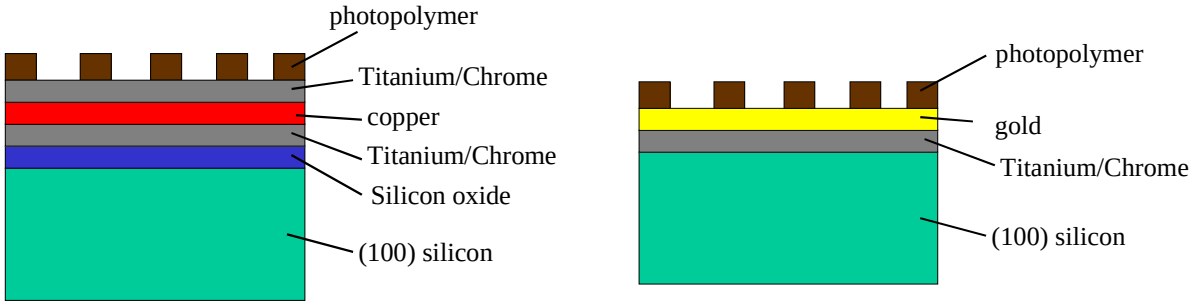

Figure 3 – Samples with layer structure for electroforming of copper and nickel (left) and gold (right)

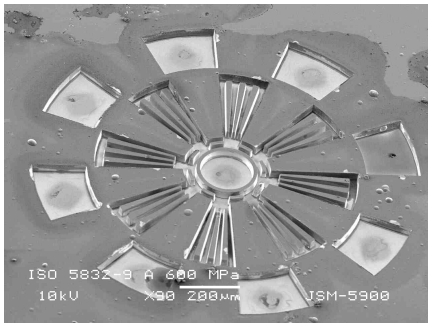

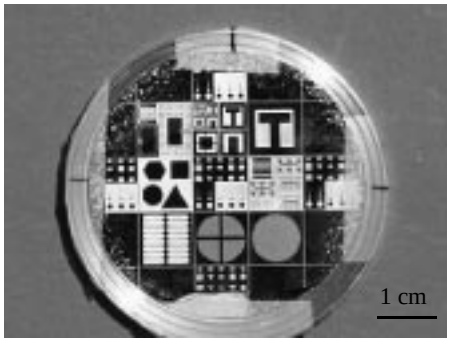

Figure 4 (left) Electroformed Nickel mold of a micromotor (Metalfoto Co.)
Figure 5 (right) X –ray mask showing the MUSA 2000 pattern. The clear areas are electroformed gold

3. Results

Data related to copper electrofroming are summarized in Table 1. Samples without TTGSOL did not present delamination irrespective of the crystallographic orientation of silicon wafer, bond layer metal and vacuum technique used for depositing it. Delamination occurred only in samples where both conditions – TTGSOL and commercial bath – were present simultaneously. However similar samples, with TTGSOL and same pattern (MUSA 2000), sent to be copper electroformed in the industry did not exhibited delamination. Moreover the morphology of these industry-

eletroformed-samples were more specular and exhibited small amount of pits compared to the samples obtained in our laboratory. Samples with titanium top layer presented superior morphology compared to those with chromium top layer. In few nickel electroforming tests we observed delamination but similar nickel samples sent to the same industry where copper were electroformed did not present delamination. Moreover the nickel structures exhibited straight walls and 6:1 aspect ratio Fig. (4).

No delamination was observed in gold electroforming. SU-8 photopolymer is very stable in cyanide gold bath allowing, as result, a good lateral definition of the electroformed structures. However SU-8 removal is an awkward task because it does not dissolve in its proprietary remover. Instead it detach from the substrate in the form of small plates resembling dandruff that stick on the metallic structures. Differently of the SU-8, the AZ 4620 is attacked by the cyanide gold bath impoverishing, as result, the microstructures lateral resolution. AZ 4620 is highly soluble in acetone. The gold pattern in the 2000 MUSA X-ray mask in showed in Fig. (5).

Table 1. Adherence of electroformed copper layers (~50 μm thick) on different substrates and bath origin

substrates		bath	Copper delamination
wafer	Thin metallic films		
Si [111]	Cr/Cu (TE)	commercial	no
	Ti/Cu (Sp)		no
Si [100]	Ti/Cu (Sp)		no
Si[100]/ TTGSOL	Cr/Cu (TE)		yes
	Ti/Cu (Sp)		yes
	Cr/Cu (TE)	Home-made	no
	Ti/Cu (Sp)		no
	Cr/Cu (TE)	industry	no
	Ti/Cu (Sp)		no
Sp:Sputtering T.E. thermal evaporation			

4. Discussion

Delamination occurs when the forces associated to the stress of the thick metallic layers surpass the bonding forces in the wafer/bonding-layer interface. That could be occurring when TTGSOL and commercial bath are employed for copper and nickel electroforming. The adhesion forces in the TTGSOL/bonding layer interface are weak due to the high stress of the TTGSOL as showed in Fig. (6). They become weaker, leading to delamination, due to the greater stress of the thick metallic layers brought about when commercial (contaminated) bath is used instead homemade (purer) bath. The commercial copper and nickel baths are not prepared with P.A. reagents, as is the case of home-made bath, otherwise they would be quite expensive to be used in large scale as it occurs nowadays. Impurities are an important source of stress of metallic layers (Dini,1992). It should be kept in mind that commercial baths are formulated for thin layers which are used in surface treatment. Its formulation could not satisfy the requirements for thick layers (~50 μm) applications as it is the case of LIGA technology. The impurities in the commercial bath are supposedly to be soluble and then not removable by mechanical filtering.

Instead delamination, the main problem related to gold electroforming concerns the photopolymer mold. SU-8 is quite stable in the cyanide gold bath but is of difficult removal after the electroforming has been performed. The AZ 4620 is of easy removal but their microstrucutres undergo lateral deformation in the cyanide gold bath. An ideal solution resides in finding a new photopolymer which present the best characteristics of SU-8 and AZ 4620. Alternatively it could be used a gold bath with a proper formulation, e.g. with lower pH, that does not etch the AZ 4620.

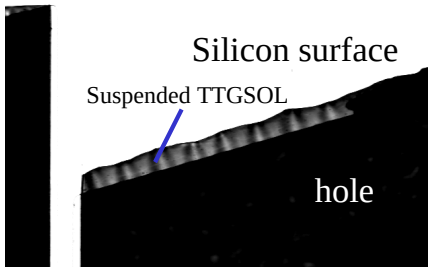

Figure 6 – TTGSOL becomes corrugated when the silicon underneath is removed. The corrugation of the resulting suspended TTGSOL reveals its high stress.

5. Final Remarks

To obtain thick metallic layer with free stress on TTGSOL is a great goal the we persue because such stress is a limiting factor in the monolithic integration of microelectronics and micromechanics. The elimination of the delamination achieved in the wake of the MUSA project was a progress towards this goal. However avoiding delamination only is not a safe indicative of good adherence. Then further and fine studies must be carried out in order to assess the magnitude of the adherence in the metal/oxide interface.

6. Acknowledgments

We thanks the industry Metalfoto for copper and nickel electroforming work and the Electronic Microscopy Laboratory (LME) of the LNLS for the JSM 5900LV photograph. We also thanks the metal microstructure designers who took part in the MUSA 2000 project, namely, Prof. Dr. José Roberto de França Arruda (Fac. Eng. Mecânica – UNICAMP), Profa. Dra. Maria Aparecida Silva (Fac. Eng. Química – UNICAMP), Prof. Dr. Luiz Carlos Kretley (Fac. Eng. Elétrica – UNICAMP), Eng. André Távora de Albuquerque Silva (Fac. Eng. Elétrica e de Computação – UNICAMP).

7. References

Becker E. W., Betz H., Ehrfeld W., Glashauser W., Heuberger A., Michel H. J., Münchmeyer D., Pongratz S. and von Siemens R., 1982, "Production of Separation Nozzle Systems for Uranium Enrichment by a Combination of X-ray lithography and Galvanoplastics, Naturwissenschaften, vol. 69, pp. 520-523.

Datta M., Landolt D., 2000, "Fundamentals Aspects and Applications of Electrochemical Microfabrication" Electrochimica Acta, vo.l 45, pp. 2535-2558.

Dini J. W., 1992, "Electrodeposition, The Materials Science of Coatings and Substrates", Noyes Publications, pp. 297-298.

Lorentz H., Despont M., Farhni N., Brugger J., Vettiger P., Renaud P., 1998 "High-aspect-ratio, Ultrathick, Negative Tone Near-UV Photoresist and its Applications for MEMS" , Sensors and Actuators A, vol. 64, pp. 33-39.

Lyons, E. H. Jr, 1974, "Modern Electroplating", ed. Lowenheim F. A., 3rd ed., John Wiley&Sons Inc. , Ch 1, pp.31-35.

Romankiw, 1997, "Review – A Path: From Electroplating Through Lithographic Masks in Electronics to LIGA in MEMS", Electrochimica Acta, vol. 42, pp. 2985-3005.

Tolfree D. W. L., 1998, " Microfabrication Using Synchrotron Radiation" , Rep. Prog. Phys., vol 61, pp 313-351.